

A TALE OF TWO VERTICES:

Production and Decay of the Higgs VV Vertex at the LHC

by

Ian J. Anderson

A dissertation submitted to The Johns Hopkins University in conformity with the
requirements for the degree of Doctor of Philosophy.

Baltimore, Maryland

May, 2015

© Ian J. Anderson 2015

All rights reserved



Abstract

In July 2012, a Higgs-like boson was observed jointly at CMS and ATLAS at CERN's Large Hadron Collider. For this thesis, we will revisit the theoretical motivation of the Higgs boson in the Standard Model, including its expected properties of production and decay. Using the $H \rightarrow ZZ \rightarrow 4l$ decay channel on the first run of CMS data in 2011 and 2012, we will establish the procedure used to observe the Higgs boson at its current statistical significance at $\sim 7\sigma$. The first measurements of the boson's mass ($m_H = 125.6$ GeV), signal strengths ($\mu_F = 0.80^{+0.46}_{-0.36}$, $\mu_V = 1.7^{+2.2}_{-2.1}$), width ($\Gamma_H < 46$ MeV), and spin-parity ($J^{PC} = 0^{++}$) will be discussed along with exclusions on additional Higgs-like bosons in the $H \rightarrow VV$ decay. Using the kinematics of the decay and production, all measured properties of the observed Higgs boson will be shown to agree within uncertainty with Standard Model predictions. Finally, the sensitivities of future Higgs boson property measurements will be discussed and quantified for the lifetime of the LHC and proposed future colliders, where the projections are comparable to some Beyond the Standard Model predictions.

ABSTRACT

Primary Reader: Andrei Gritsan

Secondary Reader: Morris Swartz

Acknowledgments

Unsurprisingly, it's difficult for me to acknowledge all those who have been there in some form or another along my journey to this point. Not for spite or pride, but for brevity; there are neither enough words nor pages for me to adequately thank everyone in name or deed. I am eternally grateful for each of you, this is only a small slice thereof.

First and foremost, I would like to thank my advisor, Andrei Gritsan. Over the past few years that I've known and worked with you, we've published a number of different results that have all taken countless shared hours, conversations, and emails. What I've learned from our talks – either in physics, in communication skills, or in self-determination – has been invaluable. Without your intuition, encouragement, and support, I wouldn't be where I am today.

I must also thank all of my colleagues and collaborators in the JHU HEP group. I owe much of what has been achieved and who I have become in the last few years to you. Morris, Petar, Barry, and Bruce have each supplied words of advice and inspiration over my time at Hopkins. Yanyan, Nhan, Andrew, Sara, and Meng:

ACKNOWLEDGMENTS

your ample experience and boundless patience was a godsend. To Candice and Heshy, I feel so lucky to have worked alongside you. For Marc, Dave, Nick, Kevin, Yongjie, Alice, Raymond, and Yaofu: our debates, collective troubleshooting, and general companionship has been my sustenance. And to Chris and Ulascan, there is no earthly way these results would have made it to publication without our discussions, arguments, and sweat. Knowing that we were in this together made it not only feasible but enduring.

To those JHU colleagues now elsewhere, especially Kirill, Fabrizio, and Markus, I'm honored to have collaborated with you. For my fellow CMS members abroad, especially Roberto, Nicola, NDF, Michalis, and all the collaborators from the Higgs and ZZ4L group, your expertise and assistance has been crucial, both to myself and the field. To the administrative staff in Bloomberg – Carm, Pam, Kelley, Brian – I'm so grateful for everything you have done to keep this program afloat.

To Chris, Matt, Sean, and David: your combined theoretical expertise is awe-inspiring and our various discussions – on physics or far afield – have been immeasurable and I'm honored to call you friends. Tristan, Kate, Grace: our adventures through these past few years are some of the most memorable experiences I've ever had and I will always treasure them. For Matt, Justin, Nik, Keith, Derek, JT, and Mike, thank you for all of the great – occasionally inane, though nothing if not interesting – conversations and good times we've had together. To KFC, thank you for all the – almost always inane – phone calls, late nights, and arguments over the

ACKNOWLEDGMENTS

years.

Lastly, the support and understanding from my family has been my rock through troubled seas. Throughout my life, there have been periods of unease, stress, and heartbreak. And yet, I am always in awe at your resilience and limitless love. Truly, to my parents, to my siblings, to my aunts and uncles and cousins, I owe my life and who I am to you all. Finally, to my wonderful girlfriend Nassira, I cannot imagine what my life would have been without you. That I could have been fortunate enough to meet you, to share this journey next to you, to grow with you - I feel so privileged and I can't wait to see what we do next.

Dedication

In so many ways, this thesis is dedicated to Sophie, Jane, Jeanie, Grammy, Louise, Marie, Ritchie, Herk, and Lorraine.

Contents

Abstract	ii
Acknowledgments	iv
List of Tables	xii
List of Figures	xiii
1 Introduction	1
1.1 Theoretical Motivation	1
1.1.1 Our Cast of Characters: Fundamental Particles	2
1.1.2 The Story: The Status of the Standard Model Before the LHC	8
1.1.2.1 Searching for Professor Higgs' Boson	10
1.1.2.2 Expecting the Unexpected	14
1.2 Summary	17
2 Experimental Setup	19

CONTENTS

2.1	The Large Hadron Collider	19
2.2	Our Setting: The Compact Muon Solenoid	23
2.2.1	Coordinates and Conventions for the CMS	25
2.2.2	Subsystems in CMS	25
2.2.2.1	The Magnet	25
2.2.2.2	Inner Tracking System	26
2.2.2.3	Electromagnetic Calorimeter	32
2.2.2.4	Hadronic Calorimeter	34
2.2.2.5	Muon System	38
2.2.3	Particle Identification	42
2.2.4	Triggers	44
2.3	Summary	45
3	Higgs Boson Phenomenology at the LHC	47
3.1	How to Find a Higgs Boson at LHC	47
3.1.1	An Interlude on Feynman Diagrams	48
3.1.2	Higgs Boson Production	51
3.1.3	Higgs Boson Decay	56
3.2	Studying the HVV Vertex	59
3.2.1	$H \rightarrow VV$	59
3.2.2	$V^*V^* \rightarrow H$	65
3.2.3	$V^* \rightarrow VH$	68

CONTENTS

3.3	Summary	69
4	Higgs Boson Discovery in $ZZ \rightarrow 4\ell$	70
4.1	Object Definitions	70
4.1.1	Electrons	71
4.1.2	Muons	73
4.1.3	Lepton Isolation and Photons	75
4.1.4	Jets	79
4.2	MC and Datasets	80
4.3	Event Selection	84
4.4	Likelihood Analysis	86
4.4.1	Expected $m_{4\ell}$ Distributions	88
4.4.2	Kinematic Discriminant for Decay	94
4.4.3	Discriminating Production Mechanisms	94
4.4.4	Systematic Uncertainties	100
4.5	Results	104
4.6	Summary	120
5	Higgs Boson Properties in $ZZ \rightarrow 4\ell$	121
5.1	Prelude to Property Measurements	121
5.2	High Mass Higgs Search	122
5.3	Higgs Boson Spin-Parity	131

CONTENTS

5.4	Higgs Boson Width	139
5.4.1	Finding the Width in the Off-Shell Region	140
5.4.2	Off-Shell 4ℓ Analysis	143
5.4.3	Width Measurement Using Off-shell Analysis	155
5.5	Off-Shell Anomalous Coupling	159
5.6	Summary	172
6	Conclusions and Outlook	173
	Bibliography	182

List of Tables

2.1	Design Parameters of the LHC	22
4.1	MC Samples for $H \rightarrow ZZ \rightarrow 4\ell$	81
4.2	Normalization Uncertainties in the 4ℓ Discovery	102
4.3	Number of Observed 4ℓ Events in $100 < m_{4\ell} < 1000$ GeV	104
4.4	Number of Observed 4ℓ Events in $121.5 < m_{4\ell} < 130.5$ GeV	107
4.5	Number of Observed 4ℓ Events in $121.5 < m_{4\ell} < 130.5$ GeV Split by Jet Categorization and Production Mechanism	117
4.6	Summary of Observed 4ℓ Signal Strengths	119
5.1	List of Alternative Spin-Parity States for 125.6 GeV Resonance	132
5.2	Summary of Allowed Intervals for Anomalous Spin-0 Couplings in 4ℓ for 125.6 GeV Higgs Boson	136
5.3	Expected and Observed 4ℓ Yields in Off-Shell Region	157
5.4	Categorizations and Observables Used in On-shell and Off-shell Re- gions of $f_{\Lambda Q}$ Measurement	163
6.1	Projected Sensitivities for CP-Violating Anomalous Coupling of Higgs Boson at LHC and Future Colliders	181

List of Figures

1.1	Fundamental Particles of The Standard Model	7
1.2	The Brout-Englert-Higgs Mechanism	12
1.3	Higgs Mass Limits Before the LHC	14
2.1	The CMS Detector with Sub-Detector Systems	24
2.2	Geometry of the Tracker System	27
2.3	Global Track Reconstruction Efficiency at CMS	29
2.4	Resolution of the Electromagnetic Calorimeter as a Function of Energy	34
2.5	Sample Output of the Hadronic Calorimeter	36
2.6	Resolution of the Hadronic Calorimeter as a Function of Simulated Transverse Energy	37
2.7	Arrangement of Detectors in CMS Muon System	39
2.8	Muon Momentum Resolution at CMS	41
2.9	Trajectories and Decays for Particle Identification in CMS	43
3.1	Compton Scattering as an Example Feynman Diagram	49
3.2	Feynman Diagrams of Bhabha Scattering	51
3.3	Higgs Production Mechanisms	53
3.4	Standard Model Production Mechanism of the Higgs at the LHC as a Function of the Higgs' Mass	55
3.5	Standard Model Decay Branching Ratios for the Higgs at the LHC as a Function of the Higgs' Mass	57
3.6	Definition of Angles in $H \rightarrow VV$ Decay	63
3.7	Feynman Diagrams of the HVV vertex	65
3.8	Definition of Angles in VBF Production	67
4.1	Expected Energy Resolution for Electrons	72
4.2	Mass Resolution and Bias from Di-electron Decays	74
4.3	Mass Resolution and Bias from Di-muon Decays	76

LIST OF FIGURES

4.4	Overall Efficiencies of Electron and Muon Reconstruction and Selection in 4ℓ Analysis	78
4.5	Higgs Width as a Function of m_H	82
4.6	Irreducible ZZ Backgrounds in the 4ℓ Channel	83
4.7	Signal Efficiency of Gluon Fusion as a Function of m_H	87
4.8	Reducible Background Mass Shapes	91
4.9	Low Mass Higgs Signal Mass Shapes	92
4.10	High Mass Higgs Signal Mass Shapes	93
4.11	Templates of Kinematic Discriminant for $H \rightarrow ZZ \rightarrow 4\ell$	95
4.12	Dijet Ratio of Gluon Fusion and Weak Vector Boson Fusion as Function of m_H	96
4.13	Dijet Ratio of Associated Production as Function of m_H	97
4.14	Transverse Momentum Shapes of Different Higgs Production Mechanisms	98
4.15	Templates of Transverse Momentum for 4ℓ Signals and Background	99
4.16	Jet Kinematic Shapes of Different Higgs Production Mechanisms	99
4.17	Templates of \mathcal{D}_{jet} for Signals and Background	100
4.18	Calibration and Closure Test of Per-Event Mass Errors in 4ℓ	103
4.19	$m_{4\ell}$ Distributions of 4ℓ Events	105
4.20	$m_{4\ell}$ Distributions of 4ℓ Events, $m_{4\ell} < 180$ GeV	106
4.21	Exclusion Limits and Local Probabilities for 4ℓ Events	110
4.22	Observed D_{bkg}^{kin} Distributions for 4ℓ Events	111
4.23	Observed D_{bkg}^{kin} Distributions for Low Mass 4ℓ Events With Signal Expectations	112
4.24	Observed p_T Distributions for Low Mass 4ℓ Events With Signal Expectations	113
4.25	Observed \mathcal{D}_{jet} Distributions for Low Mass 4ℓ Events With Signal Expectations	114
4.26	Mass Measurement of the Discovered Particle	115
4.27	Signal Strengths of the Discovered Particle Split By Jet Categorization and Production Mechanism	118
5.1	Improvement of the \mathcal{D}_{jet} Discriminant Using MELA Techniques	127
5.2	Templates of \mathcal{D}_{jet} Using vbfMELA	128
5.3	Combined Expected and Observed Exclusion Limits for High Mass Higgs Search	129
5.4	Limits on C'^2 for Different Values of \mathcal{B}_{new} in the EW Singlet Extension to the Standard Model	130
5.5	Kinematic Distributions for SM and Alternative Spin-Parity States near 125.6 GeV Resonance	132
5.6	Exclusion Limits on Mixed Spin-1 State in 4ℓ for 125.6 GeV Higgs Boson	137

LIST OF FIGURES

5.7	Summary of Spin-2 Exclusion Limits in 4ℓ for 125.6 GeV Higgs Boson	138
5.8	Summary of Allowed Intervals for Anomalous Spin-0 HVV Couplings for 125.6 GeV Higgs Boson	139
5.9	Direct Measurement of Higgs Width in 4ℓ Decay Channel	140
5.10	Differential Cross Section at LO from $gg2VV$ for Off-shell Region	144
5.11	Comparison of Off-shell Differential Cross Section between $gg2VV$ and MCFM	145
5.12	Comparisons Between VBF and ggF Productions for Off-Shell Region	146
5.13	NNLO/LO Scale Factor at 8 TeV for ggF Signal	148
5.14	Modeling of Off-Shell Normalizations in 4ℓ	149
5.15	2D $(m_{4\ell}, \mathcal{D}_{gg})$ Templates for Off-Shell 4ℓ Analysis	152
5.16	NLO Electroweak Corrections for $q\bar{q} \rightarrow ZZ$ Background	154
5.17	$m_{4\ell}$ Distributions of Expected and Observed 4ℓ Events in the On-Shell and Off-Shell Regions	156
5.18	$m_{4\ell}$ and \mathcal{D}_{gg} Distributions of Expected and Observed 4ℓ Events in the Off-Shell Signal-Enhanced Region	158
5.19	Expected and Observed Limits on Higgs Width	160
5.20	Simulated Off-shell Enhancements in the 4ℓ Channel from Anomalous HVV Couplings	162
5.21	$\mathcal{D}_{\text{jet}} > 0.5$ Ratios for Production Separation in $f_{\Lambda Q}$ Measurement	165
5.22	$m_{4\ell}$ Distributions of Jet Categorized Expected and Observed 4ℓ Events in the Off-Shell Region for $f_{\Lambda Q}$ Measurement	167
5.23	Expected and Observed Limits on Higgs Boson Width with Anomalous Coupling	169
5.24	Expected and Observed Limits on $f_{\Lambda Q} \cos(\phi_{\Lambda Q})$	170
5.25	2D $(\Gamma_H, f_{\Lambda Q})$ Observed Likelihood Scan	171
6.1	Higgs Boson Signal Strength for CMS Combination Split by Decay Channel	175
6.2	Higgs Boson Signal Strength for CMS Combination Split by Production	176
6.3	Summary of Precisions for CP-Violating Anomalous Coupling in HVV Vertex at LHC and Future Colliders	179

Chapter 1

Introduction

“It has long been an axiom of mine that the little things are infinitely the most important.”

Arthur Conan Doyle, “The Memoirs of Sherlock Holmes”

1.1 Theoretical Motivation

In some sense, a discovery seemed inevitable. Near Geneva, beneath the foot of the Jura Mountains, the Large Hadron Collider (LHC) has been accelerating protons at higher energies than any collider to date, continuing the fruitful lineage of technological advancement and scientific discovery from earlier particle accelerators. On July 4, 2012, in a joint announcement from CMS and ATLAS, the organizations of the two respective general purpose detectors at the LHC, it was announced that a Higgs-like boson¹ was observed which opened a new window

¹Although it is now considered “a Higgs boson”, contemporarily it was deemed “a Higgs-like boson” until further study could be done.

CHAPTER 1. INTRODUCTION

to probe the foundations of the universe. The genesis of this announcement can be traced to ancient Greece and India with the origins of atomism - the postulate that there exist fundamental, unbreakable constituents that make up all matter - through the discovery of quantum mechanics to today. The Standard Model (SM) is the model proffered by particle physicists for explaining the underpinnings of matter in our universe. This discovery appears to be the observation of the last remaining piece of this model.

Conceived in the 1970s, the SM has been one of the most successful scientific models² ever. Precision tests have repeatedly agreed with SM predictions and fundamental particles which were not observed at the time of conception have since been discovered. The Standard Model's particles and their interactions, along with how they act in the aggregate, can explain nearly all phenomena across any size or time frame in our universe. But, as we will see in Sec. 1.1.2, there still remain large unanswered questions which we may hope to probe by looking in detail at this new boson.

1.1.1 Our Cast of Characters: Fundamental Particles

Broadly, the Standard Model consists of a series of point particles with only a few basic characteristics: spin, charge, and mass.

Spin can be thought of as the intrinsic angular momentum of a particle. It can

²The only possible usurper is special relativity which underlies some of the mathematics of the SM.

CHAPTER 1. INTRODUCTION

only take integer or half-integer values, which is used to classify particles into two categories: *Bosons* (integer spin) and *Fermions* (half-integer spin). This classification isn't arbitrary; the spin determines the general role of that particle. Fermions obey Fermi-Dirac statistics and therefore cannot occupy identical energy states. These become the building blocks of all observed material in the universe. Bosons instead obey Bose-Einstein statistics – they are permitted to occupy identical energy states – and make up the force carriers. If fermions are the pieces, bosons are the glue that binds them.

These particles can interact through any of the four observed forces: Electromagnetism, the Weak and Strong forces, and Gravity. Gravity is different than all other forces and not integrated into the Standard Model (see Sec. 1.1.2), but the other three forces are. We can further differentiate the fermions based on what forces they interact with. Fermions that interact with the strong force are called *quarks*, whereas *leptons* do not. How strongly these fermions interact with a given force is quantified in the concept of charge. Traditionally, when we use the term “charged” in reference to a particle, it refers to whether it interacts with electromagnetism. There are three charged leptons: the electron has unit negative charge as do its two heavier cousins, the μ and the τ . There are also three uncharged leptons called neutrinos: the electron neutrino, the μ neutrino, and the τ neutrino. All quarks are charged; the up (u), charm (c), and top (t) quarks (*up-type*) have charge of $+2/3$ while the down (d), strange (s), and bottom (b) quarks (*down-type*) have

CHAPTER 1. INTRODUCTION

charge $-1/3$. The force carrier of electromagnetism is a massless, uncharged boson called the photon. By virtue of being massless and uncharged, photons can travel infinitely, such that particles interact electromagnetically over very long distances.

The weak and strong forces interact only at much smaller distances, e.g. inside atomic nuclei. For the strong force, the analogy of electromagnetic charge isn't simply positive or negative. Instead, particles can have color charge, which can be red, blue, or green. Quarks are the only colored fermions and the gluon is the strong force carrier. Gluons are massless, but contrary to the photon, gluons are colored so they will interact with other gluons. As a result, the strong force exhibits a property called *confinement*, where colored combinations of particles are unstable³. Individual quarks or gluons cannot therefore be directly observed (see Sec. 2.2.2.4), so the strong force doesn't interact over long distances. Instead, quarks tend to come in colorless groups (*hadrons*) of two (*mesons*) or three (*baryons*)⁴.

If we look at these fermions, we see groups of three: three charged leptons, three uncharged leptons, three up-type and three down-type quarks. Can a fermion transform from one group to another? What about to another fermion in the same group? Through the weak force, quarks can change from up-type to down-type (or vice-versa), e.g. the charm quark can decay into the down quark or the strange

³For electromagnetism, the energy of the total interactions between two charged particles will decrease as the distance between the particles increases. For the strong force, because the gluons themselves have color, the total energy will *increase* with distance. Confinement implies that it is energetically favorable to have colorless states; color charge is literally confined.

⁴There are some experimental results involving tetra- and pentaquarks, but they are very rare and fall well outside of the scope of this thesis.

CHAPTER 1. INTRODUCTION

quark. Further, charged leptons can change from one to another, e.g. the muon can decay into the electron. The force carriers for this decay are the W^\pm bosons, which have either positive or negative unit charge. Also associated with the weak force is the Z^0 boson, which is not charged but can still transfer momentum. But if the strong force is distance limited by confinement, why does the weak force only act over short distances?

Finally, we come to mass. The reason that the charged leptons or up-type quarks aren't fully interchangeable is because they vary drastically in their mass. This has demonstrable impact on how a particle will act, as particles with higher mass will decay to those allowed which have lower mass. A muon is roughly 200 times more massive than the electron, so a muon will quickly decay to an electron. Similarly, the mass of the top quark is much heavier than any other quark, so it has a very, very short lifetime. The weak force acts differently than electromagnetism because while the photon is massless, the W^\pm and Z^0 bosons are massive; the W^\pm and Z^0 will quickly decay, usually to a pair of fermions. As a result, the first generation of fermions – those with lowest mass: the electron, the up quark, and the down quark – are the most stable. With just these three particles, we can make basic protons (two ups and a down) and neutrons (two downs and an up) which combine with the electron to form all of the atoms in the periodic table.

All of the particles listed so far make up matter. In addition, there are antiparticles which have the same mass, but the opposite properties. The anti-electron is

CHAPTER 1. INTRODUCTION

the *positron* as it is positive. Anti-quarks have the same name but with a bar on top, so \bar{u} is the anti- u . Anti-quarks have color of anti-red, anti-green, or anti-blue. Mesons, for example, are a quark and anti-quark pair which add up to a colorless state. As the name implies, when antimatter and matter come in contact with each other, they annihilate, converting into force carriers. Force carriers can then split into matter and antimatter.

One final complication comes from the *uncertainty principle*. In quantum mechanics, the uncertainty principle dictates that complementary variables (e.g. position and momentum, or energy and time) cannot simultaneously be measured to infinite precision. This has consequences that underlie all of modern physics, not the least of which is that particles can violate the energy-momentum relationship⁵ so long as it is only for a correspondingly brief amount of time. These *virtual* particles can never be observed directly, but still impact calculations and observations in particle physics. Protons are better thought of as not being composed only of two up quarks and a down quark, but also the interacting gluons and a sea of temporary quark-antiquark pairs, popping in and out of existence.

⁵Einstein's famous relationship between total energy, momentum, and mass: $E^2 = p^2c^2 + m^2c^4$.

CHAPTER 1. INTRODUCTION

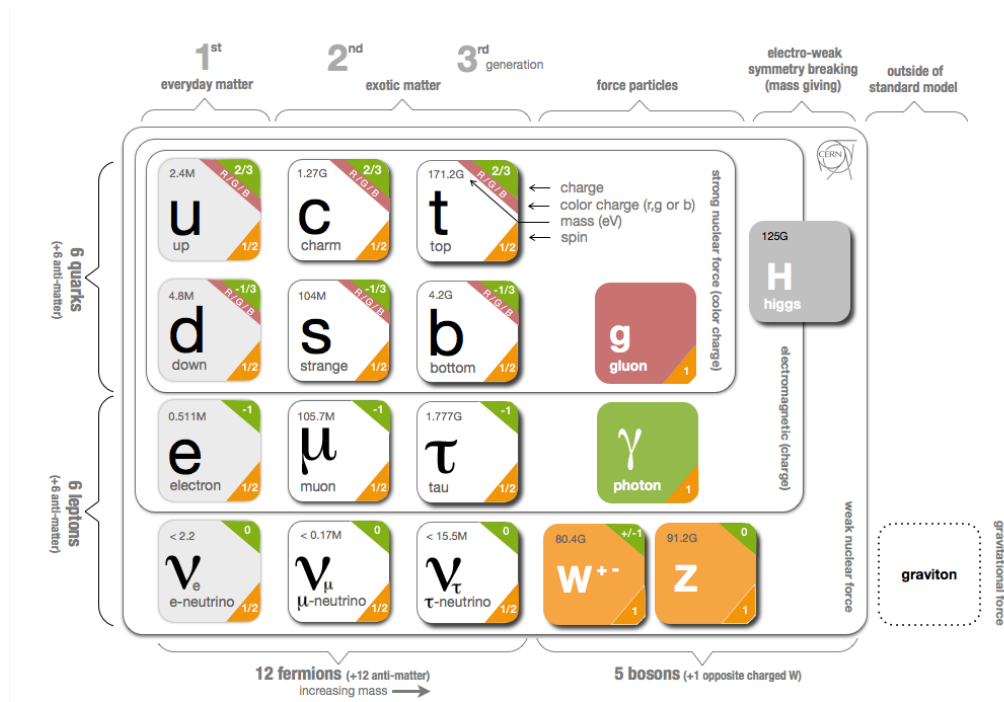


Figure 1.1: The Fundamental Particles of the Standard Model and their Properties. Masses are listed in units of eV/c^2 , a convenient unit⁶ for quantifying subatomic masses. The graviton, a hypothetical particle associated with gravity, is also shown. Plot is a modified from [1].

Before the LHC was turned on, this (Fig 1.1) was the status of the observed particles and properties of the Standard Model. Absent from this picture is the Higgs boson. To understand the role of the Higgs boson and the importance of its discovery, we need to step back and motivate the Standard Model itself.

⁶From here onwards, we will use natural units for convenience where $c = 1$. Energies and masses will interchangeably have eV units with SI prefixes.

1.1.2 The Story: The Status of the Standard Model Before the LHC

Trying to encapsulate the entire universe at once is undeniably intimidating. Fortunately, over centuries of development, physicists have established an arsenal of tools to make the task a bit more manageable. One of the most powerful techniques available is to locate and utilize a symmetry in the phenomenon to be considered; a planet should rotate around a star in the same fashion whether it's moving clockwise or counterclockwise. More than just identifying the symmetry to help simplify a problem, Noether's Theorem states if a system has a particular symmetry it inherently has an associated observed quantity. These examples are prolific, forming the basis of even introductory physics:

Conservation of Energy: Time invariant Lagrangians⁷ conserve energy.

Conservation of Momentum: Translationally invariant Lagrangians conserve momentum.

Conservation of Angular Momentum: Rotationally invariant Lagrangians conserve angular momentum.

Symmetries themselves divide into two categories: global and local. Global symmetries apply to each point in the system equally, whereas local symmetries

⁷Lagrangians, referred to by \mathcal{L} , are mathematical formulations which detail the dynamics of a given system.

CHAPTER 1. INTRODUCTION

apply to individual points in the system. To picture the difference, imagine a grassy field where thousands of identical red balls have been placed in a grid. When you rotate all of the balls 10 degrees, this is a global transformation. If you rotate just one ball 10 degrees, this is a local transformation. In either case, the orientations of the balls will not appear to have changed, so the system has both a global and a local symmetry.

The entire Standard Model can be described by only a few symmetries. Globally, the Standard Model obeys *Poincaré symmetry*, which encapsulates all the symmetries we expect: translational (dynamics are invariant of location), rotational (dynamics unchanged by fixed rotation), time (dynamics will be identical regardless of when they start), and boosts (dynamics don't change if the whole system is moving at a uniform speed). Further, the Standard Model has three local symmetries which correspond to each of the three forces covered by the SM. Each of these local symmetries is called a *gauge symmetry* and has associated bosons called *gauge bosons* whose number is determined by the number of free parameters of the symmetry.

Electromagnetism, for example, has a gauge symmetry defined by $U(1)$, the group associated with rotations about one axis. Since these rotations are only defined by one angle, there should be just one gauge boson associated with electromagnetism. As explained in Sec. 1.1.1, the Standard Model has exactly that: the photon is this gauge boson. Indeed, gauge bosons are force carriers and vice versa.

CHAPTER 1. INTRODUCTION

The weak force has a local symmetry of $SU(2)$ and thus should have three gauge bosons⁸, which appear at first glance to match the W^\pm and Z bosons. The strong force has a local symmetry of $SU(3)$ and has eight gauge bosons which match the eight gluons⁹. Thus, we have our picture of fundamental fermions exchanging these gauge bosons to interact with one another.

However, mass has not yet been motivated. In fact, gauge bosons are mathematically required to be massless particles. Although the photon and the gluons are massless, why do the W^\pm and Z^0 bosons have mass? The mass hierarchy of the fermions is also absent: if the top and up have otherwise identical properties, why is the top's mass over 75,000 times greater than the up? More problems arise: if matter and antimatter annihilate when they collide, why is there more matter than antimatter? And what about gravity? These are the deeper concerns of the Standard Model. Fortunately, there are answers that, if correct, could leave signatures we could find in particle accelerators.

1.1.2.1 Searching for Professor Higgs' Boson

Another common theme motivating the SM and physics beyond the SM is the idea of unification, all forces are simply different aspects of a single force. In 1961, Sheldon Glashow observed that electromagnetism and the weak force could be

⁸For brevity, the explanation for the number of bosons implied by $SU(N)$ and the mathematics behind these groups are not provided, but detailed further in [2]

⁹Of these eight linearly independent color states, there are six colored states and two colorless states. Aside from a brief reprise dealing with hadronization in Sec. 2.2.2.4, the strong force doesn't relate to the remainder of this thesis. Further information can be found at [3]

CHAPTER 1. INTRODUCTION

unified in the electroweak interaction [4]. In short, the unified $U(1) \times SU(2)$ electroweak theory has one boson associated with $U(1)$ (B^0) and three bosons associated with $SU(2)$ (one neutrally charged W^0 and two charged bosons, W^+ and W^-). This symmetry is then broken such that the photon and Z^0 are mixtures of both the B^0 and W^0 . Breaking a gauge invariance can introduce mass terms for the gauge bosons, so while the photon will be massless, the W^\pm and Z^0 will be massive. This does provide the desired result, but it shifts the burden; there ought to be an explanation why this symmetry is broken. Shortly after this unification was proposed, a framework was proposed which explains how a gauge symmetry could be spontaneously broken instead of explicitly broken [5–9]: the *Brout-Englert-Higgs Mechanism*¹⁰.

The Brout-Englert-Higgs mechanism details that there is a field that fills all of space and interacts with the particles of the Standard Model. How this gives a broken symmetry is best illustrated by looking at the associated potential. At high energies, we can picture the potential to be a symmetric valley centered around a point. In that case, the lowest energy state is stable and symmetric: if we imagine a ball rolling in such a structure, it would always come to the lowest point and the symmetry is preserved. But, as the universe cooled, the Higgs potential changed to what is seen in Fig. 1.2, commonly referred to as the “Mexican-hat” or “champagne

¹⁰At the time of development, there were many simultaneous developments, so the name of the mechanism has alternative names, the most thorough of which is the ABEGHHK’tH Mechanism, named for Anderson, Brout, Englert, Guralnik, Hagen, Higgs, Kibble, and ’t Hooft. Often, this is shortened to the “Higgs Mechanism”.

CHAPTER 1. INTRODUCTION

bottle potential". As the ball started at the top of the bulge, it would fall to a lower energy state in the circular valley. Clearly, the symmetry that was preserved in the early universe would then be broken.

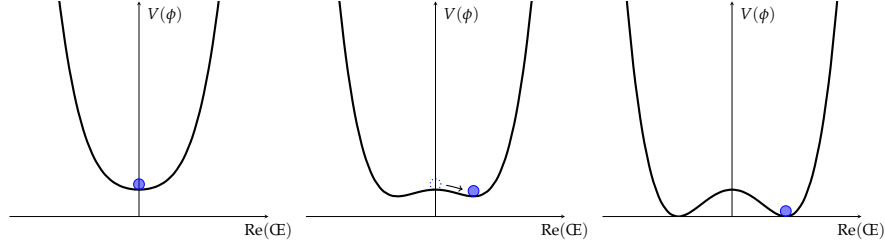


Figure 1.2: The Higgs Potential is a quartic potential with a negative quadratic term. This change in sign gives a ring¹¹ of energetically favorable values, which provide the spontaneous symmetry breaking required by the Standard Model.

This mechanism, along with the other fundamental forces and particles, was summarized into the Standard Model by Weinberg and Salam [10, 11]. In doing so, we have a natural explanation for the massless photon and massive W^\pm and Z^0 that we require. The massive Z^0 in particular had only been predicted when the Standard Model was finalized in the late 1960s, but in the coming decades it was observed indirectly in the 1970s [12] and then directly in the 1980s [13–15]. On top of making the W^\pm and Z^0 massive, by breaking the Electroweak symmetry fermions acquire a mass proportional to how strongly they couple to the Higgs field. This explains why the top and the up have such greatly differing masses.

¹¹Where $V(\phi)$ is the potential, ϕ is complex and the plots are rotationally symmetric in the complex plane, giving a ring of minima.

CHAPTER 1. INTRODUCTION

Crucially, the completion of the Standard Model with the Higgs mechanism from an experimental perspective is to confirm that the Higgs field exists and does generate the masses as described. The final prediction of the Standard Model is that there should be excitations of the Higgs field which manifest as the *Higgs boson*, an uncharged zero-spin particle. The strength that bosons and fermions couple to the Higgs field is determined by the mass of the Higgs boson, so the only unknown in the SM before the LHC was what this mass is.

Before the LHC, all attempts to find the Higgs boson had been elusive. Theoretically, $m_H \lesssim 1$ TeV otherwise there would be large instabilities in the universe that would have already been observed [16]. A lower bound on the Higgs mass was set at LEP, an electron-positron collider, where $m_H > 114.4$ GeV [17] at the 95% confidence level. From measuring properties of the SM to higher and higher precision, the Higgs mass was expected to be found in the mass range $m_H \lesssim 185$ GeV. Since the exact Higgs mass was not known and these excitations should be extraordinarily rare, the best chance to find the predicted Higgs boson would be a general purpose detector at a particle accelerator that covers a wide range of energies with a very high throughput. The Tevatron is such a collider and its general detectors, D0 and CDF, further excluded the Higgs boson from having a mass between $160 < m_H < 170$ GeV [18], leading to the status showing in Fig. 1.3 In Sec. 2, we argue that the CMS detector at the LHC is ideal for extending this search.

CHAPTER 1. INTRODUCTION

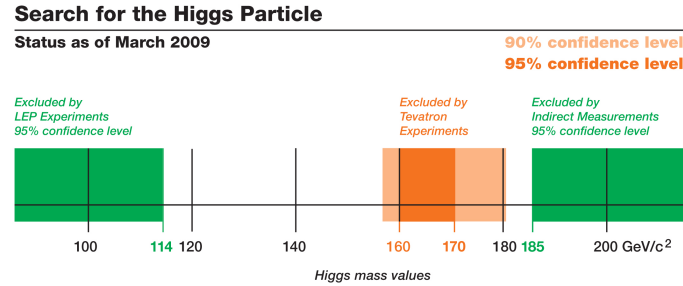


Figure 1.3: Before the LHC, the Higgs Boson’s mass was excluded to 95% confidence in the ranges $m_H < 114.4$ GeV and $160 < m_H < 170$ GeV via direct experimental results, and $m_H > 185$ GeV via indirect measurements.

1.1.2.2 Expecting the Unexpected

Adding the Higgs Boson to our cast of fundamental particles completes the Standard Model, but there are still remaining difficulties:

Matter v Antimatter

The universe was created with equal amounts of matter and antimatter. Matter and antimatter annihilate when they interact, yet the visible universe is largely made of matter. The current theoretical explanation for this asymmetry is that there are particles and decays that would have a preference for matter over antimatter [19]. Although some of this asymmetry has been predicted and observed, neither are sufficient to account for the relative lack of antimatter.

CHAPTER 1. INTRODUCTION

Gravity

Gravity is absent from the SM. Its inclusion is extraordinarily difficult. Gravity is many orders of magnitude weaker than any of the other three forces and must appear like General Relativity at large distances, but currently quantum models of gravity break down at very small distances.

Neutrino Masses

In the SM, neutrinos are not predicted to have mass, yet they have been observed to oscillate between different generations [20]. In order to account for these oscillations, the neutrinos are required to have different masses and thus must be massive. Although theoretical models exist to give neutrinos mass, the masses have not yet been measured.

Dark Matter and Dark Energy

Current estimates of the universe say that only 4% of all mass-energy is made of the particles in the Standard Model. The remaining 96% is made up of Dark Matter (23%) which seems to only interact gravitationally and Dark Energy (73%) which is responsible for the acceleration of the expansion of the universe.

These questions lead to models that are considered Beyond the Standard Model (BSM) physics. There are two main veins of BSM physics, Supersymmetry (SUSY) and Extra Dimensions. As discussed already, symmetry is a very powerful tool

CHAPTER 1. INTRODUCTION

in theoretical physics. SUSY takes the symmetries available under the SM and adds one additional symmetry which predicts new supersymmetric partners for every particle in the SM. For example, every fermion will have a supersymmetric bosonic partner, e.g. the selectron to the electron or the sbottom to the bottom. These partners could provide answers for some or all of the unresolved questions in the SM. Extra dimensions posits that beyond the four traditional dimensions, three spatial and one time, there are additional dimensions which are not readily observed. Additional particles and properties can be hidden in excitations of these extra dimensions which could also explain these unresolved questions.

These additional particles and properties influence searches at the LHC aside from direct observation. First and foremost, nearly all BSM models would require not just one but multiple Higgs bosons, any or all of which could be probed at the LHC. Thus, even though the Higgs of the SM is most likely to be found in the mass range $114 < m_H < 185 \text{ GeV}$, the search should be extended to look for other resonances which may be Higgs-like that would give credence to BSM physics. Furthermore, each of these particles could have different properties than what we expect in the SM Higgs mechanism. Many theorized explanations of gravity imply the existence of another boson called the graviton. Such a particle would have spin-2 instead of the spin-0 presumed in the SM Higgs, so it is also important to probe the spin of any new particle.

Some new physics comes from looking at high precision measurements which

CHAPTER 1. INTRODUCTION

predicate the discovery of undiscovered fundamental particles, as was predicted with the Z^0 . For example to achieve the matter/antimatter asymmetry, there need to be particles that violate CP-symmetry, where a system's dynamics are identical if all matter is replaced with antimatter (and vice versa) and the spatial coordinates are inverted. As a substantial source of CP-asymmetry needed to explain the matter/antimatter asymmetry has not yet been observed, the hope is that new particles would break this symmetry. Even if no other particles aside from a Higgs candidate are found, the SM Higgs is predicted to preserve this symmetry (*CP-even*) and any deviation in the properties from the expected could prove invaluable towards future research into the field of particle physics.

1.2 Summary

As previously mentioned, we now know that there is a Higgs boson, but it is insightful in retrospect to walk through the discovery chronologically to understand the process and appreciate its significance. In Sec. 2, the LHC will be expounded, particularly the CMS experiment and how it was designed to look for a Higgs boson or other new physics. In Sec. 3, the possible production and decay modes of the Higgs boson will be investigated, including the "golden" channel $ZZ \rightarrow 4\ell$, and how it can be used to search and study any Higgs-like resonances. In Sec. 4, largely based on the published result [21], we will review the discovery of a Higgs-

CHAPTER 1. INTRODUCTION

like boson in this channel. In Sec. 5, the observed properties of the new boson will be detailed and how well they match up with what we expect in the Standard Model. Lastly, in Sec. 6, the effects of these results will be summarized and what they mean for future measurements.

Chapter 2

Experimental Setup

"I'm going to find it and I'm going to destroy it. I don't know how yet. Maybe dynamite."

Steve Zissou, "The Life Aquatic with Steve Zissou"

2.1 The Large Hadron Collider

In Sec. 1.1, we saw that although the Standard Model was tested robustly before the LHC turned on, the Higgs boson had not yet been discovered and there are still unanswered questions not covered under the Standard Model that should lead to new physics. For many decades, the primary tool of discovery in experimental particle physics has been the particle accelerator. In rudimentary terms, two particles are accelerated towards each other and the byproducts of their collisions are studied to look for new particles.

CHAPTER 2. EXPERIMENTAL SETUP

There are two categories of particle accelerators, leptonic and hadronic: leptonic colliders have electron-positron collisions while hadronic colliders use proton-proton or proton-antiproton collisions. As discussed in Sec. 1.1.1, protons are made up of a sea of different particles with varying energies, making it difficult to know the exact initial conditions of a collision. A leptonic collider, on the other hand, can tune the initial energy of the collisions to a precise value with strictly designed initial conditions. However, as argued in Sec. 1.1.2.1 and 1.1.2.2, the proposed particles could take many energy values, so any search must be done over a wide range, which should also explore unprobed regions out of reach of previous detectors, encouraging the use of hadronic collisions. The highest energy collision before the LHC were at the Tevatron at Fermilab which had a maximum center-of-mass energy up to about 2 TeV (2000 GeV).

The Large Hadron Collider was designed with these characteristics in mind: a 27-kilometer circular accelerator for proton-proton¹ collisions that can reach up to energies² of 14 TeV. An earlier proton-proton accelerator, the Super Proton Synchrotron which found direct evidence for the Z boson [13–15], initializes the proton bunches at 450 GeV for injection into the larger ring. Once reaching the LHC, a series of 1232 superconducting dipole magnets with radio frequency cavities increase the energy of the protons as they move around the ring. As these bunches

¹The tunnel was originally used for LEP, to collide electrons and positrons. Heavy ions can also be accelerated in the LHC, leading to interesting research for the strong force, but this is outside the scope of this thesis.

²Although the LHC was designed for higher energies, the results of this thesis will focus on the first runs which were at 7 and 8 TeV.

CHAPTER 2. EXPERIMENTAL SETUP

accelerate, the protons will tend to diffuse, so thousands of additional magnets (quadrupole, octopole, etc) are installed to focus the beam. Each bunch in the LHC contains 1.15×10^{11} protons and every run contains 2808 bunches. These high populations are required to probe the highest energies and rarest interactions expected at the LHC.

To quantify the probability of a process occurring in a given collision, physics utilizes the concept of *cross section* (σ). This is best illustrated by comparing protons in a bunch to a flow of ballbearings: as two bunches pass through one another, the likelihood that any ballbearing strikes another is proportional to their size, literally their cross-sectional area. Similarly, in quantum physics, the likelihood of an event is determined by its cross section, typically written in units of *barns* (b) where $1 \text{ b} = 10^{-28} \text{ m}^2$. The processes intended to be probed at the LHC have cross sections ranging from the order of picobarns ($1 \text{ pb} = 10^{-12} \text{ b}$) to fractions of femtobarns ($1 \text{ fb} = 10^{-15} \text{ b}$).

Particle accelerators use *luminosity* (\mathcal{L}) to indicate the expected flux of collisions to determine how many events of a given cross section should be expected per second, i.e. $\frac{dN}{dt} = \mathcal{L} \times \sigma$. The luminosity can be defined in terms of the accelerator's parameters:

$$\mathcal{L} = \frac{\gamma f k_B N_p^2}{4\pi\epsilon_n \beta^*} F$$

where γ is the Lorentz factor corresponding to how fast the particles are moving, f is the frequency that bunches revolve through the LHC, k_B is the number

CHAPTER 2. EXPERIMENTAL SETUP

of bunches, N_p is the number of protons in a bunch, ϵ_n (normalized transverse emittance) and β^* (betatron function at the point of interaction) both relate to the physical size of the beam, and F is a reduction factor caused by the crossing angle of the beams. Relevant design parameters are also found in Table 2.1. Ultimately, the design luminosity of the LHC is $\mathcal{L} = 10^{34} \text{ cm}^{-2}\text{s}^{-1}$ which corresponds to about 1 billion proton-proton interactions per second. To quantify the total amount of data collected by a particle detector, time-integrated luminosity, in units of fb^{-1} , is used to gauge how many events of a given cross-section should be expected. For example, with 10 fb^{-1} of data, one would expect 10 events for a cross-section of 1 fb.

Number of bunches	k_B	2808
Number of protons/bunch	N_p	1.15×10^{11}
Bunch separation		25 ns
Design Luminosity	\mathcal{L}	$10^{34} \text{ cm}^{-2}\text{s}^{-1}$

Table 2.1: Design Parameters of the LHC

After reaching the desired energy, the proton bunches can interact at four crossing points. Each of these points is the site of a detector on the LHC: CMS (The Compact Muon Solenoid), ATLAS (A Toroidal LHC Apparatus), ALICE (A Large Ion Collider Experiment), and LHCb (LHC beauty Experiment). CMS and AT-

CHAPTER 2. EXPERIMENTAL SETUP

LAS are general purpose detectors for proton-proton interactions, while LHCb uses proton-proton collisions to study the physics of the b quark and ALICE uses the protons to collide with heavy-ion targets to look deeper into the intricacies of the strong force. The remainder of this chapter will detail CMS and how it is used to search for particles like the Higgs.

2.2 Our Setting: The Compact Muon Solenoid

The Higgs Boson and theorized particles in BSM physics are largely expected to be unstable³ and rapidly decay to particles of the Standard Model, so it's unsurprising that the design requirements of the CMS are built around accurately detecting these particles and characterizing their energies and momenta. To collect the most information about these events, a detector should be designed to record all decay chains so that the full kinematics could be reconstructed. This is the idea behind a *hermetic* detector: different subsystems are nested to capture information about any particle observed and characterized by what sub-detectors they interact with. With all particles accounted for, any missing energy can also be quantified. A detailed view of the CMS detector is seen in Figure 2.1. This section will overview the subsystems, where further details are found in the CMS Technical Design Reports [22,23].

³Some theoretical particles, like certain candidates for dark matter, will have longer lifetimes and may pass through CMS undetected. However, this would appear as a large source of missing energy.

CHAPTER 2. EXPERIMENTAL SETUP

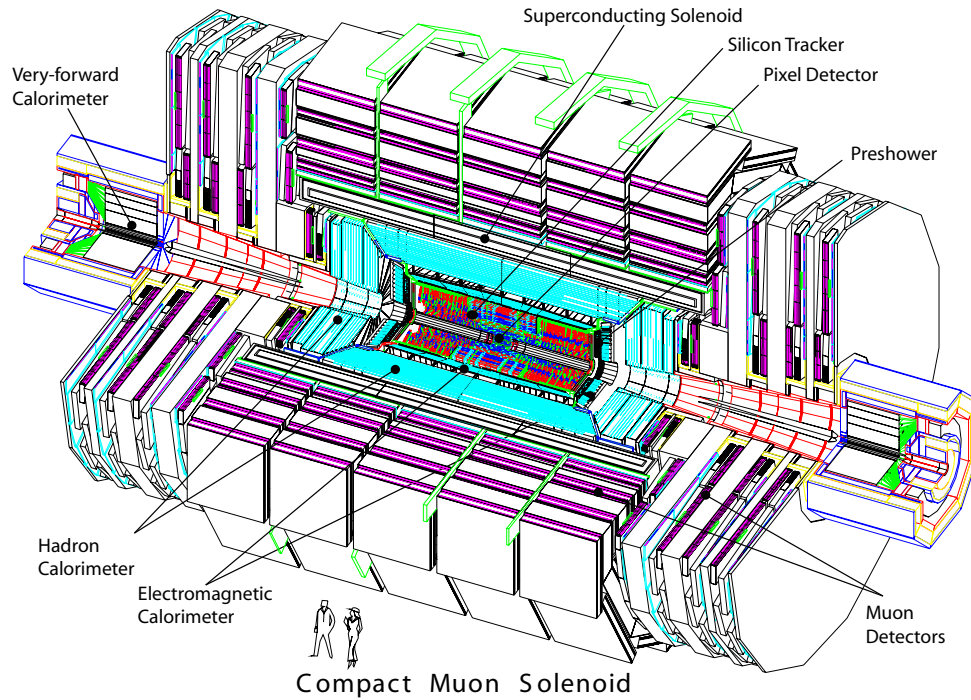


Figure 2.1: The CMS detector is built around the interaction region, with the silicon tracker and pixel detector (Sec. 2.2.2.2) are at the innermost radii to track particles as they are created. Outside the tracker system, the the calorimeter systems (Sec. 2.2.2.3 and 2.2.2.4) are close to the superconducting solenoid (Sec. 2.2.2.1). Lastly, the muon system (Sec. 2.2.2.5) is found on the outer shell. Two human figures are used for scale.

2.2.1 Coordinates and Conventions for the CMS

To unambiguously define locations for components or events found in the detector, a standard coordinate system is used such that the origin is centered at the nominal collision point. In cartesian coordinates, the y -axis is defined to be vertically upward while the x -axis is points toward the center of the LHC accelerator ring. However, given that the detector is cylindrically symmetric, directions are commonly defined using ϕ and η . ϕ is the azimuthal angle starting from the x -axis in the $x - y$ plane. η is the *pseudorapidity* where $\eta = -\ln[\tan(\theta/2)]$, θ being the polar angle measured from the z -axis. Momentum and energy are then broken into their transverse (away from the axis, e.g. p_T, E_T) and longitudinal (along the axis, e.g. p_z, E_z) components. The beam is very near the axis and, in addition to low p_T QCD processes, would cause a sizable background, so particles that have large p_T or E_T (or in the case of searching for energy imbalance, E_T^{miss}) should be the easiest to identify unambiguously.

2.2.2 Subsystems in CMS

2.2.2.1 The Magnet

One way to categorize the decay products of a particle is to look at their charges. Any charged particle will have a curved trajectory in a magnetic field, where the direction of curvature is determined by the sign of the charge and the scale of the

CHAPTER 2. EXPERIMENTAL SETUP

curvature is proportional to the momentum. Given the large energies and desired precision of the momenta, the magnetic field must be very strong and consistent. CMS uses a 12.9m long, 5.9m in diameter superconducting solenoid with a designed field strength of 4T, about 100,000 times that of the Earth's magnetic field. An iron return yoke, running through the muon system, is used to guide and return the field. In doing so, the magnetic field in the muon system will be antiparallel and of lower magnitude than the field in the calorimeters and tracking systems.

2.2.2.2 Inner Tracking System

Searches for the Higgs boson and the determination of its properties will largely, as we will see in Sec. 4 and Sec. 5, depend on precise determination of decay chains and the kinematics of their decay products. To determine interaction vertices and precisely measure the momentum of particles, CMS uses a tracker system, which uses combinations of silicon pixels and strip sensors to record hits when charged particles pass through each element. These hits can then form trajectories to track the particles as they move through the innermost radii of the detector. The full geometry of the tracker system, with pixel and strip trackers, can be seen in Fig. 2.2.

As particle flux will clearly be highest closest to the interaction point, the smallest elements must be placed to avoid oversaturating the electronics. Silicon pixels of size $100 \times 150 \mu\text{m}^2$ are arranged in three cylindrical barrel layers at $r = 4.4 \text{ cm}$, 7.3 cm , and 10 cm each with a length of 53 cm plus two endcap annuli at $|z| =$

CHAPTER 2. EXPERIMENTAL SETUP

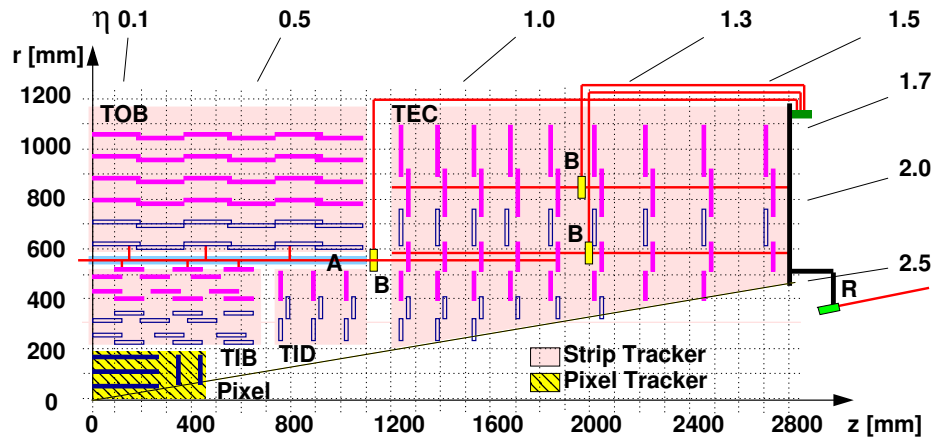


Figure 2.2: Tracker cross-sectional slice (1/4 of the z view). The pixel tracker is located at the innermost radii of the detector and is labeled in striped yellow. The strip tracker is composed of four regions: Tracker Inner Barrel (TIB), Tracker Outer Barrel (TOB), Tracker End Cap (TEC), and Tracker Inner Disks (TID). The blue pieces are double-sided strip-only modules while magenta are single-sided.

CHAPTER 2. EXPERIMENTAL SETUP

34.5 and 46.5 cm with radius from $r = 6$ cm to 15 cm. The pixels are arranged in modules with read-out chips (16 per module in the barrel, 2-10 per module in the endcap), each of which reads the output of an array of 52×80 pixels. The output and location of any active pixels are stored in a buffer, awaiting decision to be stored permanently or not from the Level-1 Trigger (see Sec. 2.2.4).

Outside of the pixel layers, the particle flux per unit area will be lower. Tracker elements can be a bit larger without oversaturating, so silicon microstrips are used (minimum cell size of $10 \text{ cm} \times 80 \text{ }\mu\text{m}$ for $20 < r < 55$ cm and $25 \text{ cm} \times 180 \text{ }\mu\text{m}$ for $r > 55$ cm). The strip tracker is divided into four regions, named to indicate their location in the tracker subsystem: Tracker Inner Barrel (TIB), Tracker Outer Barrel (TOB), Tracker End Cap (TEC), and Tracker Inner Disks (TID). The TIB consist of four layers covering $|z| < 65$ cm while the TOB covers $|z| < 110$ cm and is made of six layers. By the orientation and size of the components, the barrel has single-point $r - \phi$ resolution of $23\text{-}34 \text{ }\mu\text{m}$ ($35\text{-}52 \text{ }\mu\text{m}$) and z resolution of $230 \text{ }\mu\text{m}$ ($530 \text{ }\mu\text{m}$) in the TIB (TOB). For the endcap region, the TID is made of three rings that fill the space inside the r range of the TOB and outside the z range of the TIB while the TEC is made of 9 rings stretching from $120 < |z| < 280$ cm. As the radiation is even smaller in the outer regions of the tracker, the strips can be longer and thicker. In the TOB and six outermost layers of the TEC, the sensors are slightly thicker at $500 \text{ }\mu\text{m}$ compared to the $320 \text{ }\mu\text{m}$ thick sensors elsewhere. By associating multiple tracker hits, trajectories of charged particles can be constructed. The ulti-

CHAPTER 2. EXPERIMENTAL SETUP

mate designed global track efficiency can be seen for muons and pions (the lightest meson) in Fig. 2.3. Overall efficiency decreases for smaller p_T and near the edges of the detectable region.

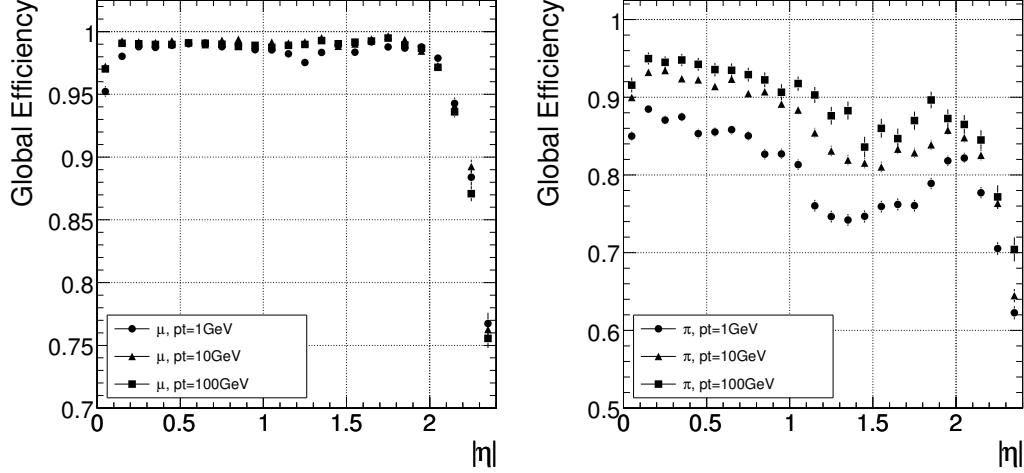


Figure 2.3: Global track reconstruction efficiency of muons (left) and pions (right) for transverse momenta of 1, 10, and 100 GeV/c.

As the tracker subsystem is the only one that can reconstruct vertices, great care is taken to affirm that the numerous pieces of the tracker are aligned to very high precision (ideally smaller than the single-point resolution, so $\lesssim 10\mu\text{m}$). After construction, an optical survey was used to calibrate the tracker⁴, as well as other subsystems, to account for shifts in orientation. However, this method primarily accounts for large scale structure and not individual module misalignments. In sum, there are 9.6 million strips and 66 million silicon pixels spread across over

⁴A laser alignment system was built for the tracker system, but was ultimately not as powerful as the optical survey so it was never used.

CHAPTER 2. EXPERIMENTAL SETUP

16588 modules, where the position and orientation of each must be tracked independently both before and during operation of CMS. The only way to account for all modules and get the desired detector position resolution is to use track-based alignment.

After measuring the positions of the various devices during construction and utilizing the optical survey information, trajectories of known particles can be used to further the alignment. If individual module positions are not known correctly, there will be a systematic difference⁵ between the measured hit position and the trajectory impact points, known as a *residual*. Ultimately, the idea of track-based alignment is to find the needed corrections for each module by minimizing the χ^2 function,

$$\chi^2(\mathbf{p}, \mathbf{q}) = \sum_j^{\text{tracks}} \sum_i^{\text{hits}} \mathbf{r}_{ij}^T(\mathbf{p}, \mathbf{q}_j) \mathbf{V}_{ij}^{-1} \mathbf{r}_{ij}(\mathbf{p}, \mathbf{q}_j) \quad (2.1)$$

where \mathbf{r}_{ij} defines the residual of a hit for a particular track, \mathbf{q}_j are the track parameters, \mathbf{V}_{ij} is the covariance matrix between the residuals, and \mathbf{p} are the desired corrections.

Two statistical methods are used to find the corrections. One algorithm globally minimizes χ^2 , *Millipede* previously used at other experiments [24], by accounting for the track parameters and corrections simultaneously. Computationally, to find the individual module corrections, it is equivalent to minimizing a matrix equation for $O(10^5)$ degrees of freedom, which is extraordinarily intensive. How-

⁵In local coordinates for an individual module, which can be up to six parameters: three translational and three rotational deviations.

CHAPTER 2. EXPERIMENTAL SETUP

ever, using a reasonable starting point, it will converge in an acceptable amount of computation time. Alternatively, a local iterative algorithm [25], using the Kalman filter reconstruction algorithm [26], assumes no track parameter dependence in Eqn. 2.1, simplifies the minimization considerably. The track parameters and correlations between different modules are accounted for by iterating the minimization multiple times. Each of these algorithms yield consistent results and are used in tandem for the full tracker alignment.

In 2008, when the detector was fully constructed but the beam was not yet running, millions of cosmic muons were tracked through the detector. Using a combination of global and local techniques, the positions of the modules were determined to an average precision of 3-4 μm in the barrel and 3-14 μm in the endcap in their respective most sensitive coordinate [27]. Since environmental conditions of operation can cause deviations over time, similar alignment strategies are used by CMS during data collection.

Although crucial to searches at CMS, not all particles will leave trajectories in the tracker sub-system. Any uncharged particles, like photons, will pass through without depositing any hits. To account for these particles and to complete the kinematics of charged particles, the energies of particles must be quantified, requiring the use of calorimeters.

CHAPTER 2. EXPERIMENTAL SETUP

2.2.2.3 Electromagnetic Calorimeter

In order to detect electromagnetic particle energies at CMS, an electromagnetic calorimeter (ECAL) made of lead tungstate (PbWO_4) barrel crystals (61200 such crystals in the barrel [$0 < |\eta| < 1.479$], 7324 in the endcaps [$1.479 < |\eta| < 3.0$]) is built just outside of the inner tracking system. As the name implies, this sub-detector is designed to detect particles that predominantly interact electromagnetically, namely photons and electrons. As photons and electrons pass through a dense transparent material, they will interact with the heavy nuclei therein. Electrons have their paths diverted by the strongly positively charged nuclei in a process called *bremsstrahlung*, where the diversion will emit a photon. Meanwhile, photons of a sufficient energy can *pair produce* in the presence of a heavy nucleus, decaying into an electron and positron pair. The combination of these processes produce showers of electrons and photons of lower energy, called *electromagnetic showers*. Muons, though charged electromagnetic particles, are too heavy to initiate these decays and will pass through the ECAL. Other particles which tend to decay via strong processes, like taus and quarks, have longer decay lengths so the products of their decays will tend to be outside of the ECAL.

This electromagnetic showering has two characteristic length scales. The radiation length, X_0 , determines the depth of a shower in the calorimeter while the Moliere radius determines a shower's width. Lead tungstate was chosen because it has short radiation and Moliere lengths (0.89 cm and 2.2 cm, respectively) while

CHAPTER 2. EXPERIMENTAL SETUP

maintaining a fast response time roughly equal to the bunch crossing time. Each of the crystals in the ECAL have a square front facing cross-section (about 22×22 mm² and 28.6×28.6 mm² for the barrel and endcaps, respectively) with a length equal to a large number of radiation lengths ($25.8X_0$ for the barrel, $24.7X_0$ for the endcap) so these electromagnetic showers are fully contained in the ECAL.

Particles that deposit their energy in the ECAL can then be measured by adding the energies of the resultant shower products. Electromagnetic showers in lead tungstate will scintillate, where photons associated with the shower will be absorbed then quickly re-emitted through the crystal. However, the total number of photons at the end of the crystal is comparatively small ($\sim 30 \gamma/\text{MeV}$), so additional electronics are placed to act as photodetectors and amplify the signals. In the barrel, two silicon avalanche photodiodes (APDs) are attached to the far end of each crystal, while vacuum phototriodes (VPTs) are at the end of each endcap crystal. Both the crystals and the APDs are highly sensitive to temperature changes, so the ECAL requires a cooling system to maintain temperature stability.

To test the performance of the crystals, the performance of a supermodule of crystals was measured with a test electron beam before installation. The energy resolution was then parameterized as a function of energy:

$$\left(\frac{\sigma}{E}\right)^2 = \left(\frac{S}{\sqrt{E}}\right)^2 + \left(\frac{N}{E}\right)^2 + C^2 \quad (2.2)$$

where S is the stochastic term coming from random statistical fluctuations, N is the noise from the detector, and C is a constant term. The values of the parameters

CHAPTER 2. EXPERIMENTAL SETUP

and this parameterization as a function of energy are found in Fig. 2.4.

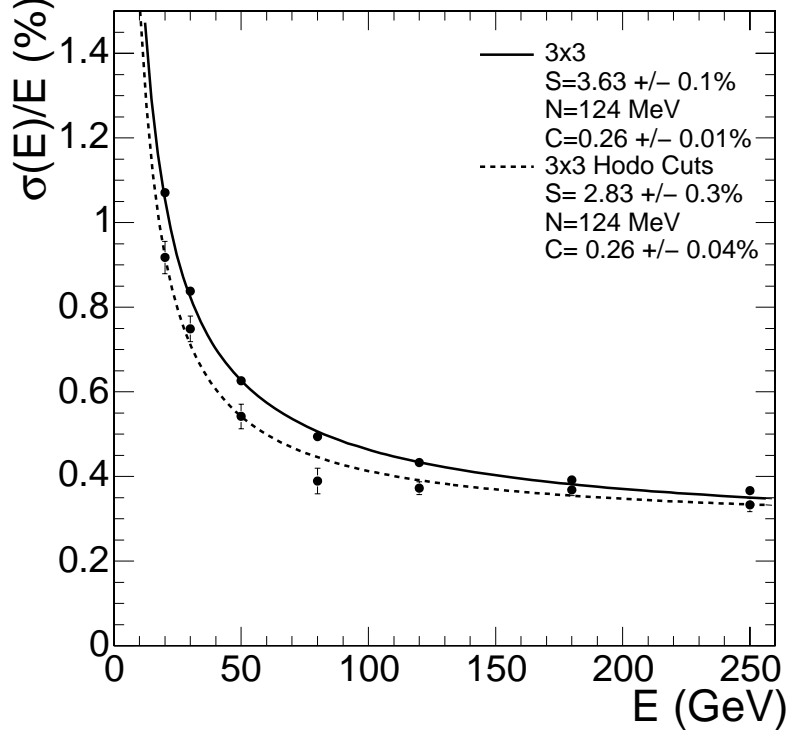


Figure 2.4: ECAL Supermodule Energy Resolution, $\sigma(E)/E$ as a function of the electron energy from the test beam. The solid and dashed lines vary by the area used to reconstruct the energy.

2.2.2.4 Hadronic Calorimeter

For particles that pass through the ECAL, another calorimeter is needed to measure the energy of the hadronic products of CMS, called the hadronic calorimeter (HCAL). As mentioned in Sec. 1.1.1, quarks and gluons cannot be observed in an isolated state, instead being found grouped into hadrons. At particle accelerators,

CHAPTER 2. EXPERIMENTAL SETUP

these hadrons will have a sufficiently high momentum that the constituents will pull apart from one another. However, a property of the strong force is that as two colored particles move apart, the energy of the bond between the particles will increase. This means that at some distance, it becomes energetically favorable for the hadron to split into a pair of hadrons. Simultaneously, the quark or gluon constituents may radiate lower energy gluons, which will similarly tend to split into quarks or gluons. These processes are termed *hadronization* and *fragmentation*, where the end result is analogous to the electromagnetic case: hadronic decay products from an interaction will appear as showers of hadrons and their decays products. These showers are called *jets*.

While the ECAL was made of continuous crystals that could generate and direct the scintillated photons to the photodetectors, the HCAL uses sampling. When jets strike a dense material, there will be some decay in this absorber layer. Then, as these particles pass through a plastic scintillator, they will ionize the material, sending pulses of scintillated photons corresponding to the energy of the products. By alternating these absorber and scintillator layers, the energy of a jet can be found through multiple samples, effectively making energy snapshots of the decay.

In the barrel region ($|\eta| < 1.4$)⁶, there are 32 such layers⁷, segmented into tow-

⁶There is also a hadron outer detector in the barrel $|\eta| < 1.26$ in the muon system that sample the energy penetrating from hadronic showers to reduce contamination.

⁷Their thicknesses are identical except the first layer which is thicker to account for particles that leave the ECAL.

CHAPTER 2. EXPERIMENTAL SETUP

ers of $\Delta\eta \times \Delta\phi = 0.087 \times 0.087$. The absorber layer is made of brass due to its non-magnetic properties and short interaction length. Each scintillating element is embedded with wavelength-shifting fibres which carry the light to multi-channel hybrid photodiodes (HPDs) which apply a gain to the photoelectrons to find the corresponding energy. In the endcap ($1.3 < |\eta| < 3.0$), there are 14 layers identical to the barrel region but with slightly different segmentation ($\Delta\eta \times \Delta\phi = 0.087 \times 5^\circ$ for small $|\eta|$ to $\Delta\phi = 10^\circ$ with $0.09 < \Delta\eta < 0.35$ for larger $|\eta|$). Finally, there is also a hadron forward (HF) calorimeter ($3.0 < |\eta| < 5.0$) built of absorbing layers of steel and quartz fibres, which scintillates and directs light to photomultipliers, segmented into elements of $\Delta\eta \times \Delta\phi \approx 0.175 \times 10^\circ$. A sample output of the HCAL can be seen in Fig. 2.5 while jet energy resolution can be found in Fig. 2.6.

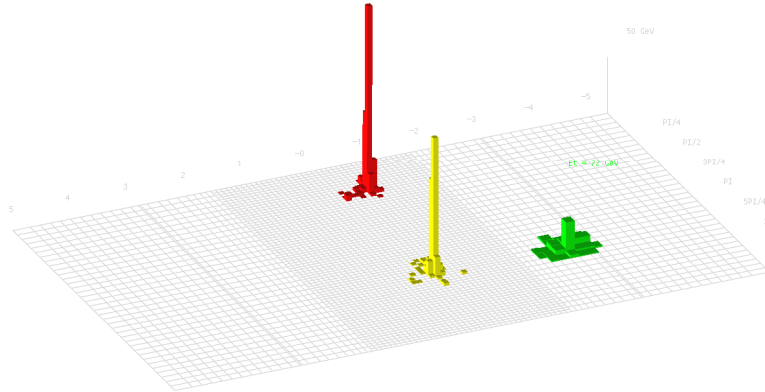


Figure 2.5: Multi-jet event in the HCAL, showing the η, ϕ segmentation over the full range ($0 \leq \phi < 2\pi$, $-5.0 < \eta < 5.0$). Heights correspond to the energy recorded in a particular tower of segments.

CHAPTER 2. EXPERIMENTAL SETUP

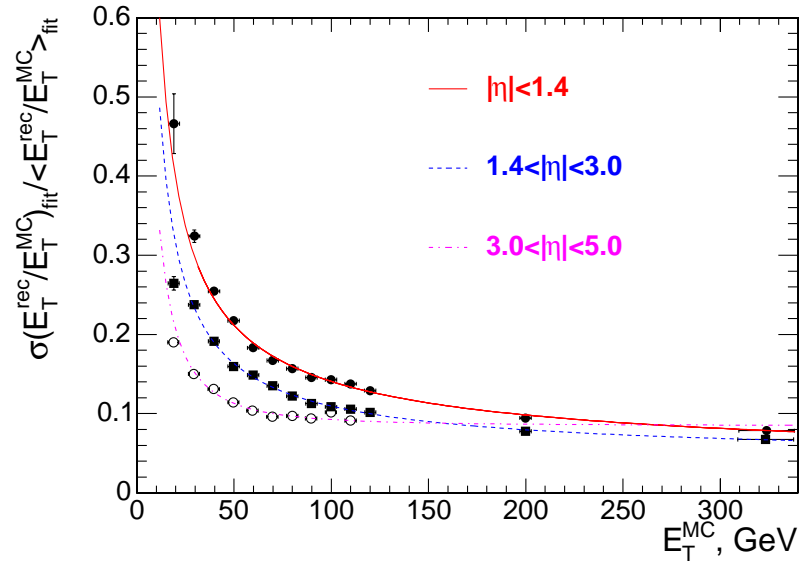


Figure 2.6: Resolution of the transverse energy of jets as a function of the simulated jet energy, discriminated by barrel ($|\eta| < 1.4$), endcap ($1.4 < |\eta| < 3.0$), and forward ($3.0 < |\eta| < 5.0$) regions of the hadronic calorimeter (HCAL).

CHAPTER 2. EXPERIMENTAL SETUP

By unifying the information from the tracker, ECAL, and HCAL systems, CMS can fully detail the energies of all decay products. The only particles of the Standard Model not detected by these systems are neutrinos, which will pass through the detector. However, by the hermetic design of CMS, neutrinos can be accounted for in a given interaction by looking at the missing energy in a given event⁸.

2.2.2.5 Muon System

Muons are one of the cleanest signatures to identify and thus crucial for finding new physics. For charged particles, electrons are common byproducts of many low energy decays and can be stopped in dense material. Tau leptons are much rarer, but have a very short lifetime and thus decay in the inner detector. Quarks cannot be observed individually. Neutrinos aren't charged and very difficult to detect as they only interact via the weak force. Muons, on the other hand, are charged, heavy leptons that have long enough lifetimes to pass through the outer reaches of the detector. Because of these properties, muons that come from collisions are measured both by the tracker sub-system and from three different detecting elements in an outer muon system.

On the outer edge of the detector, three types of detectors are used to measure muons. The layout of the different types of detectors can be seen in Fig. 2.7. Away

⁸Searches are also done looking for anomalously large amounts of missing energy which could account for any number of BSM physics, including microscopic black holes, extra dimensions, weakly interacting massive particles, etc. However, as of writing, no new physics has been observed in these searches.

CHAPTER 2. EXPERIMENTAL SETUP

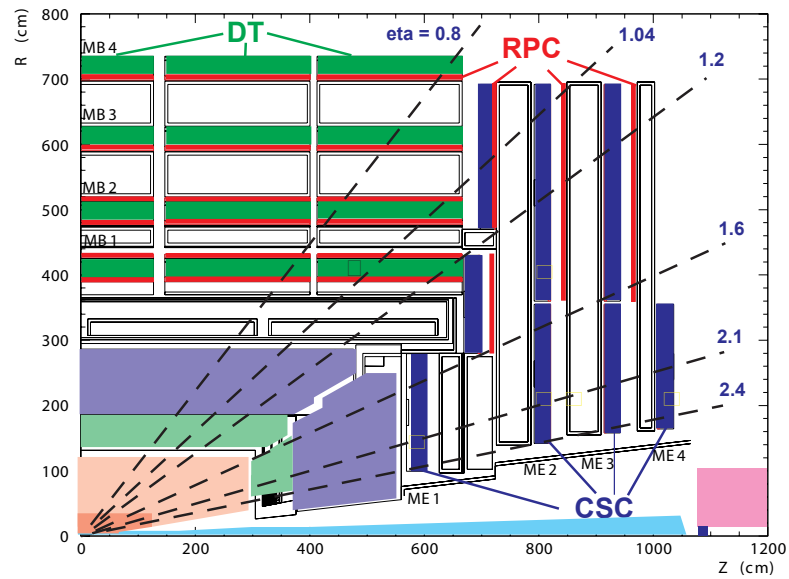


Figure 2.7: Vertical slice of CMS showing one quarter of the muon system. The three different devices used are labeled: Drift Tube (DT) chambers, Cathode Strip Chambers (CSC), and Resistive Plate Chambers (RPC). The inner subsystems are unlabeled but shown where tracker subsystem appears in orange, with the ECAL in green and the HCAL in purple.

CHAPTER 2. EXPERIMENTAL SETUP

from the beam line ($|\eta| < 1.2$), along the barrel, four layers of 250 drift tube (DT) chambers are used. Each chamber is composed of a positively charged wire in a volume filled with gas. As a muon moves through the chamber, the gas becomes ionized and the freed electrons will drift toward the wire. The position of the muon can then be tracked by where electrons were observed to drift. Closer to the beam line (up to $|\eta| < 2.4$), in the endcaps, there are four layers of 468 trapezoidal shaped cathode strip chambers (CSC). Each CSC is made of seven layers of metal, inlaid with a plane of cathode strips plus anode wires nearly perpendicular to the strips. The gaps between metal layers are filled with a gas that will ionize when any charged particle passes through, causing an electron avalanche. Similar to the DTs, these electrons will charge anode wires and cathode strips near the trajectory, allowing spatial reconstruction at each layer.

Finally, in both the barrel and endcap regions ($|\eta| < 1.6$), 1080 resistive plate chambers (RPC) are added in conjunction with the DTs or CSCs. Each RPC consists of two very narrow chambers (2mm thick x 130cm long) filled with gas plus anode and cathode plates made of bakelite, which has a very high resistivity. As with DTs or CSCs, when charged particles pass through the gas, it ionizes and is quickly detected with the bakelite layers. By design, RPCs have worse spatial resolution than either the DTs or CSCs, but their time resolution is much better and they trigger faster, allowing for very rapid identification of muons. This will prove particularly relevant to triggering at CMS in Sec. 2.2.4.

CHAPTER 2. EXPERIMENTAL SETUP

By tracking the muons through these different detectors, their trajectories, and thus their momentum, can be reconstructed. Although most of the resolution power is provided by the inner tracker (see Sec. 2.2.2.2), the outer muon system improves the performance at very high momenta, bringing the overall resolution well below 10% across all expected momenta near the barrel and most momenta ($p \lesssim 2\text{TeV}/c$) in the endcaps, as seen in Fig. 2.8.

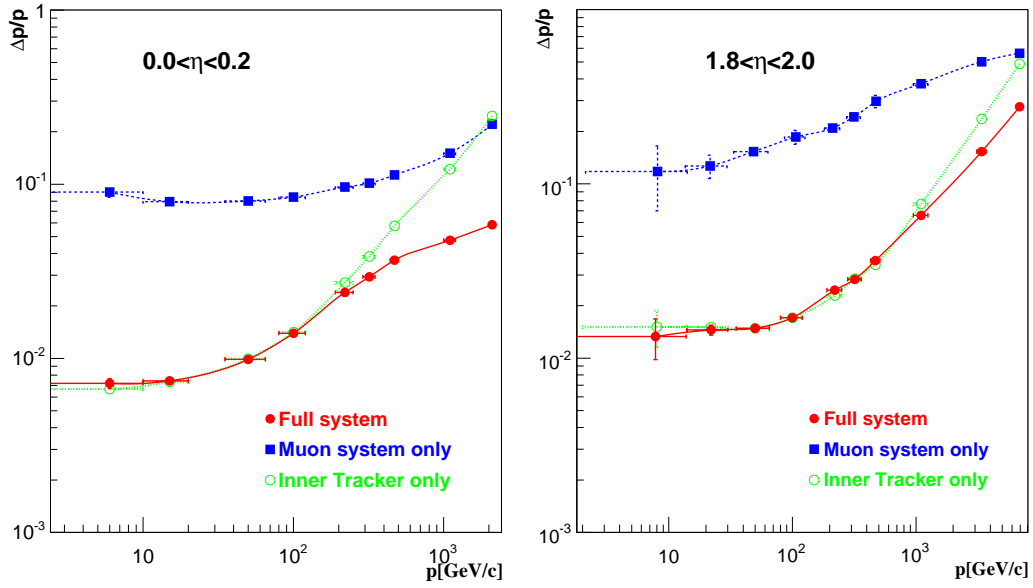


Figure 2.8: Momentum resolution of muons for the muon system only, inner tracker only, or both in the barrel (left) and endcap (right) regions.

2.2.3 Particle Identification

During operation, when the proton beams collide, all of the subsystems work in tandem to identify different particles by what portions they interact with. For example, both muons and electrons will record hits in the tracker, but the muon will move through the muon system while electrons stop in the ECAL. Fig. 2.9 shows a diagram with the expected interactions from a sample set of particles. In theory, it seems like this should be simple categorization: only electrons and photons interact with the ECAL, hadrons will interact with the HCAL, etc. Although it can be this simple, in practice, it is more nuanced. In one crossing, there are roughly 20-30 collisions and each can have multiple decay products which could deposit energies at similar locations. The *particle-flow algorithm* [28] uses the total information from all subsystems to reconstruct individual particles.

By linking the output from the different subsystems, particle-flow can iteratively identify particles. For any charged particles, there will be tracks that should align with energy deposits in the calorimeters or muon system. Any hits in the calorimeters are clustered by looking for local maxima and associating nearby elements that are above threshold. In some cases, additional information can be used with the clustering. For example, in the ECAL, electrons will spread energy over a larger area of crystals than converted photons ($\gamma \rightarrow e^+e^-$). These clusters (or trajectories in the muon system) are then matched to trajectories in the tracker system. Starting with a very tight agreement between the two elements, matched particles

CHAPTER 2. EXPERIMENTAL SETUP

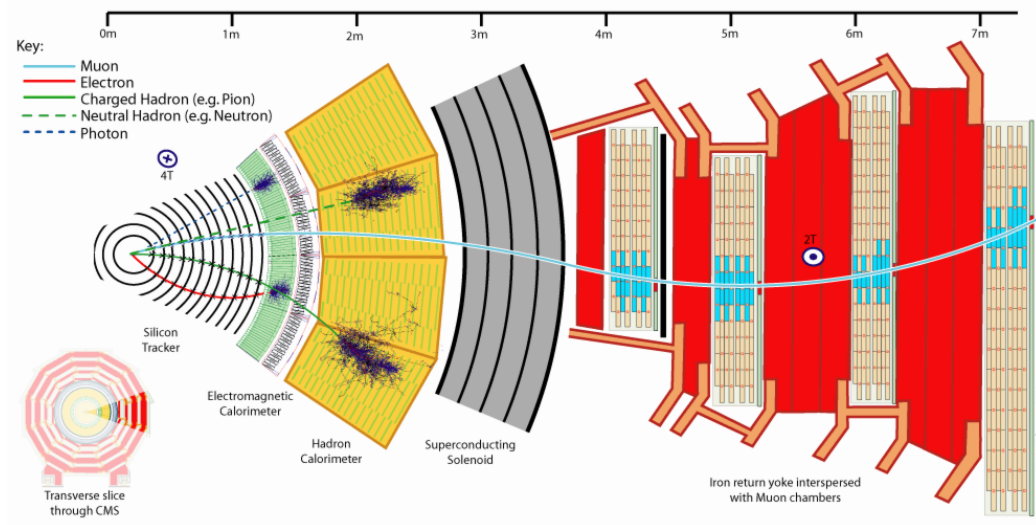


Figure 2.9: Transverse slice of CMS with sample trajectories and decays from expected SM particles. Photons (dashed blue) and electrons will deposit their energy in the Electromagnetic Calorimeter, while both neutral (dashed green) and charged hadrons (green) deposit in the Hadronic Calorimeter. Muons (blue) will move through the muon system. All charged particles will interact with the tracker, leaving curved trajectories.

CHAPTER 2. EXPERIMENTAL SETUP

and their associated hits in the subdetectors are removed from consideration and the algorithm repeats with a looser constraint.

This algorithm removes elements from consideration in a particular order⁹, starting with global muons, then electrons and photons, and finishing with jets. Once all particles are reconstructed, the missing transverse energy can be calculated. Finally, isolation can be used to indicate whether a given reconstructed particle is *prompt*, meaning that it comes from an initial interaction, or alternatively if the reconstructed particle comes from a secondary decay (e.g. a component of a jet). These reconstructed particles form the basic framework of all analyses at CMS.

2.2.4 Triggers

As specified in Sec. 2.1, the intended number of collisions is on the order of 1 billion per second. However, even using state-of-the-art storage technology only about 100 events per second can be stored for later analysis, so nearly all of the collisions need to be rejected. Instead of arbitrarily taking data every hundredth of a second, a trigger system is designed so that only potentially interesting events can be captured. To determine what is interesting, data is temporarily stored and filtered by custom electronics. The first trigger, Level-1, uses custom electronics to

⁹This is roughly in order of resolution for the expected particle, where each identification has little influence on successive identifications.

CHAPTER 2. EXPERIMENTAL SETUP

accept events are only if they either have i) primitive objects¹⁰ from subsystems that pass p_T or E_T thresholds or ii) global E_T or missing transverse energy (E_T^{miss} or MET). The detector elements with fast time resolution, like the RPCs in the muon system (see Sec. 2.2.2.5), define these primitive objects. Altogether, the Level-1 trigger procedure, including data transfer and decision making, is designed to be completed within $3.2 \mu\text{s}$ and reduces the rate of events to approximately 100 kHz.

After passing the Level-1 trigger, software high level triggers (HLT) apply additional processing to further reduce the throughput. Where the Level-1 triggers use primitive objects, HLT cuts on approximately reconstructed objects, applying thresholds for observables like p_T , relative isolation in the calorimeters and/or tracker, or $|\eta|$ of the particle. Although a primary purpose of the HLTs is to bring the event rate to 100 Hz, these cuts are tuned to be broadly applicable to different analyses, being maximally inclusive to the intended signal while minimizing backgrounds. Each analysis group can then select the data that pass the appropriate high level triggers to make a high precision measurement, exclude a theoretical model, or discover a new as-yet undetected particle.

2.3 Summary

In 2008, after 25 years of construction, the LHC began operation. Within another two years, the combined energy of the beams reached 7 TeV. In 2011, over

¹⁰Primitive objects are coarsely reconstructed particles with reduced resolution.

CHAPTER 2. EXPERIMENTAL SETUP

5 fb^{-1} was collected for 7 TeV. After increasing the energy to 8 TeV in 2012, more than another 20 fb^{-1} was collected. This was sufficient to confirm the existence of a Higgs-like boson, appearing to achieve one of the most elusive discoveries in particle physics. This chapter has reviewed the intricacies of the CMS detector itself, explaining the mechanism used to extract relevant information from the decays of trillions of high energy proton collisions. But how exactly was the new particle found in this mountain of data? How well can we measure its properties? Put bluntly, is this really the Higgs boson we have been looking for?

Chapter 3

Higgs Boson Phenomenology at the LHC

“My drawing was not a picture of a hat. It was a picture of a boa constrictor digesting an elephant. Then, I drew the inside of the boa constrictor, so that the grown-ups could see it clearly. They always need to have things explained.”

“Le Petit Prince”, Antoine de Saint-Exupéry

3.1 How to Find a Higgs Boson at LHC

Just as with any other unstable particle in the Standard Model, when the LHC reaches a sufficient energy, the Higgs boson should be produced and then decay. Prior to discovery, it was known that if a SM Higgs boson existed, its production and decay must obey certain characteristics determined by its mass. By close ex-

amination of the decay products in CMS, we can pull back the curtain to see if a Higgs is hiding in one of these decay channels and if it matches the predictions of the Standard Model.

3.1.1 An Interlude on Feynman Diagrams

Before moving to specifics on how the Higgs is produced and decays at the LHC, we must diverge briefly to discuss production and decay more generally. Up to this point, we have been describing interactions in broad strokes, without delving into explicit mathematics. For the most part, we can continue without evaluating every integral and exponent, but these calculations still impact any analysis so we must find a way to encode these details. Fortunately, such a framework exists to represent the complicated mathematics behind the interactions of the Standard Model: *Feynman Diagrams*. (Fig. 3.1)

In the most naive terms, particle physics measurements can be reduced to one goal: given initial particle states, what is the probability of producing a particular set of final particle states? As previously discussed in Sec. 2.1, the cross section of an event quantifies this probability, but it must be calculated somehow. In quantum field theories, the mathematical operation to convert incoming particle states to outgoing states via allowed operations of the model is the *S-matrix*. Embedded in this matrix is the *scattering matrix element* (commonly shortened to matrix element), \mathcal{M} , which encodes the full details of the interactions of a particular theory.

CHAPTER 3. HIGGS BOSON PHENOMENOLOGY AT THE LHC

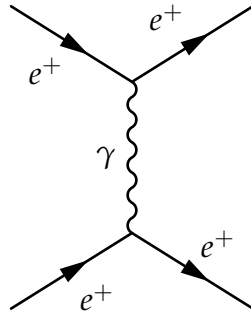


Figure 3.1: Compton Scattering as an example Feynman Diagram. With time going forward from left to right, two electrons approach each other, scatter via exchange of a photon, then move apart.

The heuristic approach used to calculate the matrix element comes from summing the evaluations of all possible fully-connected¹ Feynman diagrams. Finally, the cross section is dependent upon the modulus squared² matrix element which can be evaluated from the Feynman diagrams according to the rules of the interactions in the Lagrangian³.

In practice, finding the matrix element is a two-fold problem. First, one needs to write down every possible contributing diagram. Each diagram must be then evaluated using the Feynman rules of that interaction; quantum electrodynamics

¹To be fully-connected, all incoming and outgoing particles must interact. In the calculation, these diagrams must also be amputated: self-interactions for a single particle do not, by definition, interact with the other particles and thus any diagrams with these elements do not contribute.

²In general, a matrix element can be complex. As with other quantities in quantum mechanics, the modulus squared of an amplitude (e.g. the amplitude multiplied by its complex conjugate) will lead to measurable quantities. This also allows for the possibility of interference between different amplitudes.

³This is a beautiful and very nuanced result where, for the sake of brevity, all of the mathematical rigor has been swept under the rug. A more complete explanation can be found in Part I of Peskin and Schroeder's *An Introduction to Quantum Field Theory*.

CHAPTER 3. HIGGS BOSON PHENOMENOLOGY AT THE LHC

(QED, pertaining to electromagnetism) has one set of rules while quantum chromodynamics (QCD, pertaining to the strong force) has another. Typically, just finding every contributing process this involves an infinite set of diagrams, however it can be simplified by categorizing diagrams by their complexity.

The simplest diagrams, called *tree-level* or *leading order* (LO) diagrams, contain no loops or extra corrections. Consider the diagrams where both the initial and final state is an electron-positron pair. Since diagrams without interactions don't contribute, the only leading order diagrams are found in Fig. 3.2. The strongest rationale for this categorization is implied by the term leading order: tree-level diagrams usually make up the highest order of magnitude term in the calculation and thus can be good approximations of the full result. Diagrams with one-loop or one radiative correction are considered *next-to-leading order* (NLO), two loops are *next-to-next-to-leading order* (NNLO) and so on.

For analyses at the LHC, this framework of Feynman diagrams underlies all levels of theoretical prediction: how a new particle could be produced, determining the most likely methods of decay, or simulating any showering or hadronization. To understand what particles should be observed from a particular process, specialized software called *Monte Carlo generators* (MC) are used to produce the kinematics of expected events. This software is used to generate both background and signal samples by using the Monte Carlo method [29] to populate kinematic distributions as determined from Feynman diagrams. Given the overall complex-

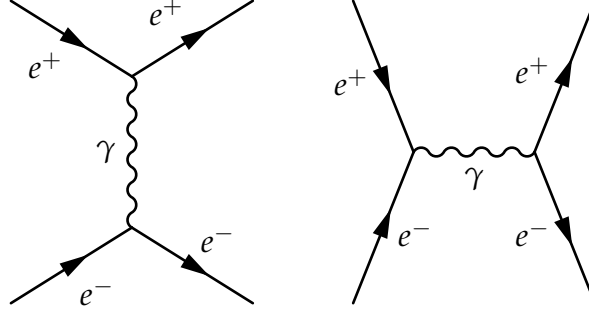


Figure 3.2: Bhabha Scattering: an electron and positron scatter via exchange of a photon (left) and an electron-positron pair annihilate to a photon then pair produce back to an electron-positron pair (right). When looking at the probability of getting an electron-positron pair from an initial electron-positron pair, these are the leading order diagrams.

ity of collisions at CMS, the simulation can be compartmentalized into different generators suited towards certain tasks (e.g. generation and initial decay of the Higgs, showering and hadronization, interactions with the specific detector). Once these samples are finalized, backgrounds can be compared to data and statistically significant deviations can indicate areas of new physics.

3.1.2 Higgs Boson Production

Starting with the production of the Higgs boson at the LHC, a crucial factor comes from use of protons in collisions. As mentioned in Sec. 1.1.1, protons are made up of a veritable sea of quarks and gluons. So when two protons collide, this

CHAPTER 3. HIGGS BOSON PHENOMENOLOGY AT THE LHC

is better thought of as a piece of one proton interacting with a piece of the other. Whether these pieces, called *partons*, are quarks or gluons determine the allowed paths that can be taken to generate a given Feynman diagram. Unfortunately, as we only detect the decay products from an event, the initial state partons can only be determined probabilistically via the *parton distribution function* (PDF). For example, events that use a small fraction of the total energy of the incident proton are much more likely to come from a lower energy gluon than the up or down valence quarks. Due to the theoretical complexity of QCD, these functions are a combination of theoretical predictions and experimental measurements and can become a source of systematics in any analysis. Nevertheless, since the mass of the Higgs boson was predicted to be well below the total energy of the beam, the possible production mechanisms of the Standard Model Higgs boson are well understood.

There are four major production mechanisms for the Higgs boson at the LHC, see Fig. 3.3. Their contribution as a function of the mass of the Higgs boson is seen in Fig. 3.4. *Gluon-gluon fusion* (ggF) is the most likely production mechanism of the Higgs boson (87% near 125 GeV). Even though ggF requires a fermionic loop, gluons are the most likely partons from the colliding protons, so this process dominates. The effective coupling of the Higgs to gluons through this loop is proportional to the mass of the quark in the loop, so the top, being the most massive quark, is the most likely contributor.

After gluon-gluon fusion, the Higgs boson is most likely (7% near 125 GeV) to

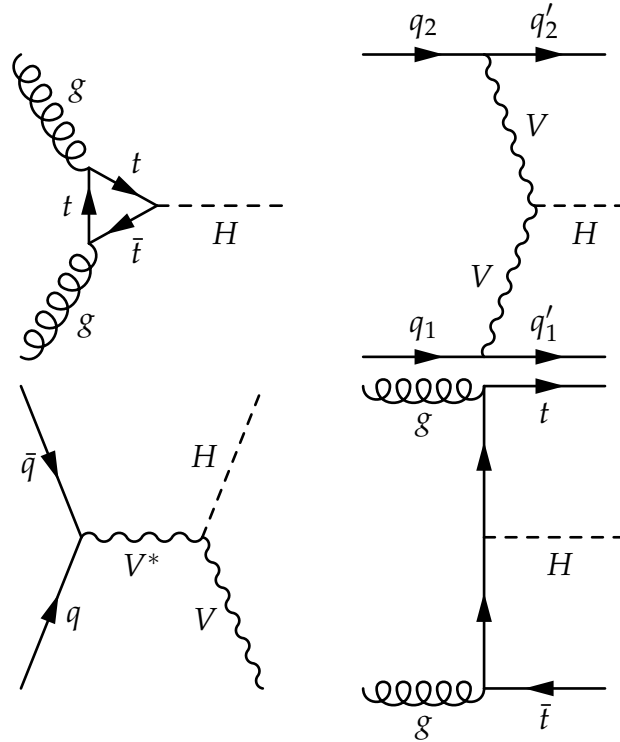


Figure 3.3: Most common production mechanisms for the Higgs boson at the LHC: gluon-gluon fusion (top left), vector boson fusion where $V = W, Z$ (top right), Higgs-strahlung where $V = W, Z$ (bottom left), associated production with $t\bar{t}$ (bottom right).

CHAPTER 3. HIGGS BOSON PHENOMENOLOGY AT THE LHC

be produced through *vector boson fusion* (VBF). A parton from each proton radiates a vector boson (either the W or Z , since photons are massless, they do not directly couple to the Higgs boson) which collide to make the Higgs boson. A crucial feature compared with gluon-gluon fusion is that there are two partons inherent in the production, labeled q_1 and q_2 in Fig. 3.3, which can become detectable jets (q'_1 and q'_2). Due to gluon radiation, ggF can also have jets in the final decay products, but jets from VBF production have substantially different kinematics, aiding in their discrimination in any Higgs boson analysis (see Sec. 3.2.2).

As the Higgs boson mass is restricted to be above either m_W or m_Z , it is energetically unfavorable for a W or Z to decay to the Higgs boson. However, quantum field theories allow for internal lines in Feynman diagrams (propagators) to become virtual and move *off-shell*⁴. Where *on-shell* particles (with a mass near the bare mass, i.e m_W and m_Z for the W and Z respectively) may be directly observed⁵, off-shell particles can never be observed directly⁶. Thus, an off-shell W^* or Z^* can radiate a Higgs to return to an on-shell W (WH) or Z (ZH). This process (3% for WH, 2% for ZH at 125 GeV) is called *Higgs-strahlung* as it is reminiscent of electrons radiating photons in bremsstrahlung. Unsurprisingly, as the Higgs' mass increases, the W or Z must be further off-shell, so this process will contribute less

⁴The shell referred to in on- and off-shell is the mass shell. Classical particles obey the energy-momentum relation $E^2 = p^2c^2 + m_0^2c^4$ where E is the particle's energy, p is its momentum, and m_0 is its bare mass. Virtual particles are not bound by this relation.

⁵With caveats about the stability of the on-shell particle. Some unstable on-shell particles, like the W and Z , decay too rapidly to be observed directly.

⁶In a sense, "virtual particle" is a misnomer as it is closer to a mathematical construct than a particle.

CHAPTER 3. HIGGS BOSON PHENOMENOLOGY AT THE LHC

to the overall cross section.

The last major production mechanism is *associated production with heavy quarks*. Strictly speaking, this can include production of the Higgs with any pair of heavy quarks, but $t\bar{t} + H$ (ttH) is the only one included in the analyses of this thesis. The expected number of ttH events in CMS is quite small and other heavy quark combinations are even smaller.

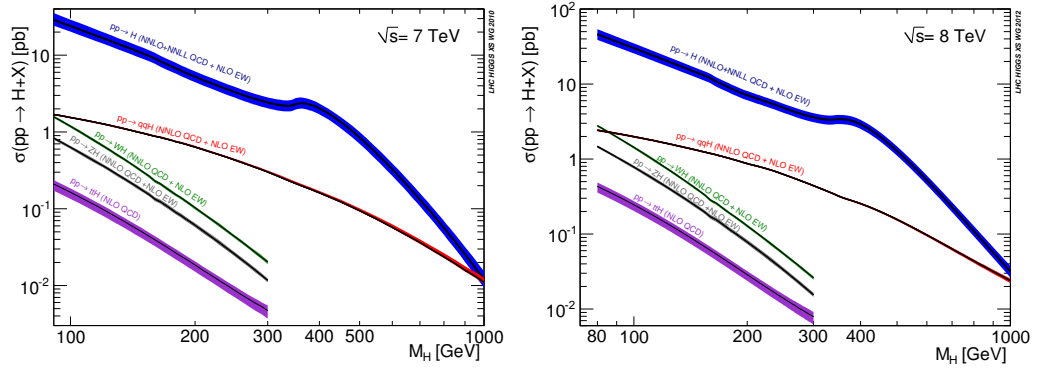


Figure 3.4: SM Cross sections of the different production mechanisms of the Higgs boson as a function of m_H in the LHC for $\sqrt{s} = 7$ TeV (left) and 8 TeV (right) with theoretical uncertainty bands [30]. Gluon-gluon fusion (blue) dominates until $m_H \approx 1$ TeV, where vector boson fusion (red) becomes dominant. WH (green), ZH (grey), and ttH (purple) become energetically unfavorable for higher values of m_H .

3.1.3 Higgs Boson Decay

Once the Higgs boson is produced at LHC, it can decay through any of the allowed channels. Since the SM Higgs boson couples to both fermions and bosons according to their mass, it can decay at leading order to any pair of massive particles and to massless particles at next-to-leading order via one loop. However, what pair is most favorable depends on the mass of the Higgs boson, quantified as the *branching ratio* as seen in the left plot of Fig. 3.5. For $m_H \lesssim 2 \times m_W$, the Higgs boson is most likely to decay to a $b\bar{b}$ pair because the $m_b = 4.2\text{GeV} \ll m_H$ so the b -quarks are the heaviest decay particles that are on-shell. For $2 \times m_t \gtrsim m_H \gtrsim 2 \times m_Z$, $H \rightarrow WW$ and $H \rightarrow ZZ$ can decay to two on-shell bosons, so they become the dominant decays. Lastly, for the highest mass ranges, $m_H \gtrsim 2 \times m_t$, the Higgs boson can also decay to two on-shell top-quarks, so $H \rightarrow t\bar{t}$ becomes much more prevalent. It does not dominate bosonic decay, however, because the fermionic coupling is proportional to the mass of the fermion whereas bosonic coupling is proportional to the square of the mass of the boson.

In CMS, the different analyses of the Higgs boson are grouped by the final state. For $H \rightarrow \gamma\gamma$, $H \rightarrow \tau^+\tau^-$, $H \rightarrow b\bar{b}$ or the direct decays of the Higgs boson are the final state⁷. For $H \rightarrow WW$ or $H \rightarrow ZZ$, how the W or Z decays plays a large role in what backgrounds are applicable, so the analyses are further grouped by the decays of the bosons (e.g. $H \rightarrow W^+W^- \rightarrow (\ell^+\nu)(\ell^-\nu)$ or $H \rightarrow ZZ \rightarrow (\ell^+\ell^-)(q\bar{q})$).

⁷Strictly, b -quarks and τ 's are unstable so the observed particles in these analyses come from their decays.

CHAPTER 3. HIGGS BOSON PHENOMENOLOGY AT THE LHC

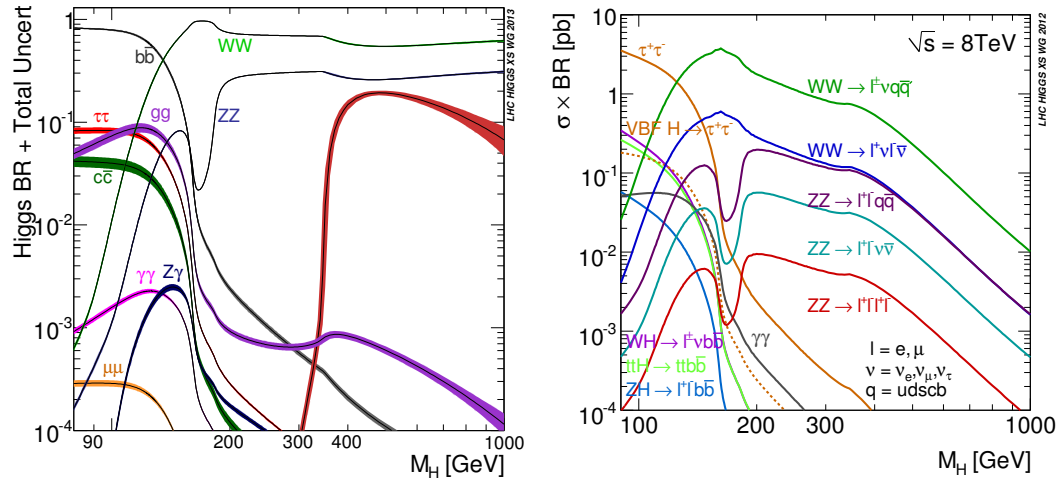


Figure 3.5: SM Branching Ratio of the Higgs boson as a function of m_H through different decays with uncertainty bands (left). SM cross sections times branching ratio at the LHC for $\sqrt{s} = 8$ TeV (right, $H \rightarrow b\bar{b}$ only has associated production shown). [30]

CHAPTER 3. HIGGS BOSON PHENOMENOLOGY AT THE LHC

In any given Higgs boson analysis, there are two competing interests: i) maximize the number of expected Higgs boson events while ii) minimizing the background to increase the overall significance of any signal. The cross sections of the given decay channel as a function of the Higgs boson mass are displayed in the right plot of Fig. 3.5.

For most of the valid mass range, $WW \rightarrow \ell^\pm \nu q \bar{q}$ should have the highest number of expected Higgs boson events. But, any state with quarks in the decay⁸ will need to compete with a large background from QCD processes, plus the momentum resolution for jets is not as good as leptons. Furthermore, any decay with neutrinos involves missing energy, meaning that the full kinematics of the $H \rightarrow ZZ \rightarrow 2\ell 2\nu$ decay cannot be uniquely determined. For this reason, $ZZ \rightarrow 4\ell$ is called the “golden” channel. The full kinematics of the Higgs boson decay can be accounted for and the energy can be measured precisely with comparatively small backgrounds. Although the expected number of Higgs boson events in this channel will be small, the relative purity makes it ideal for discovery and property measurements of a Higgs boson.

⁸Including $H \rightarrow b\bar{b}$.

3.2 Studying the HVV Vertex

Roughly speaking, there are two major vertices in the leading order contributions to Higgs boson production and decay⁹: Higgs boson coupling to two fermions (Hff) or to two bosons (HVV). Of the major production mechanisms from Sec. 3.1.2, ggF and ttH fall into the former category while VBF and VH fall into the latter. For decay, the $H \rightarrow ZZ \rightarrow 4\ell$ channel, which we will use in Secs. 4 and 5, involves an HVV vertex. Understanding how this vertex acts in the Standard Model versus a BSM Higgs boson or background could improve the sensitivity and illuminate what properties of the Higgs boson could be measured.

3.2.1 $H \rightarrow VV$

In the Standard Model, the Higgs boson is a CP-even spin-0 particle. But, as mentioned in Sec. 1.1.2.2, a newly discovered particle could violate CP-symmetry or be spin-2 instead of spin-0: that is, an observed boson may not be the SM Higgs and instead give credence to a BSM theory. For a generic spin-0 resonance X decaying to two spin-1 gauge bosons ($V = Z, W, \text{ or } \gamma$), the scattering amplitude can be written as [31]:

$$\mathcal{A}(X_{J=0} \rightarrow VV) = \frac{1}{v} \left(g_1 m_V^2 \epsilon_1^* \epsilon_2^* + g_2 f_{\mu\nu}^{*(1)} f^{*(2),\mu\nu} + g_4 f_{\mu\nu}^{*(1)} \tilde{f}^{*(2),\mu\nu} \right) \quad (3.1)$$

⁹By the Feynman rules of the Standard Model, there are a total of five vertices with the Higgs boson: one Higgs boson and two fermions, one Higgs boson and two bosons, two Higgs bosons and two bosons, three Higgs bosons, and four Higgs bosons. The latter three are all subdominant, and thus beyond the direct scope of this thesis.

CHAPTER 3. HIGGS BOSON PHENOMENOLOGY AT THE LHC

where v is the vacuum expectation value¹⁰ (VEV) of the SM Higgs field, g_i are the spin-0 couplings with momentum-dependent form factors, m_V is the mass of the vector boson, $f_{\mu\nu}^{(i)} = \epsilon_i^\mu q_i^\nu - \epsilon_i^\nu q_i^\mu$ is the field strength tensor¹¹ where q_i is the momentum and ϵ_i is the polarization vector¹² of the i^{th} gauge boson, while $\tilde{f}^{(i),\mu\nu} = \frac{1}{2}\epsilon_{\mu\nu\rho\sigma}f^{(i),\rho\sigma}$ is the dual field strength tensor.

The SM Higgs boson preserves CP-symmetry, which corresponds to the g_1 and g_2 coupling terms. For $m_V \neq 0$, such as $H \rightarrow ZZ$ or $H \rightarrow WW$, $g_1 = 2i$ at tree-level and is the dominant term while g_2 can contribute via radiative corrections (about 10^{-2}). Clearly, for $m_V = 0$, as in $H \rightarrow \gamma\gamma$ or $H \rightarrow gg$, the first term will not contribute so g_2 is dominant. The g_4 term corresponds to a CP-odd component, where the Higgs boson would be a pseudoscalar if dominant. For the SM Higgs boson, g_4 is extremely small ($O(10^{-10})$) [32] as it only appears at the three-loop level. When the total decay rate is measured independently, as in the case of the $H \rightarrow ZZ \rightarrow 4\ell$ channel, it is more convenient to use the effective fraction of events to a particular coupling defined as

$$f_{gi} = \frac{|g_i|^2 \sigma_i}{|g_1|^2 \sigma_1 + |g_2|^2 \sigma_2 + |g_4|^2 \sigma_4} \quad (3.2)$$

where σ_i is the cross section for the $H \rightarrow VV$ process where $g_i = 1, g_{j \neq i} = 0$. In

¹⁰The vacuum expectation value is the average value of a parameter in the vacuum, which is non-zero for the Higgs boson and is plotted in Fig. 1.2. For the SM Higgs boson, this value is 246 GeV.

¹¹The field strength tensor, $f^{(i)\mu\nu}$, and dual field strength tensor, $\tilde{f}^{*(i)}_{\mu\nu}$, are mathematical representations of the electromagnetic fields in the system.

¹²For vector bosons in Electroweak Theory, polarization vectors indicate the orientation of the spin compared to the four-momenta. For each polarization state, the angular distributions of the decay will be limited due to conservation of angular momentum.

CHAPTER 3. HIGGS BOSON PHENOMENOLOGY AT THE LHC

general, the g_i couplings can be complex and the phase can be found via $\phi_{gi} = \arg(g_i/g_1)$. Additional amplitudes have been calculated for a spin-1 or spin-2 resonance decaying to two gauge bosons in [31].

For the case when a discovered neutral boson appears to be Higgs-like, i.e. $g_1 \gg g_{2,4}$, the amplitude can be rewritten to emphasize measurements of anomalous couplings compared to the SM predictions. Following the formalism used in [31, 33, 34], the amplitude can be rewritten as

$$\mathcal{A}(X_{J=0} \rightarrow VV) = \frac{1}{v} \left(\left[a_1 - e^{i\phi_{\Lambda Q}} \frac{(q_1 + q_2)^2}{(\Lambda_Q)^2} - e^{i\phi_{\Lambda 1}} \frac{(q_1^2 + q_2^2)}{(\Lambda_1)^2} \right] m_V^2 \epsilon_1^* \epsilon_2^* + a_2 f_{\mu\nu}^{*(1)} f^{*(2),\mu\nu} + a_3 f_{\mu\nu}^{*(1)} \tilde{f}^{*(2),\mu\nu} \right) \quad (3.3)$$

where the momentum dependence in the a_1 term is explicitly defined up to a momentum dependent term, $\frac{q^2}{\Lambda^2}$, on the same order as g_2 and g_4 . Λ_1 and Λ_Q are the mass scales where new, not yet observed particles influence the HVV vertex and $\phi_{\Lambda 1}$ and $\phi_{\Lambda Q}$ are the phases of their respective terms. Eqn. (3.2) can then be rewritten as the equations

$$f_{ai} = \frac{|a_i|^2 \sigma_i}{|a_1|^2 \sigma_1 + |a_2|^2 \sigma_2 + |a_4|^2 \sigma_4 + \sigma_{\Lambda_1} / (\Lambda_1)^4} \quad (3.4)$$

$$f_{\Lambda 1} = \frac{\sigma_{\Lambda_1} / (\Lambda_1)^4}{|a_1|^2 \sigma_1 + |a_2|^2 \sigma_2 + |a_4|^2 \sigma_4 + \sigma_{\Lambda_1} / (\Lambda_1)^4} \quad (3.5)$$

$$f_{\Lambda Q} = \frac{\tilde{\sigma}_{\Lambda Q} / (\Lambda_Q)^4}{|a_1|^2 \sigma_1 + \tilde{\sigma}_{\Lambda Q} / (\Lambda_Q)^4} \quad (3.6)$$

with σ_i still corresponding to the respective cross sections for Eqns. (3.4) and (3.5), as it is in Eqn. (3.2). For Eqn. (3.6), since $f_{\Lambda Q}$ can only be measured by compar-

CHAPTER 3. HIGGS BOSON PHENOMENOLOGY AT THE LHC

ing on-shell and off-shell, σ_1 now refers to the total on-shell cross section where $\tilde{\sigma}_{\Lambda Q}/\sigma_1 = m_H^4$.

But how do these coupling ratios manifest in the observation of a resonance? In Eqn. (3.3), there is clear dependence on the polarization vectors of the decay bosons. As detailed in [31], by conservation of angular momentum, the spin of the resonance restricts the allowed polarization vectors and thus the helicity amplitudes which can determine the angular distributions. In other words, for the SM Higgs, the spins of the decay gauge bosons are correlated which will have direct impact on the likely angular distributions of the final decay state. These expected distributions, derived directly from the matrix element, can be used to assign probabilities on an event-by-event basis to discriminate between the SM Higgs and a BSM model or between the SM Higgs and background.

For the generic $ab \rightarrow X \rightarrow VV \rightarrow 4f$ channel, in the rest frame of the resonance (X) nine parameters are sufficient to fully characterize the kinematics: three masses (m_X, m_{V1}, m_{V2}) and six angles. Figure 3.6 shows five of these angles, with a final global rotation about the beam line making the sixth. The five angles in Fig. 3.6, referred to collectively as $\vec{\Omega}$, are all influenced by the helicity distributions from the amplitude listed above. For $m_X > 2 \times m_V$, both of the gauge bosons will be on-shell. But if $m_X < 2 \times m_V$ then the only way this decay can be observed is if at least one of the gauge bosons is off-shell. The global rotation along with the spatial momentum of the resonance are not influenced by the spin-parity of the

CHAPTER 3. HIGGS BOSON PHENOMENOLOGY AT THE LHC

state, so they don't aid in discriminating between different models, although the spatial momentum assists in separation of production mechanisms.

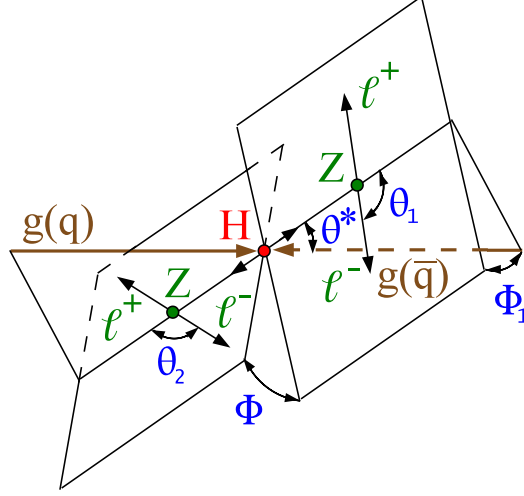


Figure 3.6: Angles in the $H \rightarrow ZZ \rightarrow 4\ell$ decay as defined in the Higgs boson rest frame. Brown lines indicate incoming gluons or quarks along beam line. θ^* defines the angle from beam line to the decay line of the Z bosons. Φ and Φ_1 define the orientation of the planes for each $Z \rightarrow \ell^+\ell^-$ decay relative to the $H \rightarrow ZZ$ decay. θ_1 and θ_2 are the angles of the leptonic decay lines to the $Z_{1,2}$ momenta in the Z's frame.

As stated in Sec. 3.1.3, the $ZZ \rightarrow 4\ell$ final state allows for precise and complete calculation of the decay kinematics, so this matrix element approach is ideal for Higgs boson searches of this final state. To discriminate background or alternative signals from the SM Higgs boson, there are two methods to analyze the three masses and five relevant angles of the decay kinematics on an event-by-event basis.

CHAPTER 3. HIGGS BOSON PHENOMENOLOGY AT THE LHC

A full 8D multidimensional fit could be used [35], but typically a very large number of events are required to properly populate the distributions, making it both computationally expensive and mostly inaccessible to decays with small yields. Alternatively, a single kinematic discriminant could be constructed where the information from the distributions is compounded into unified probabilities. This is the *matrix element likelihood approach* (MELA) [31,33] which is used in CMS $ZZ \rightarrow 4\ell$ analyses.

Discriminants in MELA are built from probabilities, using the equation

$$\mathcal{D} = \frac{\mathcal{P}_{\text{sig}}}{\mathcal{P}_{\text{sig}} + \mathcal{P}_{\text{bkg}}} = \left[1 + \frac{\mathcal{P}_{\text{bkg}}(m_{4\ell}; m_1, m_2, \vec{\Omega})}{\mathcal{P}_{\text{sig}}(m_{4\ell}; m_1, m_2, \vec{\Omega})} \right]^{-1} \quad (3.7)$$

where \mathcal{P}_{bkg} could refer to the probability from the dominant background in the analysis or an alternative signal hypothesis (e.g. a pseudoscalar Higgs boson) and \mathcal{P}_{sig} usually refers to the probability of the SM Higgs boson, though other signals could be used. Each probability ideally stems from an analytic matrix element, as is described in Eqn. 3.3, but when unavailable MC simulation can be used to populate the probability distributions. To account for this, the JHU generator (JHUGEN) was written.

JHUGEN is a dedicated MC generator, which fully encodes the correlations and amplitudes of Eqn. 3.3 as well as analogous amplitudes for spin-1 and spin-2 resonances. For $X \rightarrow VV$ decay, these matrix elements can be used in event generation or directly for building discriminants. Both properties will be utilized in the Higgs discovery (Sec. 4) and properties measurements (Sec. 5). Comparisons

of a few angular distributions from the analytic matrix element and the events from JHUGEN are found in [33].

3.2.2 $V^*V^* \rightarrow H$

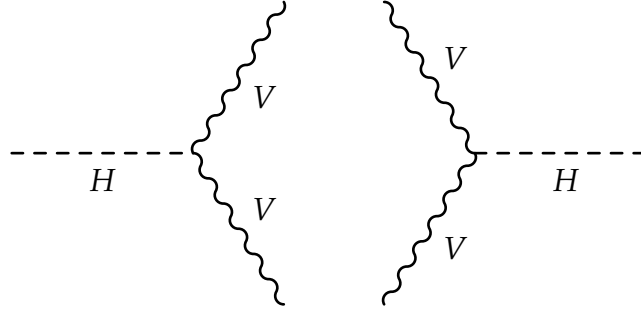


Figure 3.7: On left, the Higgs decays to two gauge bosons. On the right, two gauge bosons produce the Higgs. Any calculation of the amplitude of one vertex will be identical to the calculation of the time reversed vertex.

When looking at the HVV vertex in Fig. 3.7, it becomes obvious that $VV \rightarrow H$ is just a time reversal of the $H \rightarrow VV$ decay. The clear benefit is that, because the diagrams used to form the amplitude in Eqn. 3.1 are identical, the end result is the same. The mathematical description provided by the matrix element approach in Sec. 3.2.1 applies to VBF production as well, with a few key differences:

Production v Decay Kinematics

For VBF, the production kinematics are seen in Fig. 3.8. For $H \rightarrow ZZ \rightarrow 4\ell$ decay, the kinematics of the decay can be fully defined using the three

CHAPTER 3. HIGGS BOSON PHENOMENOLOGY AT THE LHC

masses and five decay angles which can all be fully reconstructed. VBF is considerably more complicated as i) the direction and momentum fraction of the incoming partons are tied to the parton distribution function and ii) the production bosons transfer momentum from these incoming quarks.

Universality of Decay Channel

Although VBF is the subdominant production mechanism, it exists for every decay channel. Thus, measurements of the HVV vertex can be combined across multiple analyses to improve overall performance.

High Mass Sensitivity

As the mass of the Higgs boson increases, VBF production becomes more and more likely. Any searches for high mass resonances should be tuned to emphasize VBF production.

Cross Section Differences

In Eqn. (3.4), there is dependence on the anomalous cross section. Because of the large off-shell mass of V^* in production, the ratio of anomalous cross section to SM cross section is considerably higher than in $H \rightarrow ZZ$ decay, allowing for higher precision with fewer events.

Many BSM models predict multiple Higgs bosons of varying spin states. VBF production is crucial both to unambiguously discover new BSM particles across multiple decay channels and to use the XVV vertex to measure the spin-parity

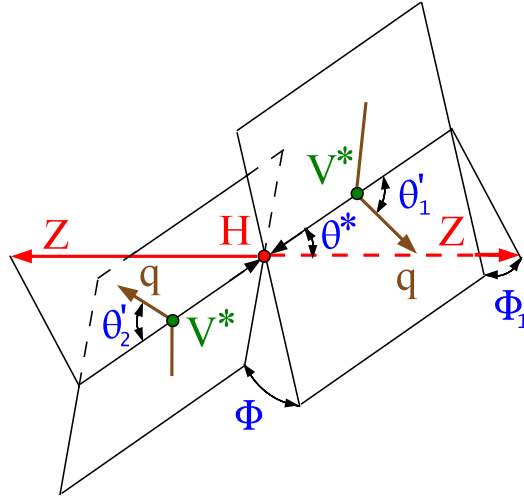


Figure 3.8: Angles of VBF production in $H \rightarrow ZZ$. Compared to Fig. 3.6, the angles mostly have similar definitions, but time reversed. The masses $m_{1,2}$ in decay are analogous to the of the virtual V^* bosons in production while θ'_1 and θ'_2 , as defined in the H frame, are analogous to θ_1 and θ_2 , but the momentum lines for the incoming and outgoing quarks are not collinear.

CHAPTER 3. HIGGS BOSON PHENOMENOLOGY AT THE LHC

state of any discovered resonance. Roughly speaking, although the full kinematics of the production are limited, the two jets that come from VBF production should have a wide forward-backward separation ($\Delta\eta$) and a large invariant mass of the dijet pair (m_{JJ}). Further correlations between these jets and the resonance can both illuminate its spin-parity and aid in the background separation. A numerical computation of the VBF matrix element¹³ is available in JHUGEN, both for generation of events and calculation of probabilities for discriminants.

3.2.3 $V^* \rightarrow VH$

Lastly, the HVV vertex can be studied looking at Higgs-strahlung production (Fig. 3.3, bottom left). As with VBF in Sec. 3.2.2, the mathematics of the generic amplitude in Eqn. 3.1 are identical. In fact, if the final state V boson decays to a jet pair, the decay products are also identical to VBF. However, where VBF expects a pair of strongly separated jets with a large invariant mass, the jet pair in VH production should have an invariant dijet mass, m_{JJ} , close to the on-shell mass of the V boson. Modeling this with a Gaussian distribution¹⁴ about the expected m_V , the remaining kinematics can be used to build a probability. Although VH also depends on the parton distribution function, because the four-momentum of the VH pair can be well constructed and the incoming partons directly produce the

¹³As well as gluon-gluon fusion with two radiated gluons, one of the dominant backgrounds to any VBF study.

¹⁴ m_{JJ} will be close to m_V , but resolution effects in the detector will smear out the true mass distribution.

virtual V^* , an analytic form of the matrix element is constructed and can be used in Higgs boson analyses.

3.3 Summary

Looking through the possible Higgs decay channels, analyzing in the $ZZ \rightarrow 4\ell$ decay channel is clearly a powerful method to search for the Higgs boson. By relying on the precise resolution for leptons in CMS, any $ZZ \rightarrow 4\ell$ event can be fully reconstructed. Then, these detailed kinematics can be used both in the search for the Higgs boson when comparing to backgrounds or in the measurement of its properties. In Sec. 4, we will use the techniques listed above to search for a Higgs boson. Then, in Sec. 5, we will extract what the properties of this new boson are and whether it agrees with Standard Model expectations.

Chapter 4

Higgs Boson Discovery in $ZZ \rightarrow 4\ell$

Vladimir: That passed the time.

Estragon: It would have passed in any case.

Vladimir: Yes, but not so rapidly.

Samuel Beckett, "Waiting for Godot"

4.1 Object Definitions

As specified in Sec. 3.1.3, $H \rightarrow ZZ \rightarrow 4\ell$ should be ideal for Higgs boson discovery. In this channel, we need four good lepton tracks for kinematic decay reconstruction, any relevant radiated photons for proper energy measurements, and a collection of any associated jets to examine the production of any resonance. Although rough reconstructions were defined in Sec. 2.2.3, our objects must be

explicitly defined to examine the certainty of any results. To do so, we need four¹ objects: electrons, muons, photons, and jets.

4.1.1 Electrons

Electrons are geometrically constrained such that $|\eta^e| < 2.5$, with a $p_T^e > 7 \text{ GeV}$ requirement is applied to maintain reasonable reconstruction efficiency while preserving capability to find low mass Higgs candidates. As referenced in Sec. 2.2.3, to reconstruct an electron, usually clusters of energy deposits in the ECAL are used as seeds to match to tracks from the silicon tracker ("outside-in" approach). However, to improve efficiency of low p_T electrons, the opposite approach is also taken where trajectories are used to find clusters in the ECAL ("inside-out"). As electrons pass through the tracker volume, there will be some energy loss via bremsstrahlung which is modeled and fit using a gaussian sum filter. More details on the reconstruction algorithm is found in [36–38]. The expected energy resolution for prompt and isolated (see Sec. 4.1.3) electrons is found in Fig. 4.1.

For identification, a Boosted Decision Tree² (BDT) multivariate technique [39] is trained using observables for electrons, such as the amount of energy radiated via bremsstrahlung during flight, matching between trajectories and ECAL clusters,

¹Although the tau is also a lepton, it decays quickly and tends to appear more like a jet making the mass resolution of a $H \rightarrow ZZ \rightarrow 2\ell 2\tau$ worse than a 4ℓ event. For this reason, taus are not considered in the $H \rightarrow ZZ \rightarrow 4\ell$ analyses in this thesis.

²BDTs form a subset of the broader machine learning technique, decision tree learning, which utilizes multiple decision trees to classify data.

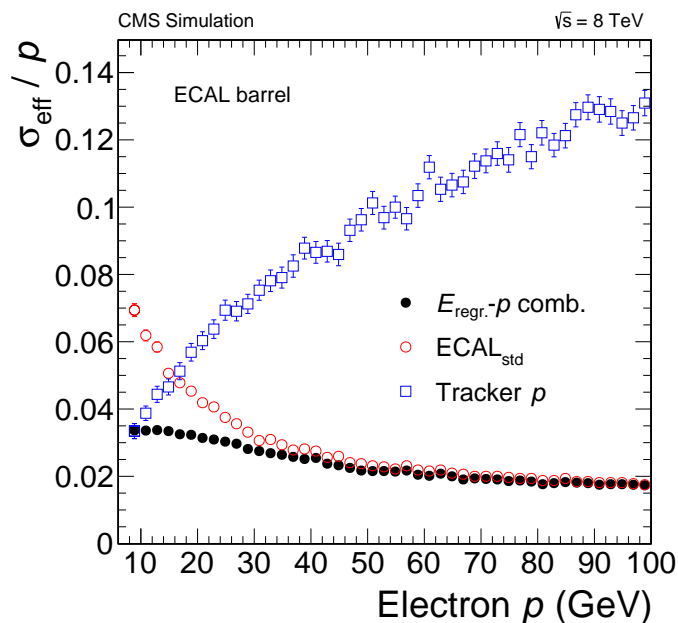


Figure 4.1: Expected energy resolution for prompt and isolated electrons in the ECAL barrel and tracker as a function of the initial energy. The effective resolution is better in the tracker (open blue squares) for low energy electrons, while the ECAL has better resolution for high energy electrons (open red circles). This encourages the use of both outside-in and inside-out techniques. The effective resolution (solid black circles) is $\lesssim 4\%$ of the initial energy.

CHAPTER 4. DISCOVERY

and shower shapes in the ECAL. This method improves the resolution by $\sim 10\%$ per electron compared to cut-based techniques.

Lastly, to validate the momentum scale of the electrons in the 4ℓ channel, invariant mass distributions of data from well-known SM particles that decay to e^+e^- are compared to analytical distributions. In the left plot of Fig. 4.2, electrons with $p_T \gtrsim 35$ GeV show a consistency in the reconstructed mass within $\sim 0.3\%$ across three different decays³ (Z , J/Ψ , Y) for multiple pseudorapidity ranges. A small mass shift appears for lower p_T electrons, accounted for as a systematic uncertainty in the signal mass scale. The effective mass resolution in $Z \rightarrow e^+e^-$, found in the right plot of Fig. 4.2, is below 4% for the full range of the ECAL.

4.1.2 Muons

Muons are reconstructed similar to electrons, except that the matching is done between the inner tracker and the muon system. As with electrons, matching can be “outside-in” starting with hits in the muon system or “inside-out” starting with hits in the tracker. By geometric and efficiency constraints, reconstructed muons must have $|\eta^\mu| < 2.4$ and $p_T^\mu > 5$ GeV [40]. Muons are identified using minimal requirements in the tracker systems to account for consistent trajectories while maintaining small energy deposits in the ECAL [41]. The momentum resolution

³ J/Ψ is a meson made of $c\bar{c}$ with mass $m_{J/\Psi} = 3.1$ GeV while Y is a meson made of $b\bar{b}$ with mass $m_Y = 9.6$ GeV. Along with the Z , they have masses greater than $2m_e$ or $2m_\mu$, so they can be used as references to validate mass reconstruction.

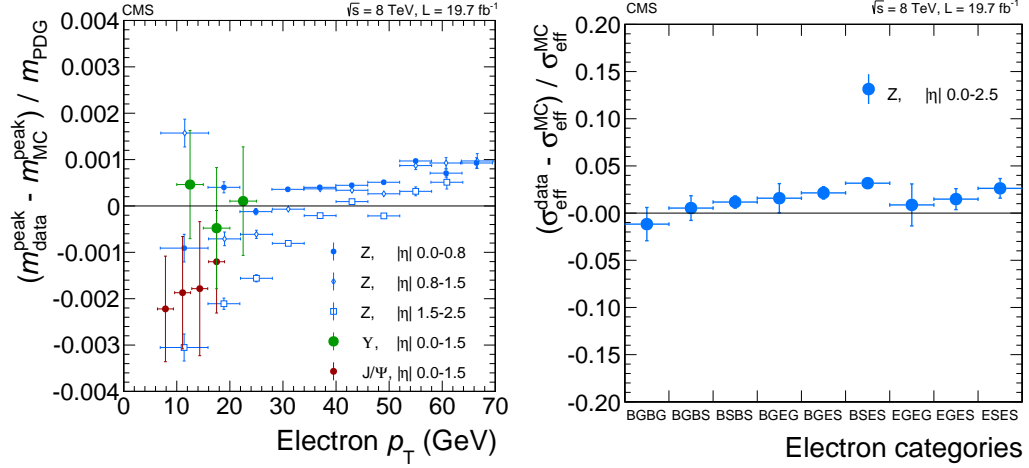


Figure 4.2: Mass bias and resolution between data and MC simulation for di-electron decays at 8 TeV. For bias measurement (left), $Z \rightarrow e^+e^-$ (blue: solid circles in barrel, open diamonds in $0.8 < |\eta| < 1.5$, open squares in endcaps) shows little mass bias for higher p_T electrons. For lower p_T electrons, $Z \rightarrow e^+e^-$, $J/\Psi \rightarrow e^+e^-$ (solid red circles), and $Y \rightarrow e^+e^-$ (solid green circles) show a small bias, accounted for as a systematic uncertainty the signal mass scale. The instrumental mass resolution (right) using $Z \rightarrow e^+e^-$ is less than 4% across the full ECAL range. Electrons are categorized by location and quality of reconstructed electron (B is ECAL Barrel, E for ECAL Endcap. G are the highest quality electron reconstructions, S is for lower quality reconstructions in multiple clusters or with a large amount of bremsstrahlung).

CHAPTER 4. DISCOVERY

for muons is 1.3 – 2.0% in the barrel and up to 6% in the endcaps.

Similar to electrons, the muon mass scale and resolution is found using $Z \rightarrow \mu^+\mu^-$, $J/\Psi \rightarrow \mu^+\mu^-$, and $Y \rightarrow \mu^+\mu^-$ data and MC mass distributions. Across all decays, no bias is seen between data and MC within 0.1%, see left plot in Fig. 4.3. Muons in the endcaps for the J/Ψ decay have slightly larger offsets, but this is a very unlikely kinematic region for $H \rightarrow ZZ \rightarrow 4\ell$ events. In the right plot of Fig. 4.3, mass resolution is seen to be consistent between data and MC within about 5% for the Z di-muon decay.

4.1.3 Lepton Isolation and Photons

After reconstruction and identification, leptons should be isolated to confirm that they are a primary decay product. For any given particle flow candidate, the idea of relative isolation is defined by looking at all particles in a cone around the candidate and finding the relative fraction of p_T from particles coming from non-leptonic processes. This is simply affirming that the lepton is the highest momentum object within a given space of the detector. Explicitly, for a cone of size $\Delta R = \sqrt{(\eta^l - \eta^i)^2 + (\phi^l - \phi^i)^2} < 0.4$, where η^l, ϕ^l are the η and ϕ of the lepton candidate, the isolation R_{iso}^l is

$$R_{iso}^l \equiv \left(\sum p_T^{\text{charged}} + \text{MAX} \left[0, \sum p_T^{\text{neutral}} + \sum p_T^{\text{fl}} - \alpha \times A_{\text{eff}} \right] \right) / p_T^l, \quad (4.1)$$

where $\sum p_T^{\text{charged}}$ is the sum of the transverse momentum of any charged hadrons

CHAPTER 4. DISCOVERY

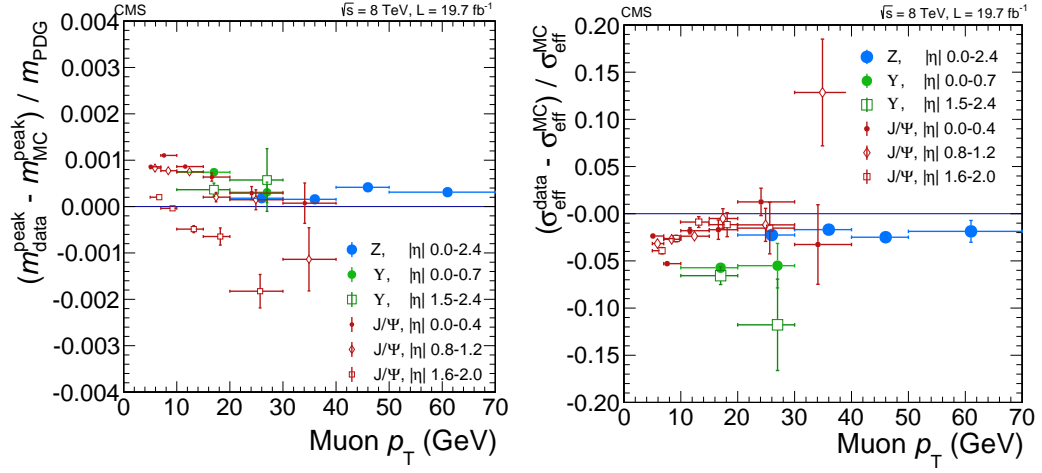


Figure 4.3: Mass bias (left) and resolution (right) between data and MC simulation for di-muon decays: $Z \rightarrow \mu^+ \mu^-$ (blue solid circles), $J/\Psi \rightarrow e^+ e^-$ (red: solid circles in barrel, open diamonds in $0.8 < |\eta| < 1.2$, open squares in endcaps), and $Y \rightarrow e^+ e^-$ (green: solid circles in barrel, open squares in endcaps). Aside from high p_T muonic decays through endcaps, no bias is observed within about 0.1%. Mass resolution between Z decays are in agreement with MC prediction within 5%.

CHAPTER 4. DISCOVERY

coming from the primary vertex, where the primary vertex is the vertex with the highest $\sum p_T^2$ of constituent tracks. $\sum p_T^{neutral}$ and $\sum p_T^\gamma$ are the sums of neutral hadrons and photons that are not radiated by the lepton (see below). When considering particles in this cone, particles very close to the lepton are not considered to avoid double counting.

As stated in Sec. 2.2.3, in any event, there are roughly 20-30 different collisions. After identifying the lepton candidates, the subsystems will still have some occupancy from the remaining collisions, called *pileup*. The maximum and the $\rho \times A_{\text{eff}}$ term in Eqn. 4.1 come from mitigating these effects in the neutral components, as the elements of the subsystems will have an average energy density from unassociated processes [42,43]. All isolated leptons in this analysis must have $R_{iso}^l < 0.4$.

After reconstruction, identification, and isolation, the overall efficiencies of electrons and muons are measured using a “tag and probe” technique [40,44]. Using the large $Z \rightarrow l^+l^-$ dataset, one lepton (either an electron or a muon, depending on what efficiency is being evaluated) that passes all trigger, identification, and selection requirements is used as the “tag”. The $Z \rightarrow l^+l^-$ with background mass shape is then fit using samples where the second lepton, the “probe”, passes or fails the selection requirements. By finding the ratio of efficiencies between data and MC distributions with all associated uncertainties, the simulations can be reweighted in bins of p_T^l and η^l to account for the overall efficiency. Seen in Fig. 4.4, both electrons and muons have high efficiencies for high p_T leptons ($\gtrsim 85\%$ and $\gtrsim 97\%$,

CHAPTER 4. DISCOVERY

respectively).

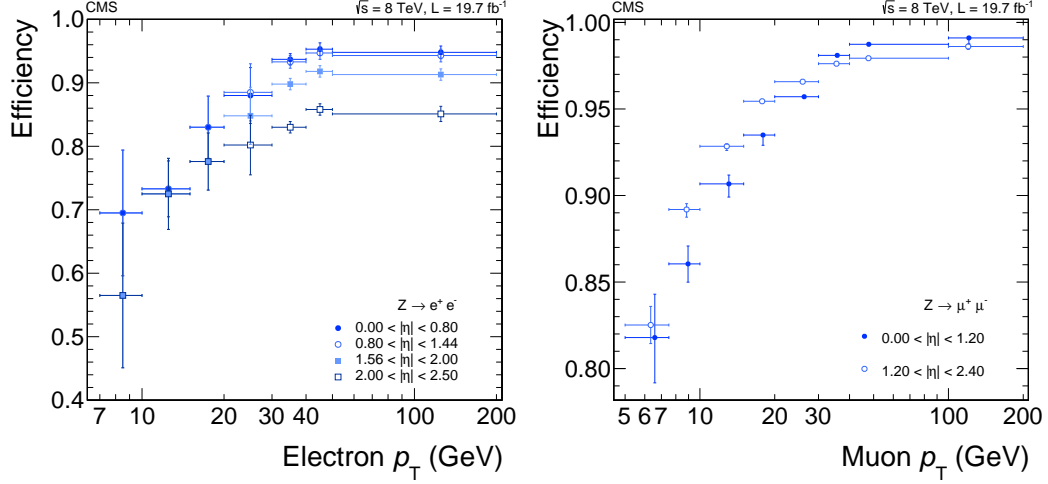


Figure 4.4: Efficiencies of reconstruction and selection for electrons (left: circles in barrel, squares in endcaps) and muons (right: circles in barrel, squares in endcaps) as functions of p_T , found using the tag and probe technique on simulation and data of $Z \rightarrow l^+l^-$.

Although photons are not part of this final decay channel, a lepton that originated from the Z boson decay could radiate a photon in its flight through the detector. To properly reconstruct the full kinematics, these *final state radiation* (FSR) photons must be accounted for. FSR photons, having radiated from a lepton, must be close to a lepton candidate and have sufficient momentum to be considered a significant correction. Photons are accepted as FSR if: i) they fall in similar geometric boundaries as leptons ($|\eta^\gamma| < 2.4$) and ii) have $p_T > 2$ GeV if within $\Delta R < 0.07$ of a lepton OR $p_T > 4$ GeV if found isolated within $0.07 < \Delta R < 0.5$

CHAPTER 4. DISCOVERY

of a lepton candidate. An isolated photon is defined, similar to Eqn. 4.1, as $R_{iso}^\gamma = (\sum p_T^{charged} + \sum p_T^{neutral} + \sum p_T^{photons}) / p_T^\gamma < 1$ where the sums the same except over a cone of $\Delta R < 0.3$.

4.1.4 Jets

Once any lepton and FSR photon candidates are determined, jet candidates are identified. Jets are found using the HCAL and tracker, where they are reconstructed using the anti- k_T clustering algorithm⁴ [45] with distance parameter $R = 0.5$, implemented using the FASTJET package [46]. Jet energy corrections as functions of E_T and η are applied to calibrate the energy of a detected jet with the expected true energy in MC [47]. To separate jet candidates associated with the primary interactions from pileup, a discriminant is built [48] via a multivariate analysis using BDTs where the number vertices, jet shapes, relative multiplicity of charged and neutral components, and fraction of low- p_T components are used for training. The tracks of any selected jets must be compatible with the primary vertex, as true for lepton candidates. Finally, jets must also have sufficiently high momentum ($p_T > 30$ GeV) and separated from any leptons or FSR photons

$$(\Delta R = \sqrt{(\eta^{l/\gamma} - \eta^{jet})^2 + (\phi^{l/\gamma} - \phi^{jet})^2} > 0.5).$$

⁴As stated in Sec. 2.2.2.4, jets come from the hadronization and fragmentation of particles that interact via the strong force. Different clustering algorithms have been developed to group tracks and calorimeter hits inside cones into jet objects.

4.2 MC and Datasets

With reconstructed objects defined, MC samples are generated for both background and signal processes. These samples can establish optimal event selections and quantify uncertainties. The full list of MC Samples can be found in Table 4.1.

For signal samples, gluon-gluon fusion and vector boson fusion are generated at next-to-leading order using POWHEG [49] up to masses of $m_H = 1000$ GeV. Higgs produced via Higgsstrahlung (WH or ZH) or associated production ($t\bar{t}H$) are generated using PYTHIA [50] at LO. Since the expected cross sections for VH and $t\bar{t}H$ are smaller for higher masses (see Fig. 3.4), they are only generated up to $m_H = 200$ GeV.

There are two additional complications for the Higgs boson signal samples. First, for lower masses, the Higgs boson can be modeled to have approximately zero-width, that is the mass distribution in $m_{4\ell}$ will be a very narrow resonance compared to experimental resolution. For a higher mass Higgs boson, more decay modes become energetically viable, so this approximation breaks down⁵ around $m_H \approx 200$ GeV, as seen in Fig. 4.5. To account for this, the mass distribution uses the complex-pole scheme [51–53]. Second, gluon-fusion Higgs boson production with 4ℓ decay has identical initial and final states as the $gg \rightarrow 4\ell$ background, so they will interfere (see Sec. 3.1.1, diagrams with identical initial and final states can

⁵This approximation also is not entirely valid for a lower mass Higgs boson, as we shall see in Sec. 5.4.

CHAPTER 4. DISCOVERY

Process	MC generator	$\sigma_{(N)NLO}$		Comments and sample name
		7 TeV	8 TeV	
Higgs boson $H \rightarrow ZZ \rightarrow 4\ell$				
$gg \rightarrow H$	POWHEG	[1-20] fb	[1.2-25] fb	$m_H = 110\text{-}1000$ GeV
$VV \rightarrow H$	POWHEG	[0.2-2] fb	[0.3-25] fb	$m_H = 110\text{-}1000$ GeV
$V^* \rightarrow VH$	PYTHIA	[] fb	[] fb	$m_H = 110\text{-}200$ GeV
$t\bar{t}H$	PYTHIA	[] fb	[] fb	$m_H = 110\text{-}200$ GeV
ZZ continuum				
$q\bar{q} \rightarrow ZZ \rightarrow 4e(4\mu, 4\tau)$	POWHEG	66.09 fb	76.91 fb	ZZTo4e(4mu,4tau)
$q\bar{q} \rightarrow ZZ \rightarrow 2e2\mu$	POWHEG	152 fb	176.7 fb	ZZTo2e2mu
$q\bar{q} \rightarrow ZZ \rightarrow 2e(2\mu)2\tau$	POWHEG	152 fb	176.7 fb	ZZTo2e(2mu)2tau
$gg \rightarrow ZZ \rightarrow 2\ell 2\ell'$	gg2ZZ	3.48 fb	12.03 fb	GluGluToZZTo2L2L
$gg \rightarrow ZZ \rightarrow 4\ell$	gg2ZZ	1.74 fb	4.8 fb	GluGluToZZTo4L
Other di-bosons				
$WW \rightarrow 2\ell 2\nu$	Madgraph	4.88 pb	5.995 pb	WWJetsTo2L2Nu
$WZ \rightarrow 3\ell\nu$	Madgraph	0.868 pb	1.057 pb	WZJetsTo3LNu
$t\bar{t}$ and single t				
$t\bar{t} \rightarrow \ell^+\ell^-\nu\bar{\nu}b\bar{b}$	POWHEG	17.32 pb	23.64 pb	TTTo2L2Nu2B
t (s-channel)	POWHEG	3.19 pb	3.89 pb	T_TuneXX_s-channel
\bar{t} (s-channel)	POWHEG	1.44 pb	1.76 pb	Tbar_TuneXX_s-channel
t (t-channel)	POWHEG	41.92 pb	55.53 pb	T_TuneXX_t-channel
\bar{t} (t-channel)	POWHEG	22.65 pb	30.00 pb	Tbar_TuneXX_t-channel
t (tW-channel)	POWHEG	7.87 pb	11.77 pb	T_TuneXX_tW-channel-DR
\bar{t} (tW-channel)	POWHEG	7.87 pb	11.77 pb	Tbar_TuneXX_tW-channel-DR
Z/W + jets ($q = d, u, s, c, b$)				
W + jets	MadGraph	31314 pb	36257.2 pb	WJetsToLNu
Z + jets, $m_{\ell\ell} > 50$	MadGraph	3048 pb	3503.7 pb	DYJetsToLL*M-50
Z + jets, $10 < m_{\ell\ell} < 50$	MadGraph	12782.63 pb	915 pb	DYJetsToLL*M-10To50

Table 4.1: Full List of MC Samples generated for analysis of $H \rightarrow ZZ \rightarrow 4\ell$, with their respective processes, generators, cross-sections for 7 & 8 TeV, and sample names.

CHAPTER 4. DISCOVERY

interfere). Below $2 \times m_Z$, this effect is negligible, because the Higgs boson width is expected to be narrow, but it must be accounted for in high mass Higgs boson samples. Additionally, signal events are reweighted to the total $pp \rightarrow H$ cross section, including NNLO and next-to-next-to-leading \log^6 corrections for gluon fusion [54–66] and NNLO contributions for VBF [58,67–71].

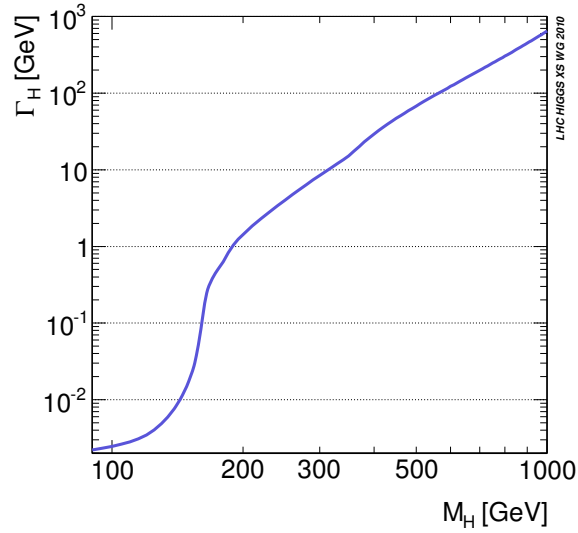


Figure 4.5: Higgs boson width as a function of m_H . The width of the mass shape for the Higgs depends on the available decay modes at a given mass. For $m_H > 2 \times m_Z$, both bosons in bosonic decays will be on-shell (see Sec 3.1.3), drastically increasing the width compared to low m_H .

We can categorize background into *reducible* and *irreducible* backgrounds. Reducible backgrounds come from large cross section SM processes where two prompt isolated leptons are generated and the remaining two, coming from secondary

⁶Corrections from additional Feynman diagrams can also have logarithmic dependencies.

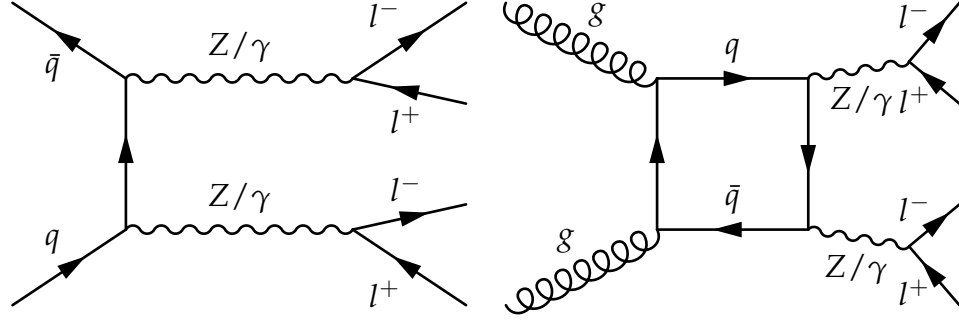


Figure 4.6: Feynman diagrams for the irreducible backgrounds in the 4ℓ channel. $q\bar{q} \rightarrow 4\ell$ (left) is dominant, while $gg \rightarrow 4\ell$ (right) requires a loop and is subdominant.

decays unrelated to the desired $ZZ \rightarrow 4\ell$ vertex, are misidentified leptons. Z + jets, for example, can have two isolated leptons from the Z but occasionally two b -jets will be produced which can be misidentified as leptons. Similarly, $t\bar{t}$ commonly decays to a state with $l^+l^-b\bar{b}$. W/Z + jets samples are produced using MADGRAPH [72], while any t samples are made using POWHEG. As the name implies, a smart selection (see Sec. 4.3) can reduce this background substantially.

Irreducible backgrounds are SM processes that have identical decay channels as the intended Higgs signal events, arising from the ZZ continuum background. The primary irreducible background is $q\bar{q} \rightarrow 4\ell$, as seen in the left diagram of Fig. 4.6, generated at NLO using POWHEG. $gg \rightarrow 4\ell$, in the right diagram of Fig. 4.6, is the subdominant irreducible background as it requires one loop to be produced. It was generated using GG2ZZ [73].

CHAPTER 4. DISCOVERY

All generated background and signal samples interface with `PYTHIA` to produce hadronization and low- p_T radiation effects. After this stage, every sample was processed through software built on `GEANT4` [74,75] which simulates the passage of particles through the matter of CMS subdetectors, then reconstructs objects using the same algorithms applied on data, accounting for any pileup effects. For any LO generators, the PDF used for generation is `CTEQ6L` [76]. For NLO generators, `CT10` [77] is used.

The datasets used are from the 2011 7 TeV and 2012 8 TeV runs, with luminosities of $5.1fb^{-1}$ and $19.7fb^{-1}$, respectively. Triggers that require at least a pair of leptons are used. For any double lepton trigger (di-electron, di-muon, or muon and electron), at least one lepton must have $p_T > 17$ GeV and the other must have $p_T > 8$ GeV. A triple electron trigger is also used where the *leading* (highest p_T) electron must have $p_T > 15$ GeV, the *subleading* (second highest p_T) electron must have $p_T > 8$ GeV, and the third electron must have $p_T > 5$ GeV.

4.3 Event Selection

After finding four prompt isolated leptons, most of the reducible background is already suppressed, but because the cross sections of the reducible processes are so large they should be minimized. For the $ZZ \rightarrow 4\ell$ decay, the Z decays are prompt so all four leptons should appear to come from one common vertex.

CHAPTER 4. DISCOVERY

Upon reconstruction of a primary vertex, the three dimensional distance of closest approach for a trajectory is called the *impact parameter*, which has an associated uncertainty of σ_{IP} . To confirm a common vertex, a requirement of $|\text{SIP}_{3\text{D}} = \frac{\text{IP}}{\cos\theta_{\text{IP}}}| < 4$ is applied. Leptons that fail either the $|\text{SIP}_{3\text{D}}| < 4$ requirement or the earlier $R_{\text{iso}}^l < 0.4$ requirement are considered *loose* leptons⁷, to be used in the estimate of the reducible backgrounds (see Sec. 4.4.1). On top of the p_T cuts from any triggers, the leading lepton must have $p_T > 20$ GeV and the subleading lepton must have $p_T > 10$ GeV to improve efficiency.

Next, we construct Z candidates out of the available leptons. The pair of opposite charge and matching flavor leptons (e.g. e^+e^- and $\mu^+\mu^-$) with an invariant mass closest to m_Z is considered Z_1 , such that $40 < m_{Z1} < 120$ GeV. This requirement eliminates nearly all backgrounds that do not contain a leptonic Z decay (e.g. $t\bar{t}$, $W + \text{jets}$) as it is unlikely to get an invariant mass near m_Z otherwise.

Out of the remaining isolated leptons, another pair of opposite charge matching flavor leptons form Z_2 . For a lower mass Higgs, it's expected that one Z would be on-shell while the other would be off-shell. To optimize for these low mass signals⁸, m_{Z2} has a looser mass requirement such that $12 < m_{Z2} < 120$ GeV. If there are multiple Z_2 candidates, as can be the case for five or more isolated leptons, the Z_2 candidate with the highest scalar sum of p_T is chosen as these leptons should

⁷Loose leptons also have relaxed constraints on electron or muon identification but must be separated by at least $\Delta R > 0.02$.

⁸For Higgs boson events with $m_H > 2m_Z$, both of the Z candidates should be on-shell which is accounted for by restricting $m_{Z1,2} < 120$ GeV.

CHAPTER 4. DISCOVERY

have the highest reconstruction efficiency. For both Z_1 and Z_2 , if there are any FSR photons associated with one of the constituent leptons, only those that bring $m_{Z_{1,2}}$ closer to m_Z are kept so long as $m_{ll\gamma} < 100$ GeV.

The requirement for Z_2 eliminates most of the remaining reducible $Z + X$ background for the same reason that the Z_1 requirement eliminates other leptonic background. However, to avoid possible contamination from low-mass hadronic decays faking leptons, any opposite charge pairing of the selected four leptons must have a sufficient invariant mass such that $m_{ll'} > 4$ GeV.

Finally, given the earlier direct exclusions from LEP (see Sec. 1.1.2.1), a requirement of $m_\ell > 100$ GeV is applied. After object definitions and selection requirements, the final efficiencies of signal detection as a function of the Higgs boson mass are seen in Fig. 4.7. In general, the 4μ mode has the highest efficiency due to the quality of reconstruction compared to electrons. The relative increase in efficiency past $m_H \approx 200$ GeV comes from both Z candidates being on-shell. Polynomial parameterizations are built for the MC signal mass points such that a full range of masses can be examined, as used in Sec. 4.4.

4.4 Likelihood Analysis

All observed events are split into twelve different sub-categories: two for beam energy (7 or 8 TeV), three for final states ($4e$, 4μ , or $2e2\mu$), and two for jet categoriza-

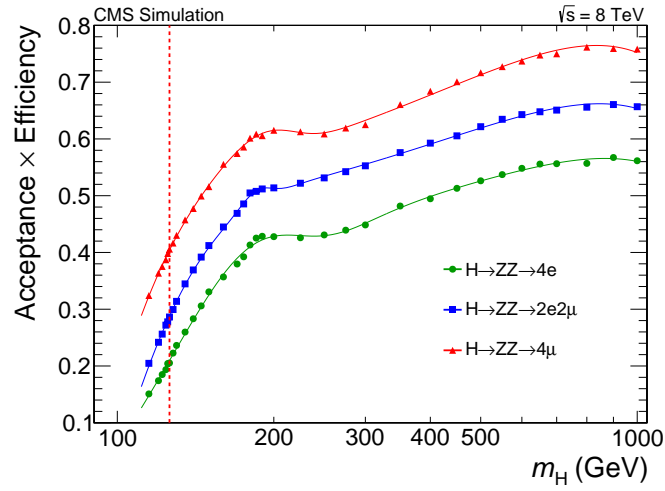


Figure 4.7: Signal detection efficiencies of ggF as functions of m_H , fit with polynomial curves estimated from MC simulation. 4μ (red triangles) has the highest relative efficiency as muon have better selection efficiency, while $4e$ (green circles) has the lowest from electrons having worse efficiency. $2e2\mu$ (blue squares) is between the two. Efficiencies are produced for all production methods with similar results.

CHAPTER 4. DISCOVERY

tion (≥ 2 jets or < 2 jets). The likelihood analysis is built on a three-dimensional model of observables: $m_{4\ell}$, $\mathcal{D}_{\text{bkg}}^{\text{kin}}$ and p_T or \mathcal{D}_{jet} , where the final observable is determined by the jet category. Instead of applying a full three-dimensional fit, the model is broken into three pieces which account for correlations. A probability distribution is defined for $m_{4\ell}$, while two-dimensional templates are defined for $(m_{4\ell}, \mathcal{D}_{\text{bkg}}^{\text{kin}})$ and $(m_{4\ell}, p_T \text{ or } \mathcal{D}_{\text{jet}})$ where the respective templates are normalized for each slice of $m_{4\ell}$. The three-dimensional likelihood is therefore the product of the likelihood of a given mass and the likelihoods of a particular value of $\mathcal{D}_{\text{bkg}}^{\text{kin}}$ and p_T or \mathcal{D}_{jet} given that mass. Explicitly, for each event:

$$\mathcal{L}_{3D}(m_{4\ell}, \mathcal{D}_{\text{bkg}}^{\text{kin}}, p_T \text{ or } \mathcal{D}_{\text{jet}}) = \mathcal{L}(m_{4\ell}) \times \mathcal{L}(\mathcal{D}_{\text{bkg}}^{\text{kin}} | m_{4\ell}) \times \mathcal{L}(p_T \text{ or } \mathcal{D}_{\text{jet}} | m_{4\ell}) \quad (4.2)$$

where the first term defines the likelihood of the event having that $m_{4\ell}$, the second term defines the 2D template for the kinematic discriminant given $m_{4\ell}$, and the third term defines the 2D template for the production discriminant, either p_T or \mathcal{D}_{jet} , given $m_{4\ell}$. Each likelihood is detailed more explicitly in the following sections, where shape systematics are discussed for each component and common normalization systematics are detailed in Sec. 4.4.4.

4.4.1 Expected $m_{4\ell}$ Distributions

To first order, any Higgs-like resonance should appear as an excess of events compared to what is expected from the SM background processes. To test different

CHAPTER 4. DISCOVERY

Higgs boson masses, the backgrounds must be well-defined across a wide range of $m_{4\ell}$. For the dominant ZZ continuum backgrounds, the MC distributions are used as a baseline for the $m_{4\ell}$ shape. The cross sections of the ZZ backgrounds are calculated to NLO using MCFM [78–80]. These distributions are then fit with an analytic function to allow for a smooth distribution over the full range, where their normalizations are allowed to vary within uncertainties. Shape uncertainties are comparatively negligible.

For the reducible background, hereafter called $Z + X$, because most of the events are eliminated by demanding four prompt leptons with two Z objects, a data driven mass shape is used to account for all contributions. One can use a data driven technique by looking in a region of phase space adjacent to the signal region, typically called a *control region*, to extrapolate back to the signal region. In the case of this analysis, using a dataset with $Z_1 + l_{\text{loose}}$, construct Z_2 using same flavor lepton pairs where $m_{Z_2} > 12 \text{ GeV}$ and $m_{4\ell} > 100 \text{ GeV}$. Two parallel methods are taken to estimate the reducible contribution with this sample, either the lepton pair that makes up Z_2 will have the same sign (SS) while passing all selection requirements or they are opposite sign (OS) but fail the selection requirements while passing the loose requirements.

In the OS analysis, the mass of Z_2 is further constrained such that $|m_{Z_2} - m_Z| < 10 \text{ GeV}$. The dataset is then further split into two categories: after the two prompt leptons from Z_1 there are either no leptons passing the selection requirements

CHAPTER 4. DISCOVERY

(2P2F) or one lepton passing the selection requirements (3P1F). Unsurprisingly, the two categories largely correspond to the types of reducible background. $Z + \text{jets}$ and $t\bar{t}$ will tend to have two prompt leptons, while $WZ + \text{jets}$ will tend to have three with any other selection leptons coming from misidentified jets. To estimate the contribution from each category to the signal region, each event is reweighted by a factor that accounts for the misidentification of one or two leptons. In the SS analysis, Z_2 is not as constrained with $|m_{Z2} - m_Z| < 40 \text{ GeV}$. The extrapolation back to the signal region is then similar to 2P2F in the OS method, with an additional factor to account for the ratio of OS to SS control regions.

Both methods give similar expectations for the number of reducible background events in the signal region, with any uncertainties accounted for the final results. For the mass shape, the 2P2F and 3P1F events from the OS method are fit using analytical forms and combined to get the shape in Fig. 4.8. This shape has an associated uncertainty coming from the choice of fit function and binning, seen as a yellow band.

For signals, the nominal mass distributions for the expected masses are found via MC simulation. For each Higgs boson mass simulated, the mass distribution is fit with a relativistic Breit-Wigner distribution⁹ convoluted with a double-sided Crystal Ball function¹⁰ [81]. For $m_H < 400 \text{ GeV}$, this function is fit for all pro-

⁹The Breit-Wigner distribution is commonly used in particle physics, representing the probability of generating an unstable propagator, like the Z or Higgs, at a given energy.

¹⁰The Crystal Ball is a function that is used to give a Gaussian distribution a long-tail with power-law behavior. A double-sided Crystal Ball applies this long tail on both sides of the Gaussian. In particle physics, this is useful to account for energy leakage in the tails of probability distributions.

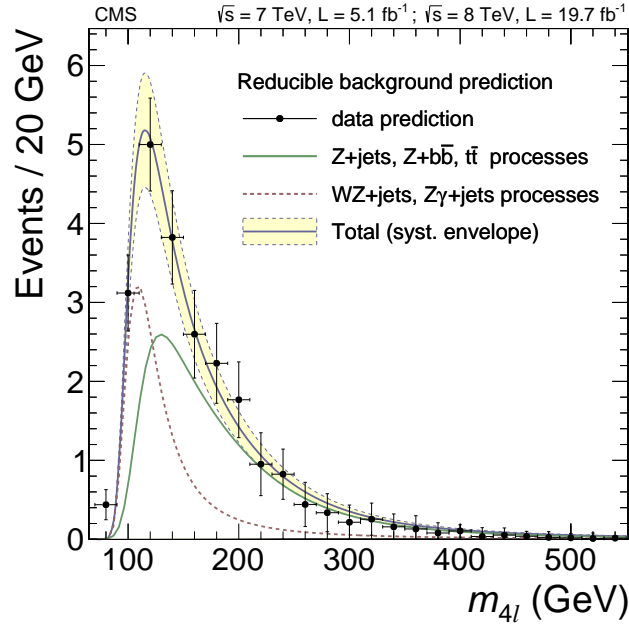


Figure 4.8: Distributions of $m_{4\ell}$ for reducible background. Contributions from $Z + \text{jets}$, $Z + b\bar{b}$, and $t\bar{t}$ come from 2P2F category (solid green) of OS control region. WZ and $Z\gamma + \text{jets}$ come from 3P1F category (dashed red). Each contribution is fit separately to form full prediction (blue curve with yellow band indicating total uncertainty) compared to data (black dots).

CHAPTER 4. DISCOVERY

duction mechanisms, jet categories, decay modes, and beam energy, where the normalization will vary by the expected cross section for that production or categorization. These normalizations have associated systematics (see Sec. 4.4.4), while any shape uncertainties are minimal since the experimental mass resolution of the detector being much larger than the expected widths. Sample distributions for the signal are found in Fig. 4.9.

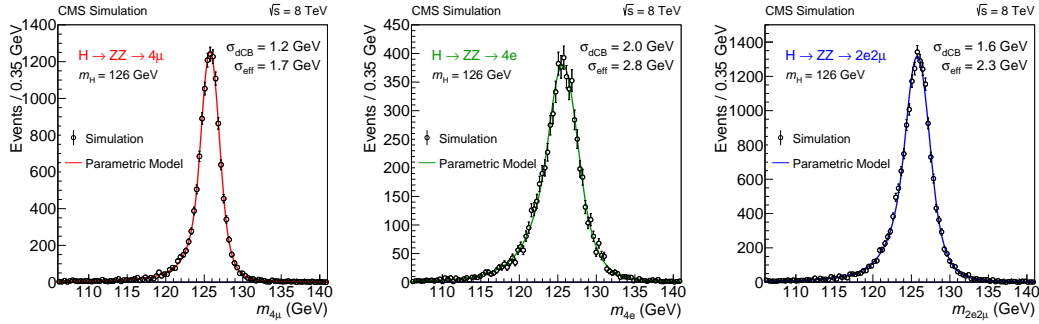


Figure 4.9: Sample Higgs signal $m_{4\ell}$ fits on MC simulation for $m_H = 126$ GeV in ggF for 4μ (left, red), $4e$ (middle, green), and $2e2\mu$ (right, blue) Each production method, beam energy, decay mode, and jet categorization has an independent fit for every mass point.

In the high mass region, $m_H \gtrsim 400$ GeV, more effects are taken into account. As specified in Sec. 4.2, the complex-pole scheme must be used and interference with the background is non-negligible, both of which enter into the signal $m_{4\ell}$ parameterizations via reweighting. After this reweighting, the Breit-Wigner constraint used for the lower masses is loosened by allowing the width to float such that it

CHAPTER 4. DISCOVERY

matches the MC distributions. Finally, instead of using the same mass shape for ggF and VBF, the shapes are found independently. The high mass $m_{4\ell}$ distributions have shape systematics arising from theoretical uncertainties in the applied corrections on top of any normalization systematics. Example high mass signal distributions with uncertainty bands are contained in Fig. 4.10.

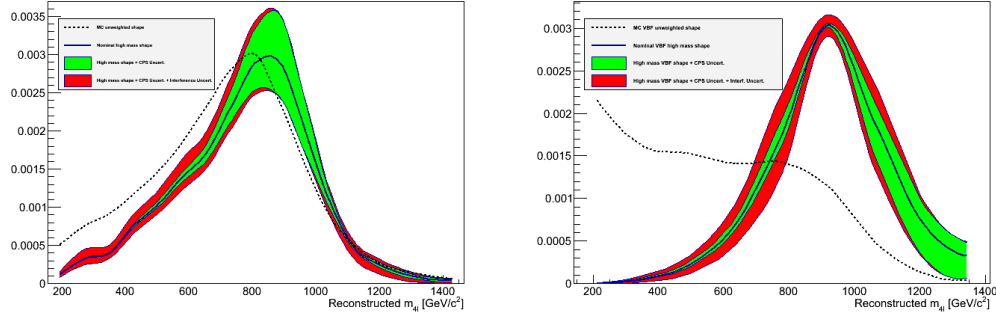


Figure 4.10: Higgs signal $m_{4\ell}$ shapes for 900 GeV for ggF (left) and VBF (right). Dashed black line is distribution directly from MC. Blue solid line accounts for complex-pole scheme reweighting and interference with backgrounds, where the red and green envelopes account for the uncertainty of reweighting.

These mass shapes can then be multiplied by the signal efficiencies, as discussed in Sec. 4.3, and the ratio for jet categorization, to be discussed in Sec. 4.4.3. This process gives the final expected yields for both the SM backgrounds and the Higgs boson signal as functions of $m_{4\ell}$ for any given Higgs boson mass to be evaluated.

4.4.2 Kinematic Discriminant for Decay

For any 4ℓ event, the kinematic discriminant, $\mathcal{D}_{\text{bkg}}^{\text{kin}}$, can be constructed with the angular distributions of the decay. Eqn. 3.7 defines the discriminant used, where the signal probability comes from the leading order JHUGen matrix element and the background probability comes from the $q\bar{q} \rightarrow 4\ell$ LO matrix element found via MCFM. Multiple sources for the matrix elements were tested with negligible differences. The relative normalization of the probabilities is tuned using a constant factor such that the total probability of signal plus background are equal above and below $\mathcal{D}_{\text{bkg}}^{\text{kin}} = 0.5$. No matrix element parameterization exists for $Z + X$, but the kinematic largely match those for $q\bar{q} \rightarrow 4\ell$ where a shape systematic is applied to account for any differences. Alternative methods using machine learning techniques, such as boosted decision trees or bayesian neural networks, show similar performance to the matrix element approach. Two dimensional templates of $(m_{4\ell}, \mathcal{D}_{\text{bkg}}^{\text{kin}})$ can be seen in Fig. 4.11.

4.4.3 Discriminating Production Mechanisms

As discussed in Sec. 3.2.2, VBF events can be identified using the kinematics of the additional two jets over other production mechanisms or backgrounds. In that vein, after selection, events are categorized by their number of jets. The *di-jet* category encapsulates all events with at least two jets meeting the definitions in

CHAPTER 4. DISCOVERY

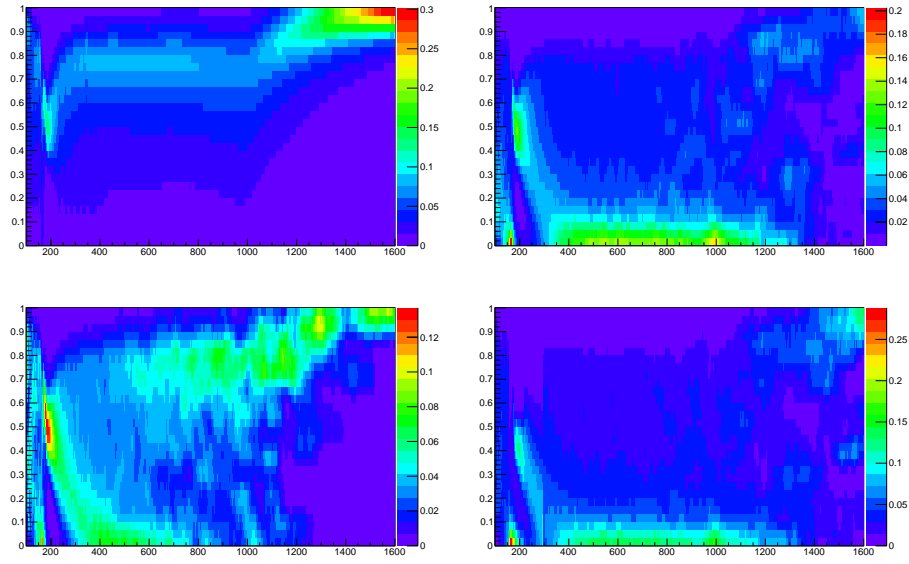


Figure 4.11: Samples of $\mathcal{D}_{\text{bkg}}^{\text{kin}} \vee m_{4\ell}$ templates for 8 TeV $2e2\mu$ Higgs boson signal (top left), $q\bar{q} \rightarrow ZZ$ (top right), $gg \rightarrow ZZ$ (bottom left), and $Z + X$ (bottom right) used in the analysis. Separate templates were made for $4e$, 4μ , and $2e2\mu$.

CHAPTER 4. DISCOVERY

Sec. 4.1.4. All other selected events fall into the *non-dijet* category. On top of the signal selection efficiency, the dijet ratio is constructed as a function of m_H (Figs. 4.12 and 4.13) to determine the number of expected signal and background events in a particular category and thus enters into the $m_{4\ell}$ distributions for each jet category.

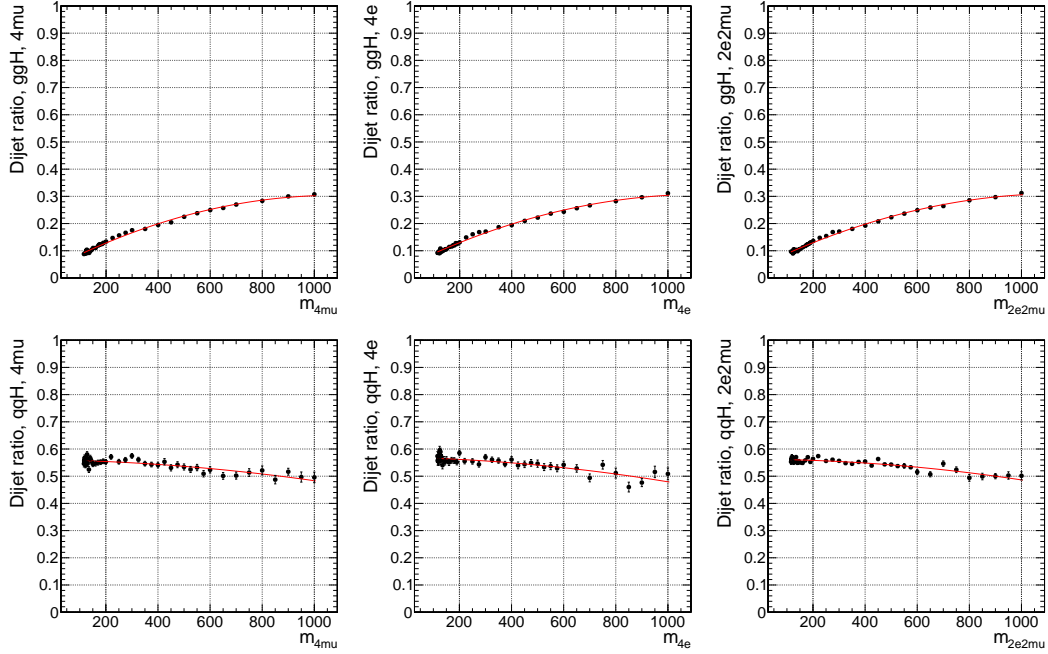


Figure 4.12: Dijet ratio of ggF (top row) and VBF (bottom row) as functions of m_H . Left to right: 4μ , $4e$, $2e2\mu$. There should be very little correlation between the Higgs final state and the dijet ratio, which is exactly what is seen.

Whether an event falls into the dijet or non-dijet category determines what observables are used for the analysis. In the non-dijet category, Higgs boson events, particularly those generated via other production mechanisms than ggF, will tend to have higher p_T distributions, seen in Fig. 4.14. To aid in discrimination of pro-

CHAPTER 4. DISCOVERY

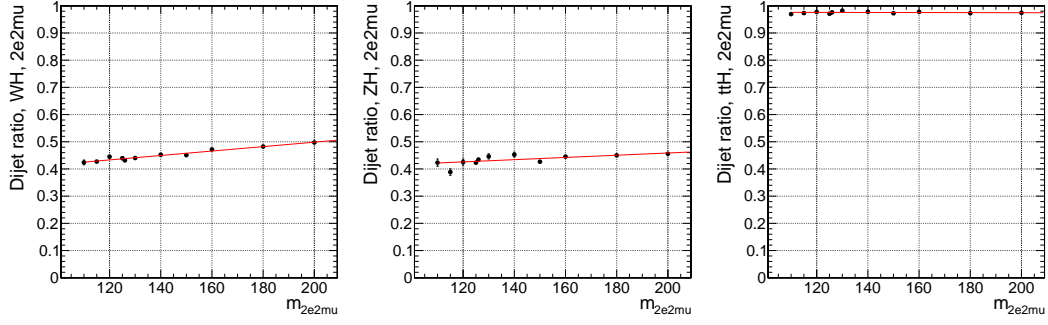


Figure 4.13: Dijet ratio of WH (left), ZH (middle), and ttH (right). ttH inherently involves the production of two jets, so the ratio will be nearly 100%.

duction mechanisms, p_T can be used as an observable in the non-dijet category.

For signal, p_T distributions are found via analytic fits of MC simulation, with some reweighting for ggF high mass samples to account for theoretical limitations and to bring the LO p_T distributions of associated Higgs production in agreement with NLO simulation. Shape systematics come from the choice of scales used theoretical predictions, top-mass approximation, and PDF uncertainties for ggF and VBF, while associated production methods have systematics from the reweighting procedure applied. For the irreducible ZZ backgrounds, analytical fits come from MC, where shape systematics are identical to VBF with an additional shape systematic to account for differences between data and MC [82]. $Z + X$, being data driven, is fit with a modified Tsallis function [83] where systematics come from uncertainty of the fit. Due to small differences in resolution based on p_T , there is a slight dependence of $\mathcal{D}_{\text{bkg}}^{\text{kin}}$ on p_T which is accounted for in the shape systematics.

CHAPTER 4. DISCOVERY

Example 2D templates of $(p_T, m_{4\ell})$ to be used in the analysis are seen in Fig. 4.15.

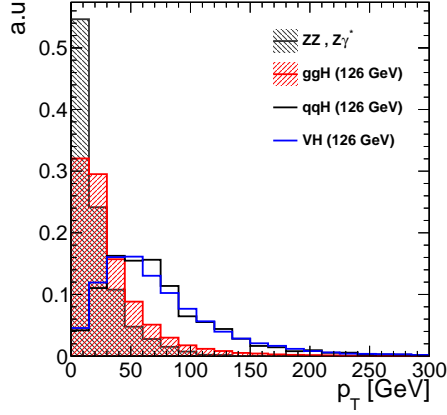


Figure 4.14: p_T distributions for ggF (hashed red), VBF (black), VH (blue), and the dominant $q\bar{q}$ background (hashed black). Subdominant production mechanisms have harder p_T spectra than either ggF or the $q\bar{q}$ background, so it can be used to discriminate production mechanisms.

For any dijet event, the combined kinematics of the jets can be examined. In the initial discovery and property measurements of the Higgs, a matrix element technique was not yet developed so a linear discriminant was built to optimize separation between VBF and ggF production mechanisms. Using the leading and subleading jets, m_{JJ} and $\Delta\eta_{JJ}$ form the two variables for the discriminant. Sample distributions are shown in Fig. 4.16 The optimal combination, trained on POWHEG ggF and VBF samples, is

$$\mathcal{D}_{\text{jet}} = 0.18\Delta\eta_{JJ} + 1.92 \times 10^{-4}m_{JJ} \quad (4.3)$$

CHAPTER 4. DISCOVERY

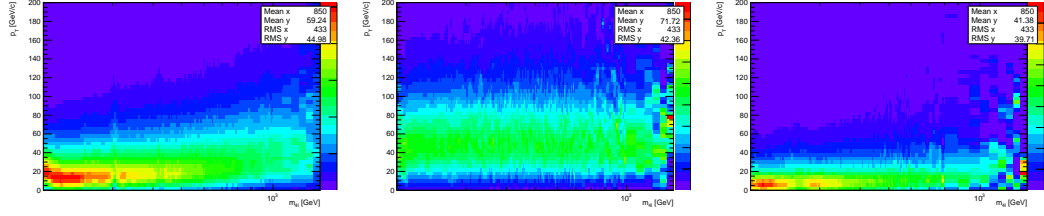


Figure 4.15: Samples of p_T v $m_{4\ell}$ templates for 8 TeV ggF (left), VBF (middle), and $q\bar{q} \rightarrow ZZ$ (right) used in the analysis. Other templates were made and used for WH, ZH, and $gg \rightarrow ZZ$.

This formulation is then implemented for different MC samples (or control region for $Z + X$) to form the 2D ($m_{4\ell}$, \mathcal{D}_{jet}) templates. Shape systematics are applied for each template, coming from the largest deviations in available alternative shapes for the respective sample: choice of MC generator, choice of hadronization tuning, or jet energy scale corrections. Sample templates are seen in Fig. 4.17.

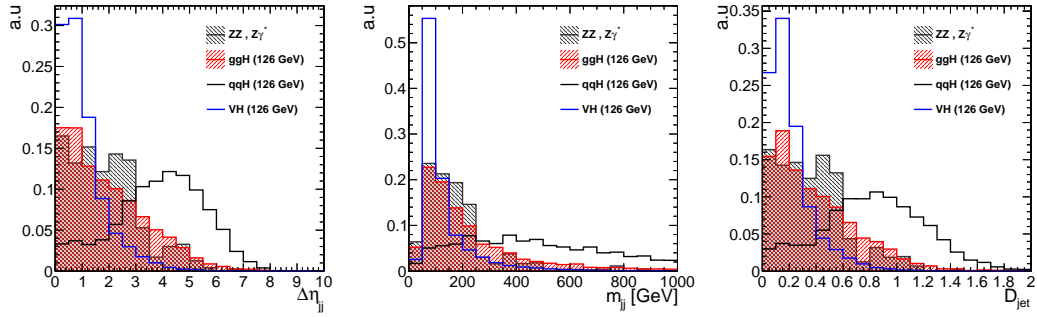


Figure 4.16: $\Delta\eta_{JJ}$ (left) and m_{JJ} (middle) distributions for ggF (hashed red), VBF (black), VH (blue), and the dominant $q\bar{q}$ background (hashed black). These are used as input for the linear discriminant (right, defined in Eq. 4.3).

CHAPTER 4. DISCOVERY

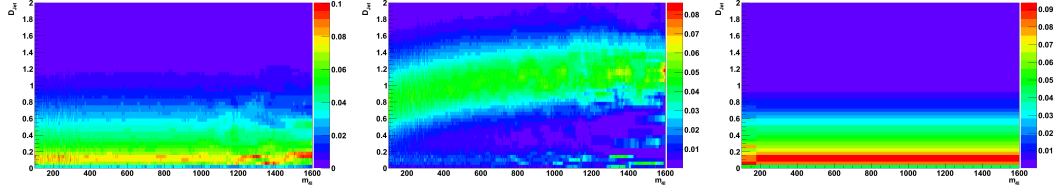


Figure 4.17: Samples of $\mathcal{D}_{\text{jet}} \vee m_{4\ell}$ templates for ggF (left), VBF (middle), and $q\bar{q} \rightarrow ZZ$ (right) used in the analysis. Other templates were made and used for WH, ZH, $t\bar{t}H$, $gg \rightarrow ZZ$, and $Z + X$. As there are no appreciable differences between decay mode (see Figs. 4.12 and 4.13) nor beam energy, one 2D template is used for each production method or background.

On top of any normalization or shape systematics applied, to account for the uncertainty of jet categorization, we used the suggestions of the JetMET group [84]. For ggF, a 15% yield uncertainty is used for the non-dijet category and 30-50% for the dijet category. Given that VBF inherently has two hard jets attached, the uncertainties used are lower: 10% for the 0 jet category and 5% for 1 or 2 jet categories.

4.4.4 Systematic Uncertainties

Broadly speaking, the systematic uncertainties applied are split into two types: normalization uncertainties and shape uncertainties. Normalization uncertainties imply that there is an uncertainty on the overall number of events that will appear

CHAPTER 4. DISCOVERY

(e.g. for a particular decay mode, background). Shape uncertainties mean that there is uncertainty on how those events will appear, independent of the number (e.g. kinematics of the Higgs boson production, mass shape of the background). While shape systematics were discussed in earlier sections with their respective shapes, Table 4.2 contains all common normalization systematics applied in this analysis for the $m_H = 126$ GeV mass point.

Parton distribution functions (PDF), as discussed in Sec. 3.1.2, determine the relative likelihood of the production of different processes at hadronic colliders. Any uncertainty in the initial state can clearly impact the allowed processes, being one of the largest uncertainties for gg production mechanisms. For all normalizations based on MC simulation (i.e. all but $Z + X$), the limitations of the order to which the cross section was calculated imparts an inherent uncertainty on the yields. For $Z + X$, this uncertainty comes instead from the control region, as discussed in Sec. 4.4.1. In any Higgs decay, the acceptance and branching ratio have respective experimental and theoretical uncertainties. Lastly, the luminosity and lepton efficiencies have uncertainties that will affect any yield estimates from MC.

Given the importance of $m_{4\ell}$ to the likelihood of the analysis, per-event mass errors can be constructed. Each lepton that makes up a 4ℓ event has an associated uncertainty, mostly determined by its momentum and location in the detector which were discussed in Sec. 4.1.1 and 4.1.2. The per-event mass uncertainty comes from the product of the sum in quadrature of the four uncertainties and

CHAPTER 4. DISCOVERY

Source	Signal ($m_H = 126$ GeV)				Backgrounds		
	ggF	VBF	VH	$t\bar{t}H$	$q\bar{q} \rightarrow ZZ$	$gg \rightarrow ZZ$	Z + X
$\alpha_S + \text{PDF (} gg \text{)}$	7.2%	—	—	7.8%	—	7.2%	—
$\alpha_S + \text{PDF (} q\bar{q} \text{)}$	—	2.7%	3.5%	—	3.4%	—	—
Missing higher orders	7.5%	0.2%	0.4%, 1.6%	6.6%	2.9%	24%	—
Signal acceptance			2%		—	—	—
$\text{BR}(H \rightarrow ZZ)$			2%		—	—	—
Luminosity				2.6%			—
Electron efficiency			10% (4e), 4.3% (2e2 μ)				—
Muon efficiency			4.3% (4 μ), 2.1% (2e2 μ)				—
Control region	—	—	—	—	—	—	40%

Table 4.2: Normalization uncertainties for signal and background processes in 8 TeV data for $m_H = 126$ GeV in the non-dijet category. Values may change between mass points. 7 TeV uncertainties are similar. Uncertainties on the same line are 100% correlated except for missing higher orders which are uncorrelated and PDF (gg) for $t\bar{t}H$ which are anticorrelated.

CHAPTER 4. DISCOVERY

a calibration constant. Using data and simulation of high cross-section di-lepton decays (Z for di-electron, Z and J/Ψ for di-muon), these per lepton uncertainties can be calibrated. Predicted and observed per-event mass errors show good agreement, within a systematic uncertainty of $\pm 20\%$. A closure test of these errors between data and MC was shown to be in agreement using $Z \rightarrow ll$ events. The uncertainties and the closure test are shown in Fig. 4.18

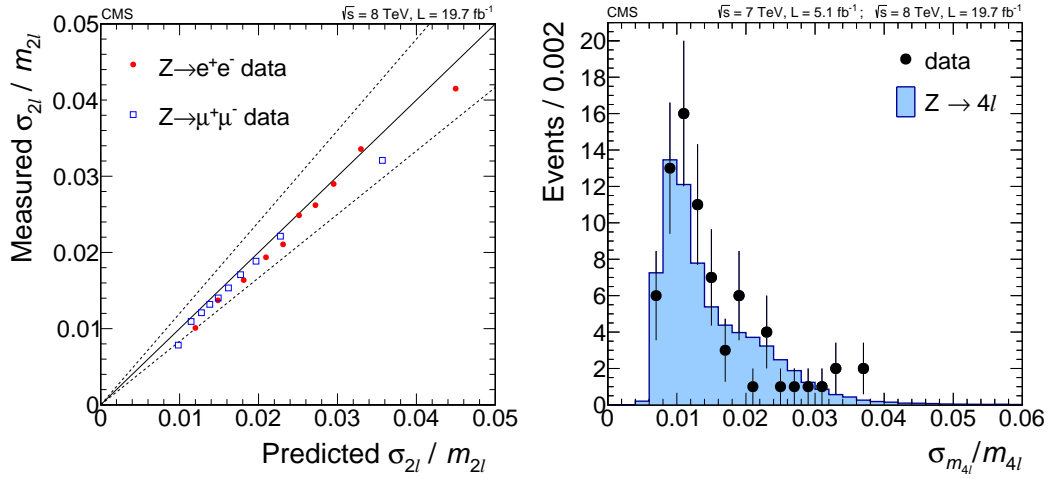


Figure 4.18: On left, a closure test between measured and predicted mass errors shows good agreement between data and MC. On right, the relative mass uncertainty distribution for data and simulation of $Z \rightarrow 4\ell$ events in the $80 < m_{4\ell} < 100$ GeV region.

4.5 Results

After passing all selection requirements, the total number of observed events with $m_{4\ell} > 100$ GeV for 7 & 8 TeV data with background and sample signal estimates are seen in Table 4.3. The total number of observed events is higher than expected from background alone. When looking at the mass distribution of the 4ℓ events in Figures 4.19 and 4.20, there is a localized excess of events over background expectations near 125 – 126 GeV. Table 4.4 details the number of observed and expected events in this localized region, $121.5 < m_{4\ell} < 130.5$ GeV.

Channel	$4e$	$2e2\mu$	4μ	4ℓ
ZZ background	77 ± 10	191 ± 25	119 ± 15	387 ± 31
Z + X background	7.4 ± 1.5	11.5 ± 2.9	3.6 ± 1.5	22.6 ± 3.6
All backgrounds	85 ± 11	202 ± 25	123 ± 15	410 ± 31
$m_H = 500$ GeV	5.2 ± 0.6	12.2 ± 1.4	7.1 ± 0.8	24.5 ± 1.7
$m_H = 800$ GeV	0.7 ± 0.1	1.6 ± 0.2	0.9 ± 0.1	3.1 ± 0.2
Observed	89	247	134	470

Table 4.3: Total number of observed and estimated events after all selection requirements for $m_{4\ell} > 100$ GeV. Estimates for signal and irreducible ZZ background come from MC simulations. Irreducible Z + X background estimates are data-driven.

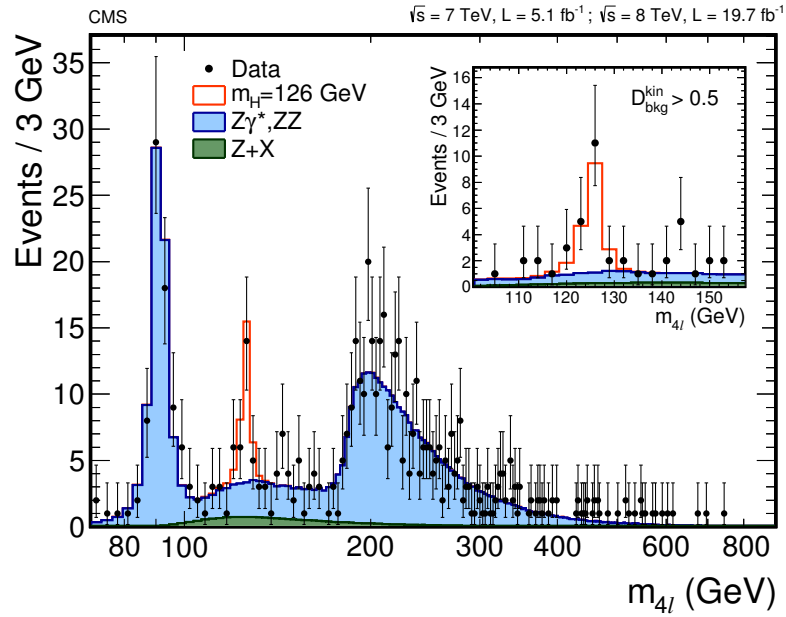


Figure 4.19: Distribution of $m_{4\ell}$ for combined 7 & 8 TeV data, with expected distributions reducible $Z + X$ (green) and irreducible $Z\gamma^*/ZZ$ (blue) backgrounds for $70 < m_{4\ell} < 1000$ GeV. Peaks for $Z \rightarrow 4\ell$ and $ZZ \rightarrow 4\ell$ are observed. An excess of events appears near $m_{4\ell} = 126$ GeV (red). An insert shows the low mass region where a D_{bkg}^{kin} selection is applied to reject ZZ background.

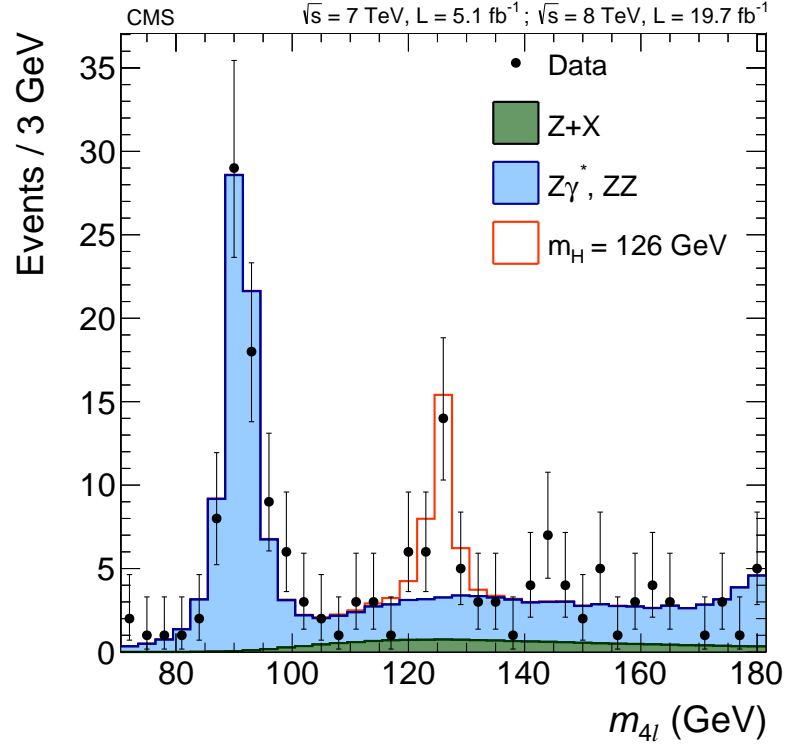


Figure 4.20: Distribution of $m_{4\ell}$ for combined 7 & 8 TeV data, with expected distributions reducible $Z + X$ (green) and irreducible $Z\gamma^*/ZZ$ (blue) backgrounds for $70 < m_{4\ell} < 180$ GeV. Peaks for $Z \rightarrow 4\ell$ and $ZZ \rightarrow 4\ell$ are observed. An excess of events appears near $m_{4\ell} = 126$ GeV (red).

CHAPTER 4. DISCOVERY

Channel	$4e$	$2e2\mu$	4μ	4ℓ
ZZ background	1.1 ± 0.1	3.2 ± 0.2	2.5 ± 0.2	6.8 ± 0.3
Z + X background	0.8 ± 0.2	1.3 ± 0.3	0.4 ± 0.2	2.6 ± 0.4
All backgrounds	1.9 ± 0.2	4.6 ± 0.4	2.9 ± 0.2	9.4 ± 0.5
$m_H = 125$ GeV	3.0 ± 0.4	7.9 ± 1.0	6.4 ± 0.7	17.3 ± 1.3
$m_H = 126$ GeV	3.4 ± 0.5	9.0 ± 1.1	7.2 ± 0.8	19.6 ± 1.5
Observed	4	13	8	25

Table 4.4: Total number of observed and estimated events after all selection requirements for $121.5 < m_{4\ell} < 130.5$ GeV. Estimates for signal and irreducible ZZ background come from Monte Carlo simulations. Irreducible Z + X background estimates are data driven.

CHAPTER 4. DISCOVERY

To test whether any deviation from the background is in agreement with the Higgs boson hypothesis and not just localized statistical fluctuations, we must evaluate the likelihood at different mass points. The unbinned distributions of the kinematics of 4ℓ events that pass selection are examined at 187 different mass points between $100 \leq m_H \leq 1000$ GeV, where each mass point has a window optimized for the expected Higgs boson width at that mass and/or detector resolution. A simultaneous likelihood fit, following the procedure suggested by [85], is used to compute exclusion limits and significance of any excess.

Using a modified frequentist construction¹¹ CL_s [?, 85, 87] to report limits, the 95% confidence level upper limit on the *signal strength* (μ), where $\mu = \sigma_{95\%}/\sigma_{SM}$: the ratio of the produced cross section to the SM cross section, is calculated for a large pseudo-dataset. This means that for a region where it is predicted $\mu > 1$, the upper limit is higher than the SM cross section, so it is not possible to distinguish an excess. The corollary is that the region with expected $\mu \leq 1$ is the *expected exclusion range*. The median of this upper limit, with $\pm 2\sigma$ bands, defines the range of expectations for the background-only hypothesis. Then, the upper-limit of the signal strength can be computed using the observed events. Any mass points within the range of expectations for the background-only hypothesis are in agreement and thus exclude the existence of a signal where $\mu \leq 1$.

For the 4ℓ events, the observed and excluded limits are seen in the left plot

¹¹A Bayesian approach [86] is also consistent with all reported results.

CHAPTER 4. DISCOVERY

of Fig. 4.21. A SM Higgs boson was expected to be excluded in the mass range $115 < m_H < 740$ GeV. The observed 95% CL exclusion limit is the mass ranges $114.5 < m_H < 119.0$ GeV and $129.5 < m_H < 832.0$ GeV. In regions where a signal is not excluded, the standard cutoff used to consider an excess a discovery is a local probability 5σ above¹² the background-only median. The reason for the stringent definition is the *look-elsewhere effect*: the mass of the Higgs boson is unknown, so when probing more mass points, the odds of any one point having an excess over 2σ increases. In the right plot of Fig. 4.21, a local significance of 6.8σ occurs at $m_H = 125.7$ GeV. For a Higgs-like boson at that mass, the expected significance is 6.7σ .

To emphasize the discovery, the distributions of the events for $D_{\text{bkg}}^{\text{kin}}$ and p_T or D_{jet} are plotted over expectations. For the decay kinematics, as seen in Fig. 4.22, the 4ℓ events are plotted over heat maps of background-only $D_{\text{bkg}}^{\text{kin}}$ distributions. In Fig. 4.23, a number of events near $m_{4\ell} = 126$ GeV have higher values of $D_{\text{bkg}}^{\text{kin}}$ in agreement with the expected distribution of background plus $m_H = 126$ GeV signal. In Fig. 4.24, the p_T distribution of the events in the low mass region are plotted over the expected distributions, where the events appear to have slightly higher p_T than expected. In Fig. 4.25, nearly all dijet events occur around $m_{4\ell} = 126$ GeV.

The most pressing properties of the discovered particle to be measured are

¹²Any substantial lack of events would be considered a mismodeling of the background.

CHAPTER 4. DISCOVERY

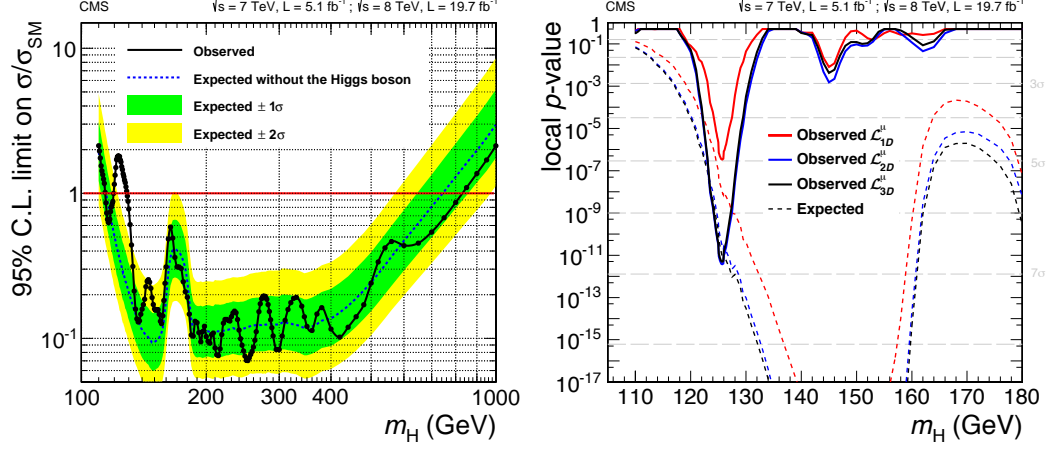


Figure 4.21: On left, expected and observed 95% CL upper limits on signal strength as functions of m_H , using 7&8 TeV data. Dashed black line is the expected limit with 68% and 95% ranges of expectation in green and yellow bands, respectively. Observed limit is solid black line, where the excluded range is $114.5 < m_H < 119.0$ GeV and $129.5 < m_H < 832.0$ GeV. On right, the expected (dashed) and observed (solid) local probability values for $110 < m_H < 180$ GeV. Black lines indicate full 3D likelihoods, red and blue are cross checks using 1D $m_{4\ell}$ and 2D $(m_{4\ell}, D_{\text{bkg}}^{\text{kin}})$ likelihoods, respectively. Horizontal dashed lines reinterpret probability in terms of number of σ . An observed (expected) local significance of 6.8σ (6.7σ) occurs at $m_H = 125.7$ GeV.

CHAPTER 4. DISCOVERY

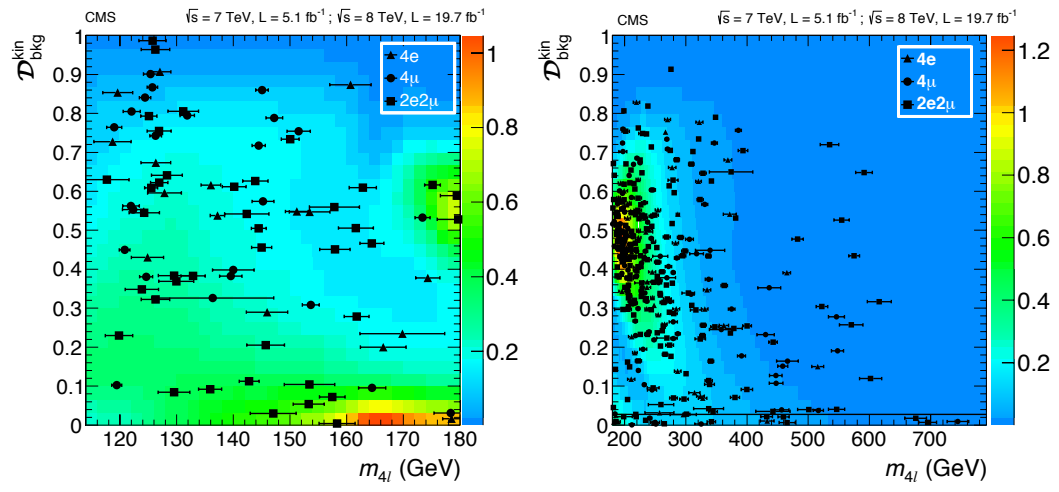


Figure 4.22: $D_{\text{bkg}}^{\text{kin}}$ v $m_{4\ell}$ distributions for 4e (triangles), 4 μ (circles), and 2e2 μ (squares) events with $115 < m_{4\ell} < 180$ GeV (left) and $180 < m_{4\ell} < 800$ GeV (left). Events have per event mass errors. Heat maps correspond to expected distributions for background only.

CHAPTER 4. DISCOVERY

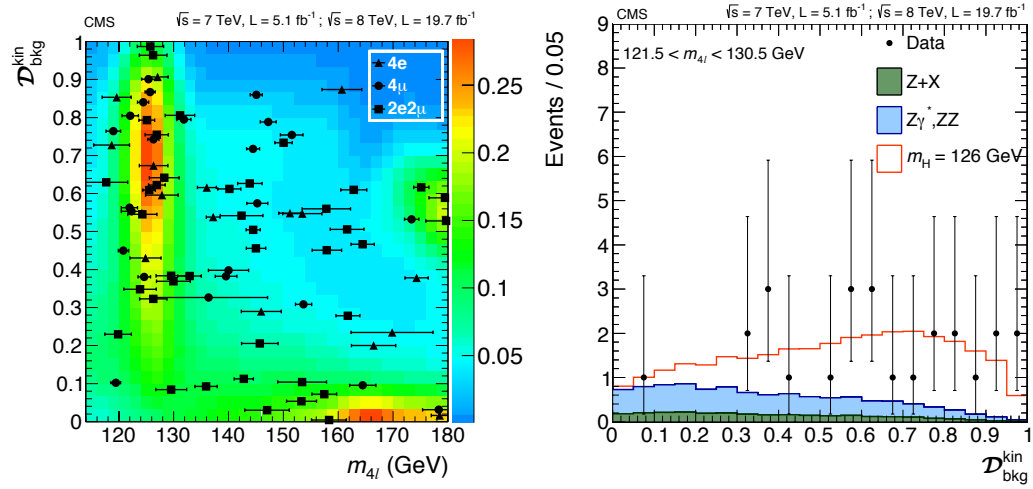


Figure 4.23: On left, $D_{\text{bkg}}^{\text{kin}} \nu m_{4\ell}$ distributions for $4e$ (triangles), 4μ (circles), and $2e2\mu$ (squares) events with $115 < m_{4\ell} < 180$ GeV. Events have per event mass errors. Heat map corresponds to expected distributions for background and $m_H = 126$ GeV signal. On right, projection of $D_{\text{bkg}}^{\text{kin}}$ for events and background expectations in $121.5 < m_{4\ell} < 130.5$ GeV range.

CHAPTER 4. DISCOVERY

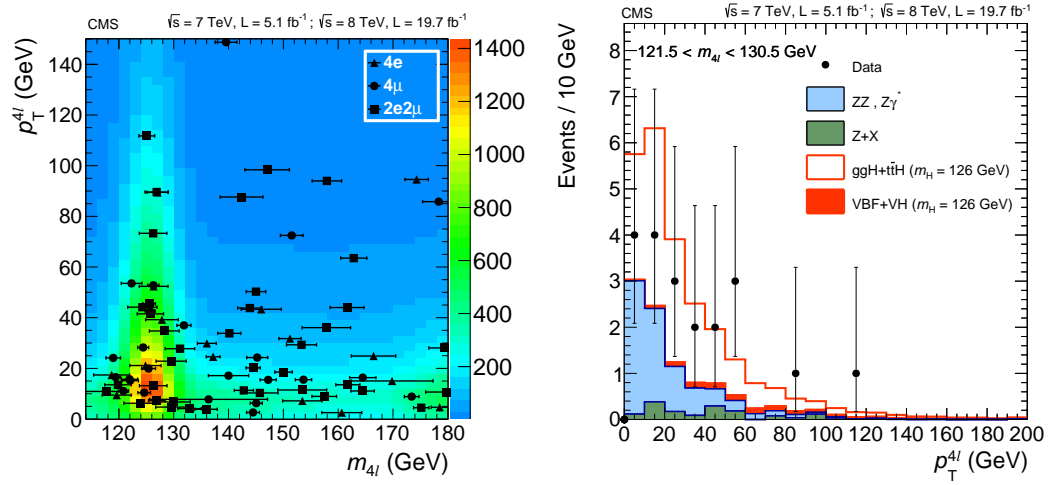


Figure 4.24: On left, p_T v $m_{4\ell}$ distributions for $4e$ (triangles), 4μ (circles), and $2e2\mu$ (squares) events with $115 < m_{4\ell} < 180$ GeV. Events have per event mass errors. Heat map corresponds to expected distributions for background and $m_H = 126$ GeV signal. On right, projection of p_T for events and background expectations in $121.5 < m_{4\ell} < 130.5$ GeV range. Expected signal is split into fermionic (ggF and $t\bar{t}H$) and bosonic ($VBF + VH$) couplings in production.

CHAPTER 4. DISCOVERY

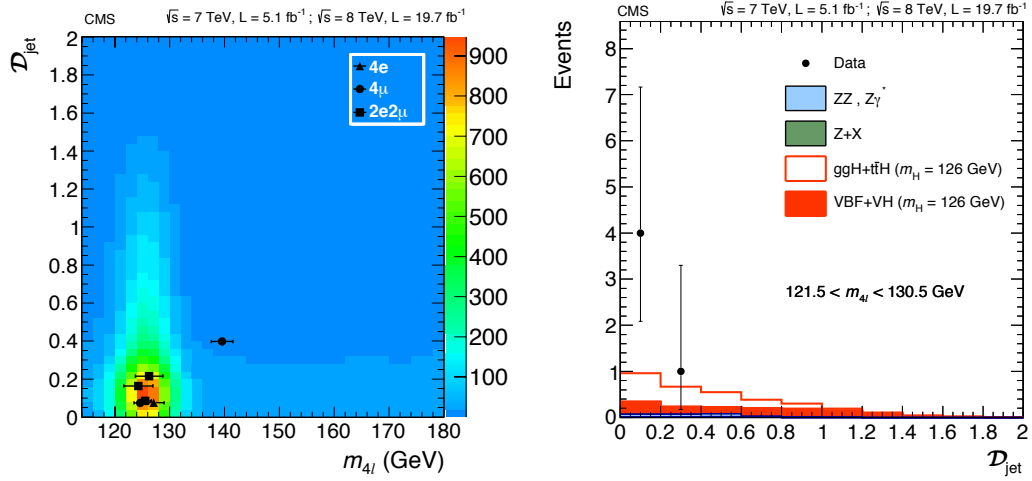


Figure 4.25: On left, \mathcal{D}_{jet} v $m_{4\ell}$ distributions for $4e$ (triangles), 4μ (circles), and $2e2\mu$ (squares) events with $115 < m_{4\ell} < 180$ GeV. Events have per event mass errors. Heat map corresponds to expected distributions for background and $m_H = 126$ GeV signal. On right, projection of \mathcal{D}_{jet} for events and background expectations in $121.5 < m_{4\ell} < 130.5$ GeV range. Expected signal is split into fermionic (ggF and $t\bar{t}H$) and bosonic ($VBF + VH$) couplings in production.

CHAPTER 4. DISCOVERY

its mass and its signal strength. If it is the SM Higgs, as we have seen in Sec. 3 the mass determines many of its other properties. In the region near $m_{4\ell} = 125$ GeV, a different 3D likelihood is built using the same $m_{4\ell}$ distributions and two-dimensional $(m_{4\ell}, \mathcal{D}_{\text{bkg}}^{\text{kin}})$ templates, but replacing the production templates with templates for the per-event mass errors¹³ using a discriminant $\mathcal{D}_m = \sigma_{4\ell}/m_{4\ell}$. The likelihood scan using this technique can be seen in Fig. 4.26. The measured mass is $m_H = 125.6 \pm 0.4(\text{stat}) \pm 0.2(\text{syst})$ GeV where the errors refer to the statistical and systematic uncertainties, respectively.

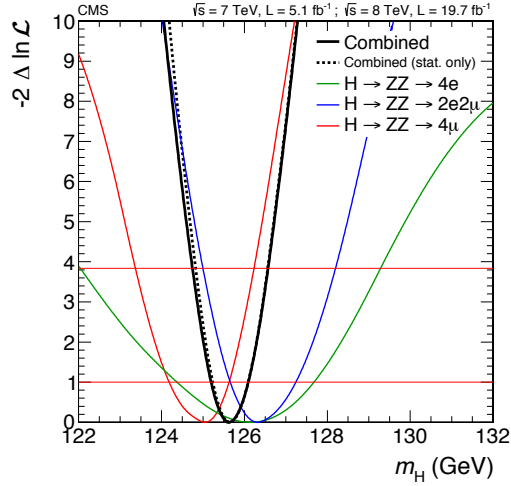


Figure 4.26: Negative log likelihood scan of m_H of the discovered particle. Scans were run independently for $4e$ (green), 4μ (red), and $2e2\mu$ (blue) events with per-event mass errors. Combined observation (black) has minimum value at $m_H = 125.6$ GeV.

¹³Similar to other 2D templates, a distribution from MC (or control region for $Z + X$), was fit using an analytic function.

CHAPTER 4. DISCOVERY

The signal strength of the discovered particle can then be found by evaluating μ at $m_H = 125.6$ GeV. The observed value at this mass is $\mu = 0.93^{+0.26}_{-0.23}(\text{stat})^{+0.13}_{-0.09}(\text{syst})$, in agreement with the expected SM signal strength at $m_H = 125.6$ GeV, $\mu = 1.00^{+0.31}_{-0.26}$. Using the earlier jet categorization, the events are split into the dijet and non-dijet categories as seen in Table 4.5. A signal strength for each category can then be defined, where $\mu_{\text{non-dijet}} = 0.83^{+0.31}_{-0.25}$ for the non-dijet category and $\mu_{\text{dijet}} = 1.45^{+0.89}_{-0.62}$ for the dijet category. This result is shown visually in the left plot of Fig. 4.27.

In Table 4.5, the number of expected SM Higgs boson events are also split by production mechanism. For example, 55% of VBF and 43% of VH events are in the dijet category whereas only 8% of gluon-gluon fusion events are. One might ask whether the excess of dijet events implies that the production mechanisms are in agreement with SM expectations. As discussed in Sec. 4.4.3, p_T or \mathcal{D}_{jet} can disentangle the production mechanisms of the observed events in their respective jet categories. A physically significant grouping of the production mechanisms is whether the coupling is to fermions (ggF, $t\bar{t}H$) or bosons (VBF, VH). In this way, the signal strength can also be reinterpreted into fermionic and bosonic signal strengths, μ_F and μ_V respectively. A two-dimensional fit is performed using these strength modifiers assuming $m_H = 125.6$ GeV and by profiling the likelihood 68% and 95% confidence levels are obtained. In the right plot of Fig. 4.27, the observed values of $\mu_F = 0.80^{+0.46}_{-0.36}$ and $\mu_V = 1.7^{+2.2}_{-2.1}$ are in agreement with the SM Higgs

CHAPTER 4. DISCOVERY

Category	Non-Dijet	Dijet
ZZ background	6.4 ± 0.3	0.38 ± 0.02
$Z + X$ background	2.0 ± 0.3	0.5 ± 0.1
All backgrounds	8.5 ± 0.5	0.9 ± 0.1
ggF	15.4 ± 1.2	1.6 ± 0.3
$t\bar{t}H$	-	0.08 ± 0.01
VBF	0.70 ± 0.03	0.87 ± 0.07
WH	0.28 ± 0.01	0.21 ± 0.01
ZH	0.21 ± 0.01	0.16 ± 0.01
All signal, $m_H = 126$ GeV	16.6 ± 1.3	3.0 ± 0.4
Observed	20	5

Table 4.5: Total number of observed and estimated events after all selection requirements for $121.5 < m_{4\ell} < 130.5$ GeV split by jet categorization. Estimates for signal and irreducible ZZ background come from Monte Carlo simulations. Irreducible $Z + X$ background estimates are data driven. The expected signal yield for a SM Higgs boson with $m_H = 126$ GeV is reported, split by production mechanism.

CHAPTER 4. DISCOVERY

prediction of $(\mu_F, \mu_V) = (1, 1)$. The summary of all signal strengths is found in Table 4.6.

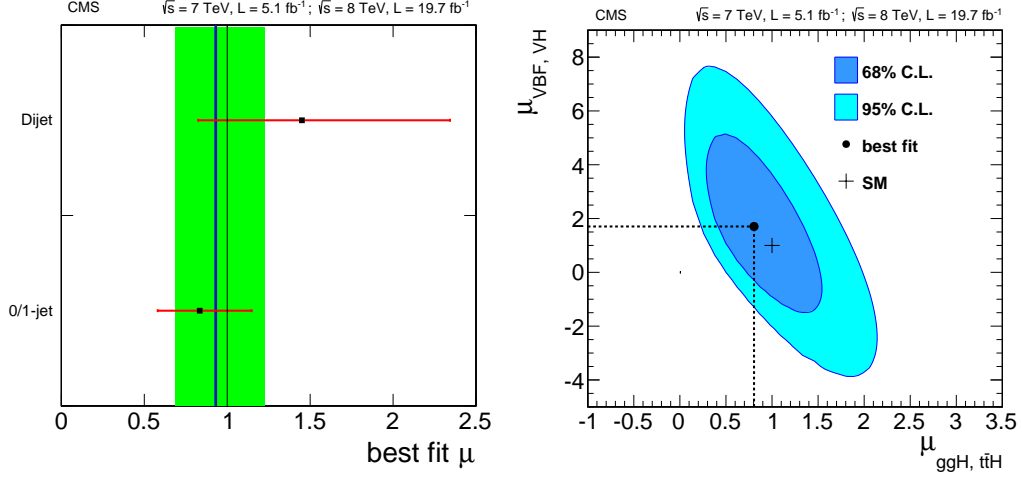


Figure 4.27: Signal strengths of the discovered particle split by jet categorization (left) and production mechanism (right). For jet categorization, SM expected (black) and observed (blue, with $\pm 1\sigma$ green bands) combined signal strengths agree. Points are split signal strengths with red bars for $\pm 1\sigma$ uncertainty. For production mechanism, a 2D expected contour of fermionic ($\mu_{\text{ggH, ttH}} \equiv \mu_F$) and bosonic ($\mu_{\text{VBF, VH}} \equiv \mu_V$) signal strengths is plotted with 68% and 95% confidence levels. Best fit of (0.80, 1.7) is in agreement with SM expectation within uncertainties.

CHAPTER 4. DISCOVERY

Total	Jet Categorization	Coupling Categorization
$\mu = 0.93^{+0.26}_{-0.23}(\text{stat})^{+0.13}_{-0.09}(\text{syst})$	$\mu_{\text{non-dijet}} = 0.83^{+0.31}_{-0.25}$ $\mu_{\text{dijet}} = 1.45^{+0.89}_{-0.62}$	$\mu_F = 0.80^{+0.46}_{-0.36}$ $\mu_V = 1.7^{+2.2}_{-2.1}$

Table 4.6: Summary of Observed 4ℓ Signal Strengths. The total signal strength, μ , is calculated using all observed 4ℓ events. Using jet categorization, the signal strength was found independently for events with 0/1 jets (non-dijet) and events with 2+ jets (dijet). Using the production discriminants and the normalizations in each jet category (Table 4.5), the signal strengths for production mechanisms with fermionic couplings (ggF , $t\bar{t}H$) and bosonic couplings (VBF, VH) are measured as μ_F and μ_V respectively. All signal strengths are in agreement with SM expectations.

4.6 Summary

On July 4, 2012, CMS and ATLAS announced the existence of a newly discovered Higgs-like particle, observed through multiple decay channels expected for the Standard Model Higgs. The “golden” $H \rightarrow ZZ \rightarrow 4\ell$ channel was one of the most sensitive channels in the combined measurement¹⁴ for detection and, along with $H \rightarrow \gamma\gamma$, recorded its mass to be near $m_H = 125$ GeV. Across all decay modes, the observed signal strengths were in agreement with theoretical predictions. Although promising, this did not mean that the new Higgs-like boson could be deemed *the* Standard Model Higgs boson. What if a *second* Higgs-like boson was sitting at a higher mass, as predicted by many BSM theories? What if, contrary to SM, the Higgs had an anomalous spin-parity that could explain the CP-violation in the early universe? Does it appear to decay to other as-of-yet undiscovered particles? In Sec. 5, each of these questions will be discussed further. Discovery was only the first step.

¹⁴The results shown in this chapter are the most up-to-date as of writing, utilizing all recorded 2012 data. With all Run I data included, $H \rightarrow ZZ \rightarrow 4\ell$ is the most sensitive channel.

Chapter 5

Higgs Boson Properties in $ZZ \rightarrow 4\ell$

1 The world is all that is the case.

1.1 The world is the totality of facts, not things.

1.2 The world divides into facts.

Ludwig Wittgenstein, "Tractatus Logico-Philosophicus"

5.1 Prelude to Property Measurements

With a Higgs-like resonance discovered, we analyzed and quantified many properties of the new particle, each of which will be covered in the following sections. Each property measurement uses the same base analysis (i.e. same data, same object definitions, same selection requirements, etc.) as in Sec. 4, with small additions or modifications as needed. Anything that has changed will be listed

CHAPTER 5. PROPERTIES

explicitly. Each of the following property measurements¹ is based on a published paper, cited for further reference. Where applicable, the following measurements were combined with other decay channels. The final results of those combinations will be discussed briefly in each instance.

In Sec. 5.2, a search for additional Higgs bosons was performed [88], which requires a few modifications to how a signal would appear compared to the exclusion limit set for a SM Higgs boson. In Sec. 5.3, the spin-parity of the new resonance was tested against alternative spin states [89]. In Sec. 5.4 we reinterpreted the high mass region into a search for an off-shell enhancement to the Higgs boson $m_{4\ell}$ shape [90]. As we will see, this equates to an upper bound on the width of the new particle, which constrains its ability to decay to yet-unobserved physics. Lastly, in Sec. 5.5, the width measurement can be utilized to set a limit on the last anomalous coupling not covered in Sec. 5.3.

5.2 High Mass Higgs Search

In light of the exclusion limits set in Sec. 4.5, where the SM Higgs boson was excluded in the range $129.5 < m_H < 832.0$ GeV, why repeat the search? As discussed in Chapter 13 of [30], although there is a Higgs-like resonance at 125.6 GeV, if its signal strength was below the expectations of the Standard Model it may not fully explain the mass generation of other particles. In this instance, an additional

¹Except Sec. 5.5, where a paper is moving through the approval process at the time of this thesis.

CHAPTER 5. PROPERTIES

higher mass particle would be required to complete this picture. One such model is called the *Electroweak Singlet model*² (EWS). Although both CMS and ATLAS observe a Higgs boson near 125 GeV, signal strengths of $\mu < 1$ are not excluded so this model is not unreasonable. Additionally, any observed particle in the high mass region would instantly become a very promising candidate for dark matter.

In the EWS model, both the observed 125.6 GeV Higgs boson and any high mass partner would couple to fermions and bosons in the same way as the SM Higgs mechanism, but with modified signal strengths compared to SM predictions. To account for this in the search, the signal line shape used in the high mass region (140 – 1000 GeV for this analysis) is altered slightly from what is defined in Sec. 4.4.1. The heavier particle, hereafter called H where h is the 125.6 GeV particle, adopts different parameters to correct for the lower signal strength and to account for new decay channels³. Defining C and C' as the scale factors compared to the SM signal strengths for h and H respectively, the total signal strength agrees with the standard model by construction: $C^2 + C'^2 = 1$. Then, the signal strength and width of H become

$$\mu' \equiv \mu_H = C'^2(1 - \mathcal{B}_{\text{new}}) \quad (5.1)$$

$$\Gamma' \equiv \Gamma_H = \Gamma_{\text{SM}} \frac{C'^2}{1 - \mathcal{B}_{\text{new}}} \quad (5.2)$$

where \mathcal{B}_{new} is the branching ratio of H to new decay channels.

²So named by the necessity of a new scalar field that would couple to the electroweak sector and acquire a non-zero vacuum expectation energy, similar to the Higgs field.

³Consider the case where $m_H > 2 \times m_h$. In this case, $H \rightarrow hh$ may be possible.

CHAPTER 5. PROPERTIES

As discussed in Sec. 4.4.1, Higgs boson signals below 400 GeV have sufficiently small widths that the shape can be embodied by just a Breit-Wigner function convoluted with a Double Crystal Ball whereas shapes for masses above 400 GeV must be treated with the Complex Pole Scheme. This remains true in the high mass search, but there is the additional complication of non-negligible interference between the signal and background [91] requiring explicit modifications to the signal distributions obtained without interference⁴. Unfortunately, at the time of this analysis, though there were MC generators to make signal-only samples at NLO, MC generators that account for the combined effects of signal, background, and interference only existed at LO.

For ggF, GG2VV was used to generate signal-only (S), background-only (B), and combined signal and background with interference samples (BSI). By generating a background sample plus a combined sample and a signal sample for the same m_H , the shape of interference can be found at LO via subtraction: (Signal+Background+Interference) - (Signal) - (Background) will give the Interference if all samples are weighted by their respective cross sections. But, this interference is only LO, while cross sections are known for signal up to NNLO. To account for this, as discussed in [30], a scale factor can be introduced to rescale interference to NNLO, but there is disagreement as to what should be rescaled. One method

⁴Because the interference is non-negligible at high masses, this means that signal-only shapes for $H \rightarrow 4\ell$ are limited approximations and thus non-physical, even for $m_H < 400$ GeV. However, as the effects of this interference only become relevant for $m_{4\ell} > 2 \times m_Z \gg 125.6$ GeV, this does not weaken the discovery.

CHAPTER 5. PROPERTIES

scales the leading order signal distribution up to NNLO by itself while background and interference are left at LO (*additive method*). Alternatively, the combination of the leading order signal and interference could be scaled by a factor related to the NNLO signal (*multiplicative method*). Instead, this analysis uses an intermediate method for the nominal shape, while the additive and multiplicative methods are used as shape systematics.

To find these interference shapes, it is too computationally intensive to make the signal-only and BSI sample for every mass point, so an analytic shape is built to model interference for different values of m_H and C'^2 which is then applied to the modified Breit-Wigner $m_{4\ell}$ shapes discussed in Sec. 4.4.1. For the EWS $m_{4\ell}$ shapes, this interference is assumed to scale based on the modified coupling such that $(\mu + I)_{\text{BSM}} = \mu_{\text{SM}} C'^2 + I_{\text{SM}} C'$. Lastly, a double-sided Crystal Ball function is again convoluted with these $m_{4\ell}$ shapes to account for resolution effects.

The same process for ggF is pursued for VBF $m_{4\ell}$ shapes, including interference, with the caveat that the LO generator `Phantom` cannot generate a signal-only VBF samples. Instead, two BSI samples are generated: one with $\mu = \mu_{\text{SM}}$ and another with $\mu = 25 \times \mu_{\text{SM}}$. While the signal scales linearly with the signal strength, the interference scales as the square root, that is $BSI_{25 \times \mu_{\text{SM}}} = 25 \times S_{\text{SM}} + 5 \times I_{\text{SM}} + B_{\text{SM}}$. With these two samples and a background-only sample, interference can be extracted for reweighting.

There is one last modification from the analysis of Sec. 4. As VBF becomes in-

CHAPTER 5. PROPERTIES

creasingly important for higher masses (see Sec. 3.1.2), so instead of using a linear discriminant for the dijet category, a full matrix element approach, *vbfMELA*, is used to separated VBF from gluon fusion with two radiated jets (see Sec. 3.2.2). The new discriminant is

$$\mathcal{D}_{\text{jet}} = \frac{\mathcal{P}_{\text{VBF}}}{\mathcal{P}_{\text{VBF}} + c(m_{4\ell}) \times \mathcal{P}_{\text{H+jj}}} \quad (5.3)$$

where the \mathcal{P}_{VBF} and $\mathcal{P}_{\text{H+jj}}$ are probabilities coming from JHUGen matrix elements and $c(m_{4\ell})$ is used to equalize the total probability above and below $\mathcal{D}_{\text{jet}} = 0.5$, similar to $\mathcal{D}_{\text{bkg}}^{\text{kin}}$ in Sec. 4.4.2. This vbfMELA discriminant has a relative improvement of 25-30% over the earlier linear discriminant of Eqn. 4.3, seen in the efficiency curves of Fig. 5.1. Performance of this discriminant was shown to be in agreement with a BDT technique trained over the same production variables, but the MELA approach is motivated directly from a physical argument and will provide a path for other applications (e.g. Sec. 5.5).

Otherwise, the statistical analysis is largely identical to Sec. 4.4. Two-dimensional templates of $(\mathcal{D}_{\text{jet}}, m_{4\ell})$, such as those seen in Fig. 5.2, are made using their respective MC samples (or control region for $Z + X$). For ggF, MINLO is now used to populate the templates as it is known to have more accurate jet kinematics. For VBF, newer samples from POWHEG 1.5 which account for the Complex Pole Scheme are used. A new background-only sample from VBF processes is generated via *Phantom*. The decay of this sample approximately matches the dominant $q\bar{q} \rightarrow ZZ$ background while the p_T matches VBF, used in the 0 and 1 jet categories

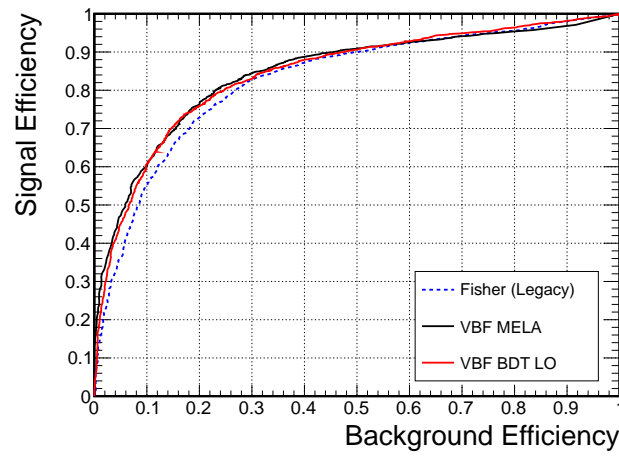


Figure 5.1: Efficiency curves showing the relative performance of the linear discriminant (in dashed blue, labeled Fisher), the vbfMELA discriminant (black) constructed from the production angles, and a BDT (red) trained on the same production variables. The vbfMELA discriminant shows improved performance over the linear discriminant and the BDT method shows similar performance as vbfMELA.

CHAPTER 5. PROPERTIES

respectively. All other MC samples are identical to Sec. 4.2.

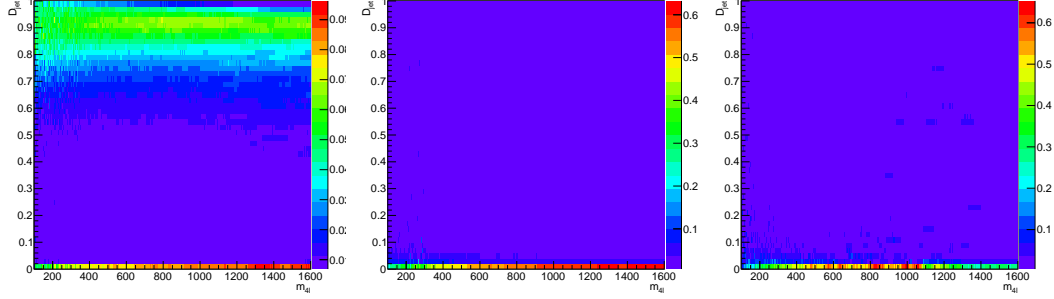


Figure 5.2: Templates of $(\mathcal{D}_{\text{jet}}, m_{4\ell})$ using vbfMELA for VBF (left), ggF (middle), and dominant $q\bar{q} \rightarrow 4\ell$ background (right). These templates replace those seen in Fig. 4.17 and described in Sec. 4.4.3.

For the new $(\mathcal{D}_{\text{jet}}, m_{4\ell})$ templates, the largest shape variations are used from the set of alternate shapes listed in Sec. 4.4.3. Other than the shape systematics applied for the mass shape reweighting, all systematic uncertainties for this high mass analysis are identical to Sec. 4.4.4.

This procedure was combined with other WW and ZZ decay states to put limits on the mass of any SM-like heavy Higgs boson or EWS resonance. For the former, a Higgs boson with SM-like couplings was excluded across the full combined search range of $145 < m_H < 1000$ GeV, as seen in Fig. 5.3. For any BSM resonance, exclusions will change depending on the values of C' and \mathcal{B}_{new} used. As C' becomes arbitrarily small, the number of expected events for a given resonance will tend to zero, so the entire range of possibilities cannot be excluded. As seen in Fig. 5.4, the

CHAPTER 5. PROPERTIES

observed limits on these parameters largely agree with the background only expectations. In sum, from the current data and analysis, the data does not support a high mass Higgs-like resonance in the WW nor the ZZ channels.

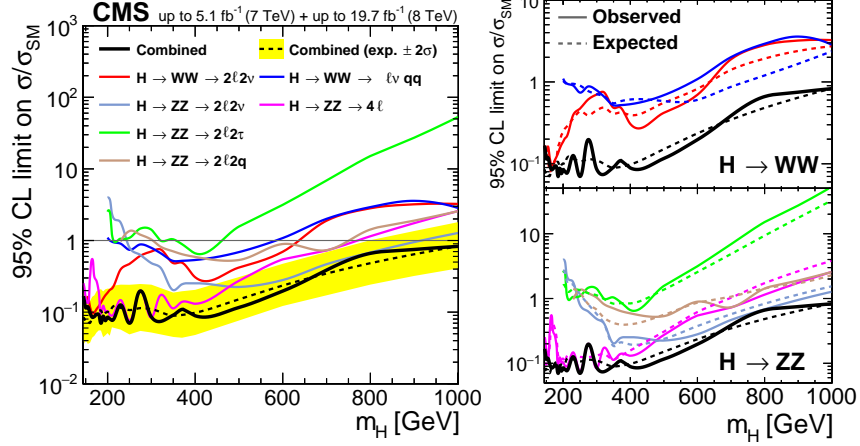


Figure 5.3: Exclusion limits on a Higgs-like high mass resonance in the range $145 < m_H < 1000$ GeV. On left, the combined (black; observed is solid, expected is dashed) and individual limits from all contributing decay channels. For masses below $\lesssim 500$ GeV, $ZZ \rightarrow 4\ell$ is the most sensitive channel while $ZZ \rightarrow 2\ell 2\nu$ is the most sensitive at higher masses. On right, the combined and individual contributions for respective WW and ZZ decay modes show no significant excesses, leading to an observed exclusion of the full range.

CHAPTER 5. PROPERTIES

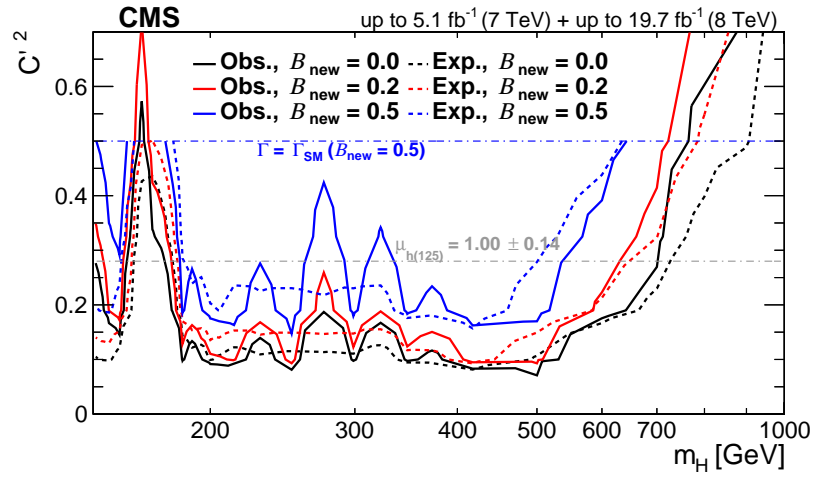


Figure 5.4: Upper Limits at 95% CL for C'^2 for different values of $B_{\text{new}} = 0.0$ (black), 0.2 (red), and 0.5 (blue). For $B_{\text{new}} = 0.5$, the dash-dotted blue line at $C'^2 = 0.5$ corresponds to where the width of the high mass resonance is the same as a SM-like Higgs boson - which has been excluded across this range.

5.3 Higgs Boson Spin-Parity

Based on the calculations from Sec. 3.2.1, we utilized the decay kinematics of the 4ℓ state to separate the SM Higgs boson signal from the dominant $q\bar{q} \rightarrow 4\ell$ background. When searching for the Higgs, this was ideal for discovery. However, now that we have a Higgs boson, what can we say about its spin-parity? It turns out that we can use similar techniques to separate the SM Higgs from different BSM hypotheses and even make measurements as to how tightly this Higgs boson agrees with the Standard Model expectations.

Using the same MELA methods and decay angular distributions, we modify the statistical analysis of Sec. 4.4 by building new discriminants tuned to separate the SM Higgs production from alternative spin-parity models. The LO matrix elements for different spin-parity states are produced using JHUGen while background matrix elements are still generated using MCFM. Both are implemented in the MELA package [31, 33, 34, 92]. Performance of the MELA package was confirmed using the MEKD package [93], based on MadGraph, FeynRules [94], and analytical parameterizations [35, 95, 96]. Dedicated MC samples for each alternative spin-parity state were produced using JHUGen. Observed kinematic distributions in data and expected distributions from MC simulations are seen in Fig. 5.5. A list of alternative spin-parity states that were considered are found in Table 5.1.

CHAPTER 5. PROPERTIES

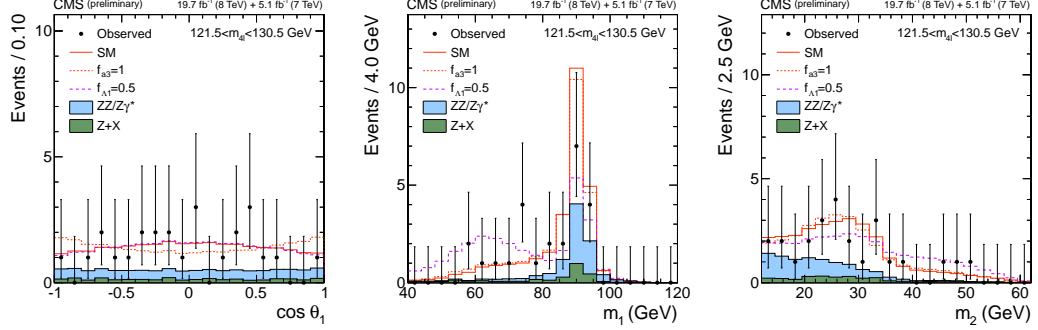


Figure 5.5: Distributions of $\cos \theta_1$, m_{Z1} , and m_{Z2} for $121.5 < m_{4\ell} < 130.5$ GeV. SM Higgs boson (solid red) is compared to a pure-pseudoscalar (dotted red) and $f_{A1} = 0.5$ (dashed magenta) expectations. SM Background distributions for irreducible ZZ (blue) and reducible Z + X (green) also shown.

Spin-0		Spin-1		Spin-2	
J^P	Description	J^P	Description	J^P	Description
0^+	SM Higgs	1^+	Exotic vector	2_b^+	KK Graviton
0^-	Pseudoscalar	1^-	Exotic pseudovector	2_h^+	BSM tensor
0_h^+	BSM Scalar			2_h^-	BSM pseudotensor

Table 5.1: Sample list of alternative models used in the spin-parity analysis. For spin-0, if the observed boson is close to the Standard Model expectations, limits can be set on the fractional components of these states, see Eqn. 3.4. Spin-1 and 2 states were also examined for production dependence. Additional spin-2 states were tested.

CHAPTER 5. PROPERTIES

There are five potentially interesting probabilities to be used:

$$\mathcal{P}_{\text{SM}} \equiv \mathcal{P}_{\text{SM}}^{\text{kin}}(\vec{\Omega}, m_1, m_2 | m_{4\ell}) \times \mathcal{P}_{\text{sig}}^{\text{mass}}(m_{4\ell} | m_H)$$

$$\mathcal{P}_{J^P} \equiv \mathcal{P}_{J^P}^{\text{kin}}(\vec{\Omega}, m_1, m_2 | m_{4\ell}) \times \mathcal{P}_{\text{sig}}^{\text{mass}}(m_{4\ell} | m_H)$$

$$\mathcal{P}_{\text{interf}}^{\text{kin}} \equiv \left(\mathcal{P}_{\text{SM}+J^P}^{\text{kin}}(\vec{\Omega}, m_1, m_2 | m_{4\ell}) - g_{J^P} \mathcal{P}_{J^P}^{\text{kin}}(\vec{\Omega}, m_1, m_2 | m_{4\ell}) - \mathcal{P}_{\text{SM}}^{\text{kin}}(\vec{\Omega}, m_1, m_2 | m_{4\ell}) \right)$$

$$\mathcal{P}_{\text{interf}\perp}^{\text{kin}} \equiv \left(\mathcal{P}_{\text{SM}+J^P\perp}^{\text{kin}}(\vec{\Omega}, m_1, m_2 | m_{4\ell}) - g_{J^P} \mathcal{P}_{J^P}^{\text{kin}}(\vec{\Omega}, m_1, m_2 | m_{4\ell}) - \mathcal{P}_{\text{SM}}^{\text{kin}}(\vec{\Omega}, m_1, m_2 | m_{4\ell}) \right)$$

$$\mathcal{P}_{q\bar{q}ZZ} \equiv \mathcal{P}_{q\bar{q}ZZ}^{\text{kin}}(\vec{\Omega}, m_1, m_2 | m_{4\ell}) \times \mathcal{P}_{q\bar{q}ZZ}^{\text{mass}}(m_{4\ell})$$

where the superscript “kin” implies that the probability is computed from matrix elements that use the decay kinematics and the superscript “mass” utilizes 4ℓ mass parameterizations to determine the probability that an event of that signal or background exists at a given 4ℓ mass. \mathcal{P}_{SM} and $\mathcal{P}_{q\bar{q}ZZ}$ refer to the probabilities associated with the SM Higgs and $q\bar{q}ZZ$ backgrounds respectively and are identical to what was used in Sec. 4.4.2. To discriminate between other pure models, \mathcal{P}_{J^P} refers to the probability associated with a particular spin-parity state (J^P , J referring to the spin and P signifying whether a state is P-even [+] or P-odd [-]). Lastly, for mixed spin-parity states, there will be interference between the two states which necessitates the remaining two interference probabilities⁵.

⁵There are two unfamiliar terms in these interference probabilities: $\mathcal{P}_{\text{SM}+J^P}^{\text{kin}}$ or $\mathcal{P}_{\text{SM}+J^P\perp}^{\text{kin}}$ and g_{J^P} . The probability term comes from a 50%-50% mix between the SM and another J^P state. g_{J^P} is a correction factor.

CHAPTER 5. PROPERTIES

With these probabilities, we again build discriminants:

$$\begin{aligned}\mathcal{D}_{\text{bkg}} &= \frac{\mathcal{P}_{\text{SM}}}{\mathcal{P}_{\text{SM}} + c \times \mathcal{P}_{\text{bkg}}} = \left[1 + c(m_{4\ell}) \times \frac{\mathcal{P}_{\text{bkg}}^{\text{kin}}(m_1, m_2, \vec{\Omega}|m_{4\ell}) \times \mathcal{P}_{\text{bkg}}^{\text{mass}}(m_{4\ell})}{\mathcal{P}_{\text{SM}}^{\text{kin}}(m_1, m_2, \vec{\Omega}|m_{4\ell}) \times \mathcal{P}_{\text{sig}}^{\text{mass}}(m_{4\ell}|m_H)} \right]^{-1} \\ \mathcal{D}_{J^P}^{\text{kin}} &= \frac{\mathcal{P}_{\text{SM}}^{\text{kin}}}{\mathcal{P}_{\text{SM}}^{\text{kin}} + c_{J^P} \times \mathcal{P}_{J^P}^{\text{kin}}} = \left[1 + c_{J^P} \times \frac{\mathcal{P}_{J^P}^{\text{kin}}(m_1, m_2, \vec{\Omega}|m_{4\ell})}{\mathcal{P}_{\text{SM}}^{\text{kin}}(m_1, m_2, \vec{\Omega}|m_{4\ell})} \right]^{-1} \\ \mathcal{D}_{\text{Interf}} &= \frac{(\mathcal{P}_{\text{SM}+J^P}^{\text{kin}} - g_{J^P} \mathcal{P}_{J^P}^{\text{kin}} - \mathcal{P}_{\text{SM}}^{\text{kin}})}{\mathcal{P}_{\text{SM}}^{\text{kin}} + c_{J^P} \times \mathcal{P}_{J^P}^{\text{kin}}}\end{aligned}$$

where \mathcal{D}_{bkg} is very similar to $\mathcal{D}_{\text{bkg}}^{\text{kin}}$ used in Sec. 4.4.2 but the probability for the mass is also included. $\mathcal{D}_{J^P}^{\text{kin}}$ is calculated for each alternative J^P hypothesis and $\mathcal{D}_{\text{Interf}}$ accounts for interference between the alternative J^P shape and the SM shape. As with other discriminants, the constants c_x are used to shift the relative normalizations such that the integrated probability below and above 0.5 are equal. These discriminants are used to populate binned templates for the statistical analysis.

The likelihood analysis changes depending on the spin being examined. As the Higgs boson is expected to be spin-0 from the Standard Model, the analysis is built to quantify any anomalous coupling parameters that would indicate a small deviation from the SM. Following the formalism from Sec. 3.2.1, we aim to extract the parameters from the set $\vec{\xi} = (f_{a2}, \phi_{a2}, f_{a3}, \phi_{a3}, f_{\Lambda 1}, \phi_{\Lambda 1})$. For n_{sig} signal events and n_{bkg} background events, we find the likelihood for N candidate events to be

$$\mathcal{L} = \exp\left(-n_{\text{sig}}(\vec{\xi}) - n_{\text{bkg}}\right) \prod_i^N \left(n_{\text{sig}}^{\text{SM}} \times \mathcal{P}_{\text{sig}}(\vec{x}_i; \vec{\xi}) + n_{\text{bkg}} \times \mathcal{P}_{\text{bkg}}(\vec{x}_i)\right) \quad (5.4)$$

where the probability distribution functions come from the appropriate templates for a particular anomalous coupling measurement. In principle, \mathcal{P}_{sig} depends on

CHAPTER 5. PROPERTIES

all values in $\vec{\xi}$, however we reduce our measurements to only be one or two-dimensional⁶ and fix all other parameters to the SM values. For 1D measurements, \mathcal{P}_{sig} becomes

$$\begin{aligned} \mathcal{P}_{\text{sig}}(\vec{x}_i; f_i, \phi_i) &= (1 - f_i)\mathcal{P}_{0^+}(\vec{x}_i) + f_i\mathcal{P}_{BSM}(\vec{x}_i) \\ &+ \sqrt{f_i(1 - f_i)}[\mathcal{P}_{\text{interf}}(\vec{x}_i)\cos(\phi_i) + \mathcal{P}_{\text{interf}\perp}(\vec{x}_i)\sin(\phi_i)] \end{aligned} \quad (5.5)$$

For 2D measurements, we have

$$\begin{aligned} \mathcal{P}_{\text{sig}}(\vec{x}_i; f_i, f_j) &= (1 - f_i - f_j)\mathcal{P}_{0^+}(\vec{x}_i) + f_i\mathcal{P}_{BSM_1}(\vec{x}_i) + f_j\mathcal{P}_{BSM_2}(\vec{x}_i) \\ &+ \sqrt{f_i(1 - f_i - f_j)}[\mathcal{P}_{\text{interf}}^{0^+, BSM_1}(\vec{x}_i)\cos(\phi_i) + \mathcal{P}_{\text{interf}\perp}^{0^+, BSM_1}(\vec{x}_i)\sin(\phi_i)] \\ &+ \sqrt{f_j(1 - f_i - f_j)}[\mathcal{P}_{\text{interf}}^{0^+, BSM_2}(\vec{x}_i)\cos(\phi_j) + \mathcal{P}_{\text{interf}\perp}^{0^+, BSM_2}(\vec{x}_i)\sin(\phi_j)] \\ &+ \sqrt{f_i f_j}[\mathcal{P}_{\text{interf}}^{BSM_1, BSM_2}(\vec{x}_i)\cos(\phi_i - \phi_j) + \mathcal{P}_{\text{interf}\perp}^{BSM_1, BSM_2}(\vec{x}_i)\sin(\phi_i - \phi_j)] \end{aligned} \quad (5.6)$$

where f_i, ϕ_i come from $\vec{\xi}$ and the BSM_x subscript or superscript refers to the relevant spin-0 model(s).

For Spin-1 and Spin-2, we use the log-likelihood test to separate the SM Higgs boson hypothesis from any alternative spin-parity state. Explicitly, we define the test statistic $q = -2 \ln \frac{\mathcal{L}_X}{\mathcal{L}_{0^+}}$ where the likelihoods are for all events, coming from probability distributions either the SM Higgs (\mathcal{L}_{0^+}) or the alternative hypothesis (\mathcal{L}_X). To quantify the separations, we calculate the probability that the alternative hypothesis has q at the median of the SM expectation. For Spin-1, these

⁶Measurements were also taken allowing the respective phases of each f_i . In this sense, each 1D f_i measurement can be extended to a 2D measurement and each 2D f_i v f_j measurement to a 4D measurement.

CHAPTER 5. PROPERTIES

likelihoods come from 3D probability distributions built from three discriminants, $(\mathcal{D}_{1+}, \mathcal{D}_{1-}, \mathcal{D}_{\text{bkg}})$. For Spin-2, the distributions are 2D built from $(\mathcal{D}_{J^P}, \mathcal{D}_{\text{bkg}})$.

The results of this analysis show that the Higgs boson is widely in agreement with the Standard Model expectations of a spin-0 CP-even particle. In Fig. 5.6, all combinations of spin-1 states are excluded. In Fig. 5.7, all tested spin-2 states are excluded, many beyond 3σ . All observed anomalous fractions agree with the Standard Model expectations ($J^{PC} = 0^{++}$), as seen in Table 5.2. These results, similar to Sec. 5.2, were combined [89] with the WW decay channel to get the limits on anomalous couplings for the HVV vertex, as seen in Fig. 5.8.

Allowed 95% CL intervals		
Parameter ($\phi_{ai} = 0$ or π)	Observed	Expected
$f_{\Lambda 1} \cos(\phi_{\Lambda 1})$	$[-0.25, 0.37]$	$[-1.00, 0.27] \cup [0.92, 1.00]$
$f_{a2} \cos(\phi_{a2})$	$[-0.66, -0.57] \cup [-0.15, 1.00]$	$[-0.18, 1.00]$
$f_{a3} \cos(\phi_{a3})$	$[-0.40, 0.43]$	$[-0.70, 0.70]$

Table 5.2: Summary of allowed intervals for real values of anomalous spin-0 couplings. f_i values are defined between $[-1.0, 1.0]$, by their definitions in Sec. 3.2.

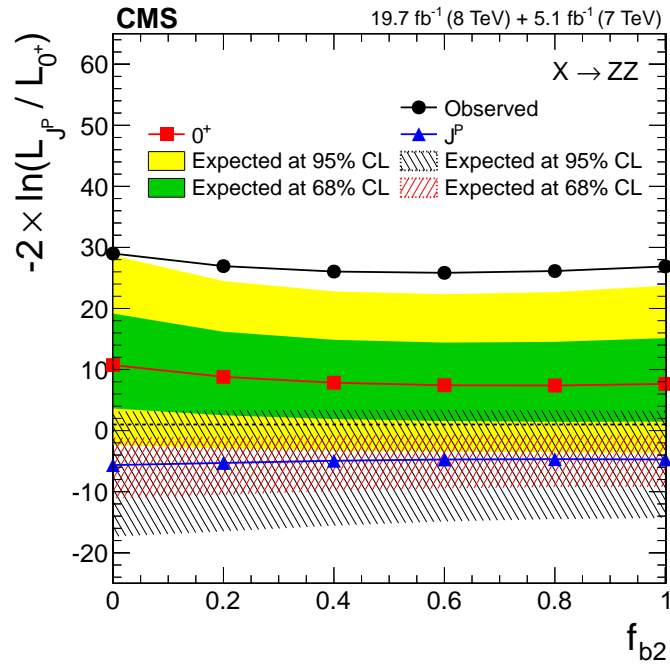


Figure 5.6: Exclusion limit on the fraction of a mixed spin-1 vector and pseudovector state, f_{b2} . Central values of $q = -2 \ln \frac{\mathcal{L}_X}{\mathcal{L}_{0^+}}$ for SM expectations (red squares) and J^P expectations (blue triangles) with $\pm 1\sigma$ and $\pm 2\sigma$ uncertainty bands. Observed points exclude all values of f_{b2} beyond 95% CL.

CHAPTER 5. PROPERTIES

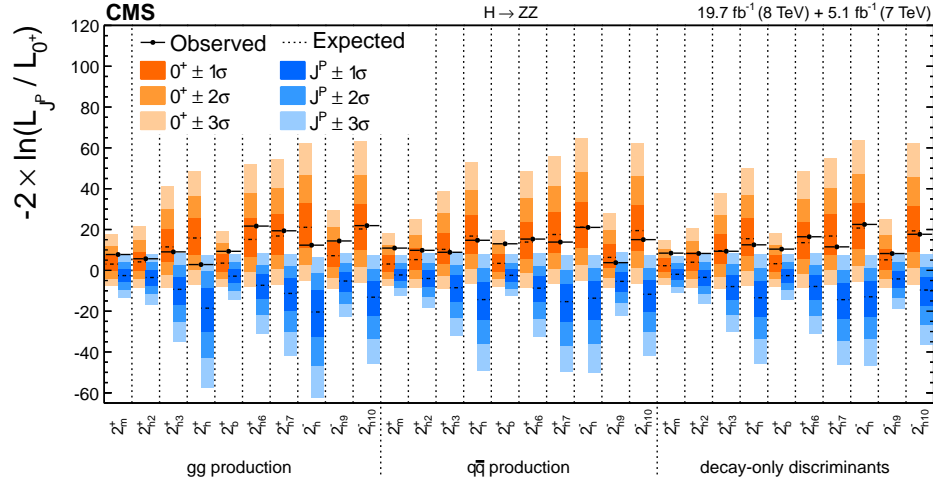


Figure 5.7: Summary of all tested alternative spin-2 hypotheses in 4ℓ channel. Orange bands correspond to $\pm 1\sigma$, $\pm 2\sigma$, and $\pm 3\sigma$ uncertainty bands around SM expectations. Blue bands are for each alternative spin-state. Spin-2 particles have different proportions of production methods, so exclusions were set using gg -only, $q\bar{q}$ -only, and production-independent decay-only discriminants. All tested spin-2 hypotheses are excluded at or above 95% CL.

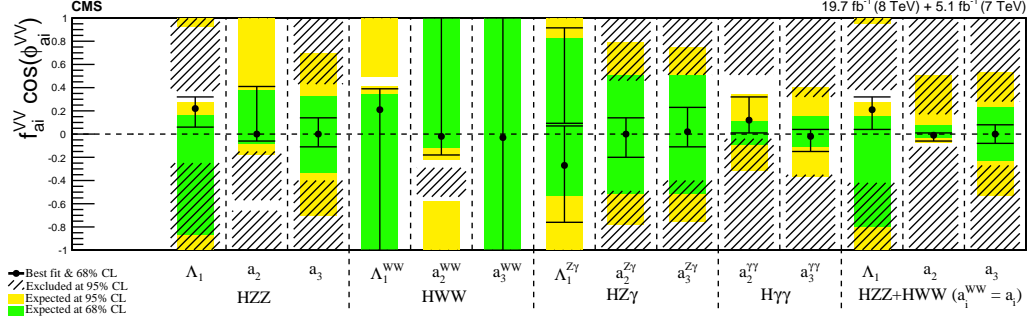


Figure 5.8: Combined limits on real anomalous spin-0 coupling fractions for HVV in CMS. Black points are the best fit values for observations with $\pm 1\sigma$ uncertainty. Black hatched regions are excluded at 95% CL. Green and yellow bands refer to expected regions for SM Higgs boson at 68% and 95% CL, respectively.

5.4 Higgs Boson Width

Using the results of Sec. 4.5, we can reinterpret the mass measurement to put a constraint on the width of the resonance. While the mass measurement assumed a narrow-width resonance, profiling the mass along with the signal strength gives the result in Fig. 5.9. The measured width is $\Gamma_H = 0.0_{-0.0}^{+1.3}$ GeV with an observed upper limit of 3.4 GeV at the 95% CL. For $m_H = 125.6$ GeV, the expected width is 4.15 MeV, about 800 times smaller than this limit. Detector resolution places limits on direct measurements of the Higgs boson width and additional statistics will have little practical impact on this limit. This is unfortunate as a potential sign of new physics is a significant deviation from the Standard Model expectations for the width as it would imply that there are decay channels not included in the

CHAPTER 5. PROPERTIES

calculations. Although these measurements are limited by the resolution, there is another method to measure the width.

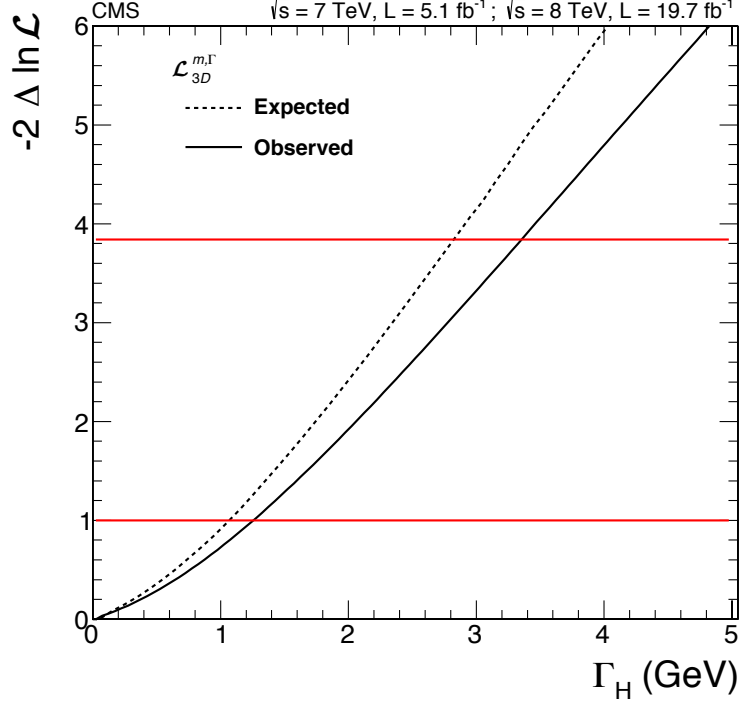


Figure 5.9: Likelihood scans of expected (dashed) and observed (solid) widths obtained using 3D fit for mass measurement. Horizontal lines correspond to 68% and 95% CL upper limits.

5.4.1 Finding the Width in the Off-Shell Region

As argued in Sec. 4.4.1 and Sec. 5.2, for Higgs boson searches where $m_H \lesssim 400$ GeV, the narrow-width approximation can be used to model the behavior near

CHAPTER 5. PROPERTIES

the on-shell peak. However, this approximation is not universally valid. For $H \rightarrow VV$ decays, there will be a substantial off-shell enhancement in the region $m_{VV} > 2 \times m_V$ due to the $2 \times m_V$ threshold⁷ and a further enhancement at the $2 \times m_t$ threshold⁸; nearly 10% of the total cross section for $H \rightarrow ZZ$ will be above $2 \times m_Z$ [53, 97]. When applying the kinematic selection of the 4ℓ channel, this increases to about 20% of the total cross section.

By measuring the off-shell contribution simultaneously with the on-shell, we can make a direct measurement of the total width of the Higgs boson [98]. Generally, the differential cross section of the Higgs boson as a function of $m_{4\ell}$ is

$$\frac{d\sigma_{gg \rightarrow H \rightarrow ZZ \rightarrow 4\ell}}{dm_{4\ell}^2} \sim \sigma_{gg \rightarrow H} \frac{m_{4\ell}^2}{(m_{4\ell}^2 - m_H^2)^2 + m_H^2 \Gamma_H^2} \frac{\Gamma_{H \rightarrow ZZ \rightarrow 4\ell}(m_{4\ell})}{m_{4\ell}} \quad (5.7)$$

where $\sigma_{gg \rightarrow H}$ is the cross section of the Higgs boson produced via gluon-gluon fusion, Γ_H is the total width of the Higgs boson, and $\Gamma_{H \rightarrow 4\ell}$ is the partial width⁹ of the Higgs boson for the $ZZ \rightarrow 4\ell$ decay channel. The zero width approximation (ZWA) finds the on-shell cross section by integrating over a mass region that spans a number of widths near the peak, covering a narrow $m_{4\ell}$ window:

$$\begin{aligned} \sigma_{gg \rightarrow H \rightarrow 4\ell}^{\text{on-shell}} &\sim \sigma_{gg \rightarrow H} m_H \Gamma_{H \rightarrow 4\ell}(m_H) \int_{m_H - n\Gamma_H}^{m_H + n\Gamma_H} \frac{1}{\pi} \frac{1}{(m_{4\ell}^2 - m_H^2)^2 + m_H^2 \Gamma_H^2} dm_{4\ell}^2 \\ &\sim \sigma_{gg \rightarrow H} m_H \Gamma_{H \rightarrow 4\ell}(m_H) \frac{1}{m_H \Gamma_H} = \sigma_{gg \rightarrow H} \frac{\Gamma_{H \rightarrow 4\ell}}{\Gamma_H} \end{aligned} \quad (5.8)$$

⁷Recall the possible decay channels in Sec. 3.1.3, specifically the branching ratio plots of Fig. 3.5. After passing the $2 \times m_V$ threshold, bosonic decays become much more likely. This leads to an off-shell enhancement for $H \rightarrow VV$ decays.

⁸ $gg \rightarrow H$ production requires a fermionic loop, dominated by the contribution from the top quark. When $m_H > 2 \times m_t$, there will be an additional enhancement, as expected via the branching ratios of Fig. 3.5.

⁹If the total width accounts for all possible decay channels, then the partial width comes only from the branching to a particular decay channel.

CHAPTER 5. PROPERTIES

Using an explicit definition¹⁰ of $\sigma_{gg \rightarrow H} \times \Gamma_{H \rightarrow 4\ell} = (\kappa_g \kappa_Z)^2 (\sigma \cdot BR)_{SM} \Gamma_H^{SM}$, with the κ notation¹¹ introduced in [21], we can rewrite the on-shell cross section as

$$\sigma_{gg \rightarrow H \rightarrow 4\ell}^{\text{on-shell}} = \frac{\kappa_g^2 \kappa_Z^2}{\Gamma_H} \Gamma_H^{SM} (\sigma \cdot BR)_{SM} \equiv \mu (\sigma \cdot BR)_{SM} \quad (5.9)$$

which is ultimately what is measured in the on-shell results previously discussed.

There clearly is a degeneracy in this measurement: if the couplings $(\kappa_g^2 \kappa_Z^2)$ and total width of the Higgs boson (Γ_H) scale appropriately, μ will remain unchanged.

This degeneracy can be broken by also looking off-shell. When $m_{4\ell} > 2 \times m_Z$, the $(m_{4\ell}^2 - m_H^2)^2 \approx m_{4\ell}^4$ term in Eqn. 5.7 will dominate the denominator. Ultimately, this means that just past the $2 \times m_Z$ threshold, there will be a plateau in the differential cross section [53, 97], causing an off-shell enhancement in this mass range. Using the high mass approximation, we also find

$$\begin{aligned} \frac{d\sigma_{gg \rightarrow H \rightarrow ZZ \rightarrow 4\ell}^{\text{off-shell}}}{dm_{4\ell}^2} &\sim \sigma_{gg \rightarrow H} \frac{m_{4\ell}^2}{(m_{4\ell}^2 - m_H^2)^2 + m_H^2 \Gamma_H^2} \frac{\Gamma_{H \rightarrow 4\ell}(m_{4\ell})}{m_{4\ell}} \\ &\sim \kappa_g^2 \kappa_Z^2 \cdot \sigma_{gg \rightarrow H}^{SM} \frac{m_{4\ell}^2}{(m_{4\ell}^2 - m_H^2)^2} \frac{\Gamma_{H \rightarrow 4\ell}^{SM}(m_{4\ell})}{m_{4\ell}} \\ &\sim \kappa_g^2 \kappa_Z^2 \cdot \frac{d\sigma_{gg \rightarrow H \rightarrow ZZ \rightarrow 4\ell}^{\text{off-shell, SM}}}{dm_{4\ell}^2}. \end{aligned} \quad (5.10)$$

That is, contrary to the on-shell region, the differential cross section *only* depends on the couplings. If we combine this with the on-shell relation of Eqn. 5.9, we

¹⁰We know from Sec. 2.1 that the cross section can be thought of as the likelihood of a certain process occurring. When we look at the total cross section $\sigma_{gg \rightarrow H}$, we can find the cross section just for $gg \rightarrow H \rightarrow ZZ \rightarrow 4\ell$ by multiplying the total cross section by the branching ratio found via the ratio of widths: $\sigma_{gg \rightarrow H \rightarrow ZZ \rightarrow 4\ell} = \sigma_{gg \rightarrow H} \frac{\Gamma_{H \rightarrow 4\ell}}{\Gamma_H}$.

¹¹The κ notation is used to define the ratios of the measured couplings of particles to the Higgs boson compared to SM expectations, where $\kappa_g = g_{ggH}/g_{ggH}^{SM}$ and $\kappa_Z = g_{HZZ}/g_{HZZ}^{SM}$.

CHAPTER 5. PROPERTIES

arrive at a measurement that can provide the total width of the Higgs boson:

$$\frac{d\sigma_{gg \rightarrow H \rightarrow ZZ \rightarrow 4\ell}^{\text{off-shell}}}{dm_{4\ell}^2} = \mu r \frac{d\sigma_{gg \rightarrow H \rightarrow ZZ \rightarrow 4\ell}^{\text{off-shell, SM}}}{dm_{4\ell}^2} \quad (5.11)$$

where $r = \Gamma_H / \Gamma_H^{SM}$. Explicitly, for a given value of μ , a measurement of the off-shell cross-section of $m_{4\ell}$ is equivalent to a direct measurement of the total width.

5.4.2 Off-Shell 4ℓ Analysis

The strategy to examine the width is to combine the on-shell analysis with a similar analysis in the higher mass off-shell region. Largely, the analyses are similar: the same datasets and MC samples (Sec. 4.2) are used with identical selection requirements (Sec. 4.3). But, there are two additional complications when looking at high masses, which were already encountered in Sec. 5.2: interference of signal and background with the same initial states and the increased role of VBF production.

For interference, we need to expand Eqn. 5.11 to account for the $gg \rightarrow ZZ$ background. As discussed in Sec. 5.2, the interference term will scale as the square root of the signal strength, so Eqn. 5.11 becomes:

$$\frac{d\sigma_{gg \rightarrow 4\ell}}{dm_{4\ell}} = \mu r \frac{d\sigma_{gg \rightarrow H \rightarrow 4\ell}}{dm_{4\ell}} + \sqrt{\mu r} \frac{d\sigma_{\text{interference}}}{dm_{4\ell}} + \frac{d\sigma_{gg \rightarrow ZZ \rightarrow 4\ell}}{dm_{4\ell}} \quad (5.12)$$

To find the $m_{4\ell}$ shapes needed for each component, samples for $gg \rightarrow 4\ell$ were generated at LO using both GG2VV 3.1.5 and MCFM 6.7 with $m_H = 125.6$ GeV.

CHAPTER 5. PROPERTIES

Sample $m_{4\ell}$ shapes generated from GG2VV are shown in Fig. 5.10. Agreement between GG2VV and MCFM samples can be seen in Fig. 5.11.

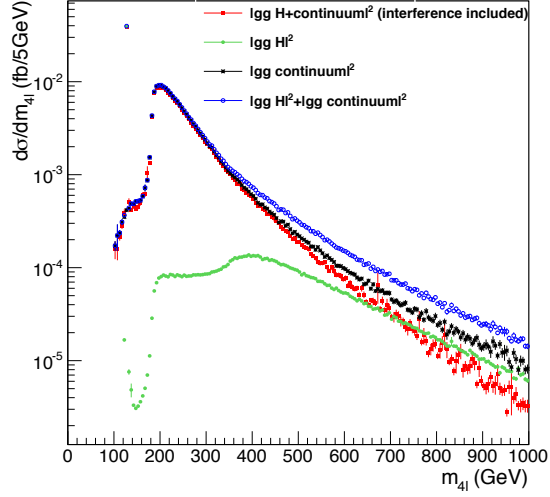


Figure 5.10: Differential cross sections for different processes in $2\ell 2\ell'$ final state and 8 TeV beam energy found at LO from GG2VV. Off-shell signal only (solid green circles) shows enhancement for $m_{4\ell} \gtrsim 2 \times m_Z$ with additional enhancement around $2 \times m_t$. Compared to background only (black crosses) and the unphysical sum of the background and signal (blue open circles), the physical background and signal combination (solid red squares) shows destructive interference.

For VBF and VH off-shell production, as was done in Sec. 5.2, PHANTOM was used to generate the off-shell samples with the same caveat that signal-only shapes cannot be produced directly so linear combinations of samples with different widths can be used to model the signal and interference contributions. Comparisons of

CHAPTER 5. PROPERTIES

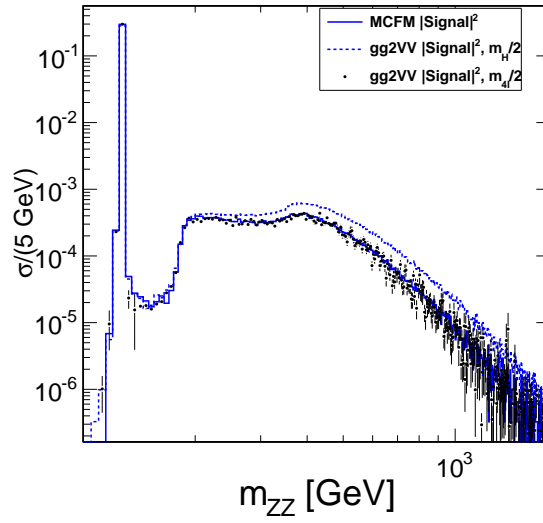


Figure 5.11: Comparison of off-shell signal only $m_{4\ell}$ distributions between GG2VV (blue lines) and MCFM (black dots) generators. When both generators use the same running factorization and renormalization scale (solid blue is fixed scale, dashed blue is running scale), the generators show very good agreement in the off-shell region.

CHAPTER 5. PROPERTIES

VBF and gluon fusion off-shell processes are shown in right plot of Fig. 5.12.

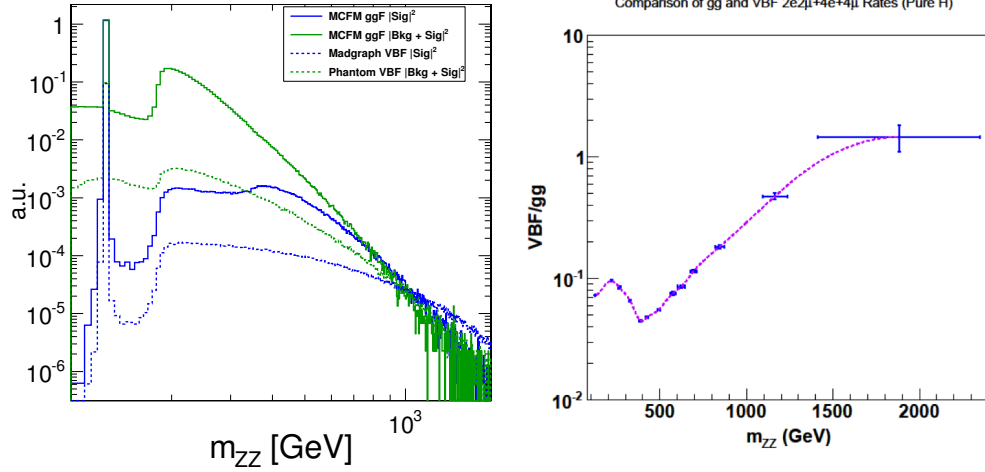


Figure 5.12: On left, differential cross sections for ggF (signal-only [solid blue] and signal plus background with interference [solid green] both from `MCFM`) and VBF (signal-only shape [dashed blue] from `MadGraph`, signal plus background with interference [dashed green] from `Phantom`). As $m_{4\ell}$ increases, the VBF contributions become more dominant, seen in the ratio between VBF and gluon-gluon fusion in the right plot.

Since these background samples are produced at leading order, we need to apply a scale factor to bring the effective cross section to NNLO. As discussed in Sec. 5.2, the scale factor for the Higgs boson signal sample is known to NNLO-NNLL, but no such scale has been calculated for the background or the interference. However, contrary to the High Mass search, the interference is not rolled directly into the signal mass shape and the scale factor could be independent.

CHAPTER 5. PROPERTIES

Fortunately, a study [99] found that the same soft-collinear approximation¹² that largely explains the corrections for the signal is also a good description for NNLO effects on the background. By this logic, we can apply the same scale factor uniformly to background, signal, and interference mass distributions. The scale factor applied, as a function of $m_{4\ell}$, is seen in Fig. 5.13. Because of the limited theoretical knowledge, a systematic uncertainty of 10% is applied to this scale factor from the background. In the on-shell analysis needed for the width measurement, this scale factor has a small impact on the $gg \rightarrow ZZ$ background, but it is applied for consistency. For VBF, an $m_{4\ell}$ independent scale factor is applied to add NNLO QCD corrections of 6%.

To conduct the off-shell analysis, the statistical analysis also needs to be modified from Sec. 4.4 or Sec. 5.2 as we are no longer looking for localized resonances but broad excesses over the high mass region. Each high mass event ($m_{4\ell} \geq 220$ GeV) is assigned a likelihood for the probability that it belongs to a particular signal (ggF or VBF), background, or interference:

$$\mathcal{L}_{\text{off-shell}} = N_{ggZZ} \mathcal{P}_{\text{sig+bkg+int}}^{ggZZ} + N_{VBF} \mathcal{P}_{\text{sig+bkg+int}}^{VBF} + N_{q\bar{q}ZZ} \mathcal{P}_{bkg}^{q\bar{q}} + N_{ZX} \mathcal{P}_{bkg}^{ZX} \quad (5.13)$$

where N_x refers to the number of expected events¹³ and \mathcal{P}^x is the associated normalized probability distribution function for each process. For N_x , it is computa-

¹²Moving to a higher order requires accounting for both additional loops and radiated particles. It has been shown [100] that for gluon fusion, the radiative corrections alone are a good approximation to move to a higher order.

¹³For $gg \rightarrow 4l$ and VBF, the numbers of events depend on the signal strength and thus are fitted values.

CHAPTER 5. PROPERTIES

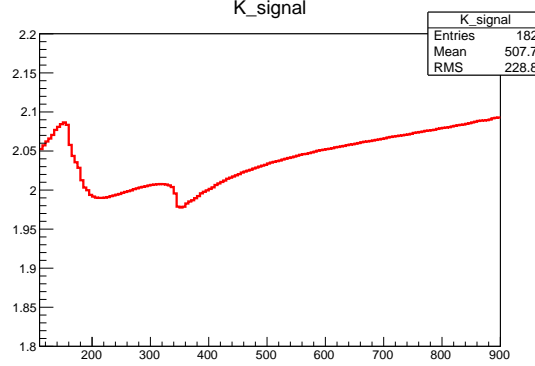


Figure 5.13: Scale factor used to move from LO to NNLO for ggF 8 TeV signal. This factor is applied identically for signal, background, and interference. The scale factor was also calculated for 7 TeV, where the shape is the same but with a magnitude of about 1.6.

tionally expensive to generate MC samples for every value of r . Instead, we use the relation of Eqn. 5.12 for the number of total $gg/VV \rightarrow 4\ell$ events in terms of the SM signal, background, and interference contributions,

$$N_{\text{tot}} = r \times N_{\text{sig}} + \sqrt{r} \times N_{\text{int}} + N_{\text{bkg}}. \quad (5.14)$$

The left plot of Fig. 5.14 shows that the analytic model is in very good agreement with the sample points generated for different values of r . This allows N_{tot} , and therefore the likelihood, to be determined for an arbitrary value of r . An additional closure test using Eqn. 5.12 on the differential cross sections from generated MC samples is shown in the right plot of Fig. 5.14.

In the on-shell analysis, we used three dimensions ($m_{4\ell}$, $\mathcal{D}_{\text{bkg}}^{\text{kin}}$, p_T or \mathcal{D}_{jet}) via an

CHAPTER 5. PROPERTIES

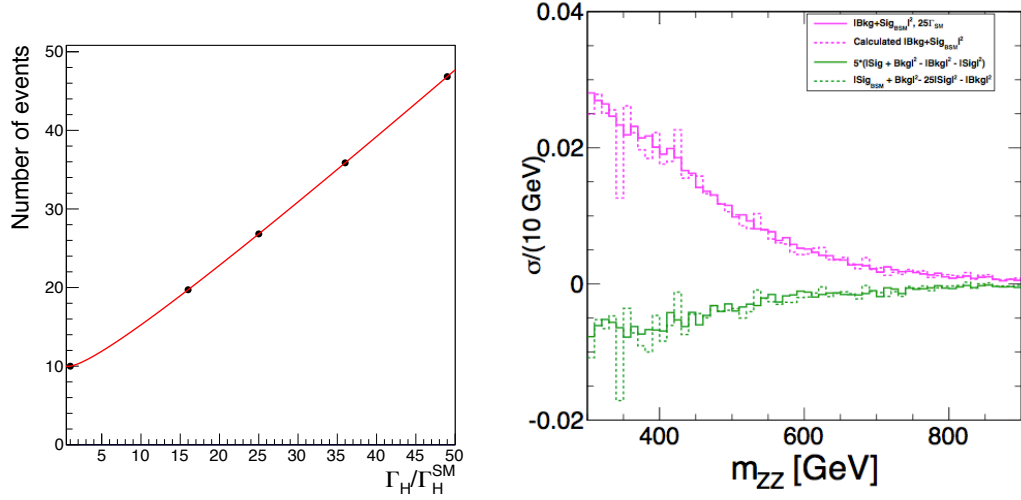


Figure 5.14: On left, an analytic model, Eqn. 5.14 (red), for the total number of signal + background + interference events for gg or $VV \rightarrow 4\ell$ as a function of the width compares very well to five points generated via MC. On right, a closure test where the differential cross sections from MC (solid) is compared against calculated shapes from other samples (dashed). Good agreement is seen both in the shape for the signal + background with interference (magenta) and isolated interference (green) for $r = 25$.

CHAPTER 5. PROPERTIES

analytic $m_{4\ell}$ shape and two 2D templates to build these probability distributions. In principle, the same observables could be used here. However, as we are trying to isolate any $gg \rightarrow 4\ell$ process¹⁴ from the $q\bar{q} \rightarrow 4\ell$ background, we should build a different discriminant to separate these two distributions.

Using the MELA approach outlined in Sec. 3.2.1, we build two probabilities for our discriminant:

$$\mathcal{P}_{gg,a}(\vec{\Omega}, m_1, m_2 | m_{4\ell}, m_H) = a \times \mathcal{P}_{sig}^{gg} + \sqrt{a} \times \mathcal{P}_{int}^{gg} + \mathcal{P}_{bkg}^{gg} \quad (5.15)$$

$$\mathcal{P}_{q\bar{q}}(\vec{\Omega}, m_1, m_2 | m_{4\ell}, m_H) = \mathcal{P}_{bkg}^{q\bar{q}} \quad (5.16)$$

where each probability \mathcal{P} depends on the standard set of decay kinematics and masses $(\vec{\Omega}, m_{4\ell}, m_H)$ used in Sec. 4.4.2 with $m_H = 125.6$ GeV. The parameter a corresponds to the effective signal strength where the Standard Model expectations give $a = 1$. These probabilities are calculated using the MELA package, based on JHUGen and MCFM matrix elements. Then, the new discriminant for the off-shell analysis is:

$$\mathcal{D}_{gg,a} \equiv \frac{\mathcal{P}_{gg,a}}{\mathcal{P}_{gg,a} + \mathcal{P}_{q\bar{q}}} = \left[1 + \frac{\mathcal{P}_{bkg}^{q\bar{q}}}{a \times \mathcal{P}_{sig}^{gg} + \sqrt{a} \times \mathcal{P}_{int}^{gg} + \mathcal{P}_{bkg}^{gg}} \right]^{-1} \quad (5.17)$$

where, following the usual procedure, a correction factor $c(m_{4\ell})$ is included in $\mathcal{P}_{bkg}^{q\bar{q}}$ such that the sum of the probabilities above and below $\mathcal{D}_{gg,a} = 0.5$ are equal. For this discriminant, the value of a must be optimized and should be near the target exclusion of r . Initial studies indicated that $r = 10$ sensitivity is possible and that

¹⁴Recall that for the decay kinematics, there should be nearly no difference between VBF and ggF.

CHAPTER 5. PROPERTIES

the results do not change substantially when a is varied up or down by a factor of 2, so we set $a = 10$ and adopt the shorthand $\mathcal{D}_{gg} \equiv \mathcal{D}_{gg,10}$.

For the probabilities in Eqn. 5.13, we use this discriminant in 2D templates of $(m_{4\ell}, \mathcal{D}_{gg})$ in the off-shell analysis, found via MC¹⁵ (or control region for $Z + X$). The on-shell analysis maintains the same 3D distributions as before. We could use \mathcal{D}_{jet} as well for the off-shell analysis to separate the production mechanisms of any observed off-shell signal events. As the first measurement of width using the off-shell region, we are primarily looking for an excess of Higgs boson-like events which have similar decay kinematics, so to simplify computation we do not use \mathcal{D}_{jet} in this study, but we will revisit the production mechanism in Sec. 5.5. Sample templates of $(m_{4\ell}, \mathcal{D}_{gg})$ are seen in Fig. 5.15.

Thus, the probabilities for VBF and ggF processes in Eqn. 5.13 take the form:

$$\mathcal{P}_{\text{sig+bkg+int}}^{\text{prod}} = \left[r\mu \times \mathcal{P}_{\text{sig}}^{\text{prod}} + \sqrt{r\mu} \times \mathcal{P}_{\text{int}}^{\text{prod}} + \mathcal{P}_{\text{bkg}}^{\text{prod}} \right] \quad (5.18)$$

where the probability distributions are the constructed $(m_{4\ell}, \mathcal{D}_{gg})$ templates. Crucially, the interference template will be negative to account for destructive interference. However, negative probabilities are non-physical, so the full probability $\mathcal{P}_{\text{sig+bkg+int}}^{\text{prod}}$ is normalized to be 1 for $r\mu = 1$ so it is positive-definite. Given these

¹⁵The `Phantom` samples were not fully simulated by the time of this analysis, so two methods were used to build the VBF templates: reweighting the `MCFM` samples using the right plot of Fig. 5.12 and momentum smearing of the `Phantom` samples to mimic detector effects. The variation between these two methods become the dominant shape systematic in the VBF templates.

CHAPTER 5. PROPERTIES

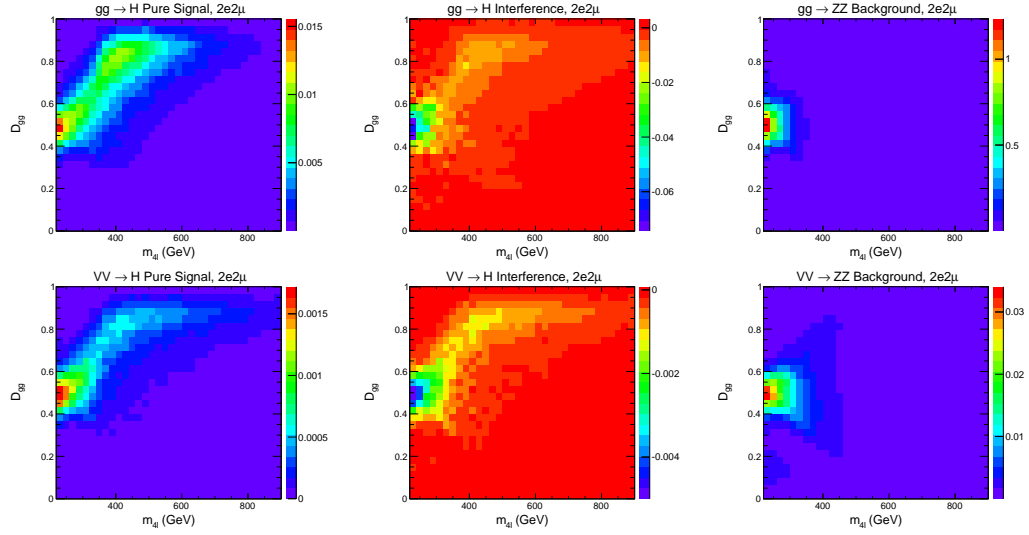


Figure 5.15: $(m_{4\ell}, D_{gg})$ templates for ggF (top row) and VBF (bottom row). Left templates are for signal, middle templates are for interference between signal and background, right templates are for background. The interference is destructive, as indicated by the color negative values in the templates. Additional templates are made for the $q\bar{q} \rightarrow 4\ell$ and $Z + X$ backgrounds.

CHAPTER 5. PROPERTIES

details, the likelihood of Eqn. 5.13 can be rewritten as

$$\begin{aligned}
\mathcal{L}_{\text{off-shell}} = & N_{ggZZ} \left[r\mu_F \times \mathcal{P}_{\text{sig}}^{gg} + \sqrt{r\mu_F} \times \mathcal{P}_{\text{int}}^{gg} + \mathcal{P}_{\text{bkg}}^{gg} \right] \\
& + N_{VBF} \left[r\mu_V \times \mathcal{P}_{\text{sig}}^{VBF} + \sqrt{r\mu_V} \times \mathcal{P}_{\text{int}}^{VBF} + \mathcal{P}_{\text{bkg}}^{VBF} \right] \\
& + N_{q\bar{q}ZZ} \mathcal{P}_{\text{bkg}}^{q\bar{q}} + N_{ZX} \mathcal{P}_{\text{bkg}}^{ZX}
\end{aligned} \tag{5.19}$$

where μ_V and μ_F are the bosonic and fermionic signal strengths, respectively.

Aside from the aforementioned changes, there are a few minor modifications to the systematics listed in Sec. 4.4.4. For the $q\bar{q} \rightarrow ZZ$ background, NLO electroweak corrections [101–103] not available in the earlier analysis of Sec. 4.2 are applied in the nominal $q\bar{q} \rightarrow ZZ$ mass distribution, seen in Fig. 5.16. The interplay between the electroweak corrections and QCD corrections is not known theoretically, so following [104], we implement an uncertainty equal to the product of the two corrections. The factorization, normalization, and signal scale factors were allowed to vary up and down by a factor of 2, where the scale factor uncertainty comes from [105] and the other variations come from the `MCFM` and `GG2VV` generators. For the 2D templates, alternative shapes were built using different PDF sets and the NLO QCD scale variations. Lastly, any systematics that should affect both on-shell and off-shell regions (e.g. normalization) are set to be 100% correlated.

With this analysis in place, we first will look for any large excess of Higgs boson-like events in the off-shell region that would indicate an anomalously large width. Then, using those results, we can simultaneously maximize the likelihoods of the on-shell and off-shell regions to measure the width in the case of an excess

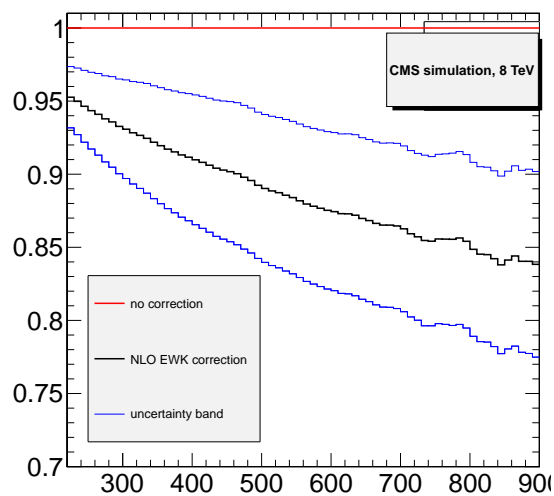


Figure 5.16: NLO electroweak corrections for the $q\bar{q} \rightarrow ZZ$ background as a ratio of the uncorrected background in terms of $m_{4\ell}$. The shape used in on-shell analysis (Sec. 4.4.1) was not corrected (red) as it was published before these corrections were available. A new nominal $q\bar{q} \rightarrow ZZ$ shape was built using the ratio these corrections to the uncorrected shape (black) and $\pm 1\sigma$ uncertainty bands (blue), coming from correlations between QCD and electroweak corrections.

or set an upper limit if no excess is observed.

5.4.3 Width Measurement Using Off-shell Analysis

Utilizing the analysis defined in Sec. 5.4.2, the distribution of 7 and 8 TeV events over the full $m_{4\ell}$ range is shown in Fig. 5.17 with a table of the expected and observed numbers of events are in Table 5.3. There appears to be a slight excess of events near the $2 \times m_Z$ peak, but there are no broad excesses that would indicate an anomalously large width. Given that the off-shell Higgs mass shape plateaus for $m_{4\ell} > 2 \times m_Z$ and that these signal events would have larger values of \mathcal{D}_{gg} , we plot the distributions for $m_{4\ell} > 330$ GeV and $\mathcal{D}_{gg} > 0.65$ in Fig. 5.18, where the yields in this signal-enriched region are in the rightmost column of Table 5.3.

As there are no observed broad excesses, we can set an upper limit on the width of the Higgs boson. Letting μ_V and μ_F float, the expected exclusion limit at 95% CL is $\Gamma_H < 41.9$ MeV. With all systematic uncertainties included, the observed exclusion limit is $\Gamma_H < 33.3$ MeV. This result was further combined with an off-shell analysis in the $ZZ \rightarrow 2\ell 2\nu$ channel¹⁶ to find a combined expected limit of $\Gamma_H < 33$ MeV at 95% CL compared to the observed limit of $\Gamma_H < 22$ MeV. These individual and combined limits can be seen in Fig. 5.19. The combined best fit value for the Higgs width is $\Gamma_H = 1.8^{+7.7}_{-1.8}$ MeV, in agreement with the Standard Model width

¹⁶The $ZZ \rightarrow 2\ell 2\nu$ channel has considerably worse mass resolution than 4ℓ because of the missing energy of the neutrinos, but when combined with on-shell information from 4ℓ its comparatively higher cross section (see Fig. 3.5) leads to a powerful off-shell analysis.

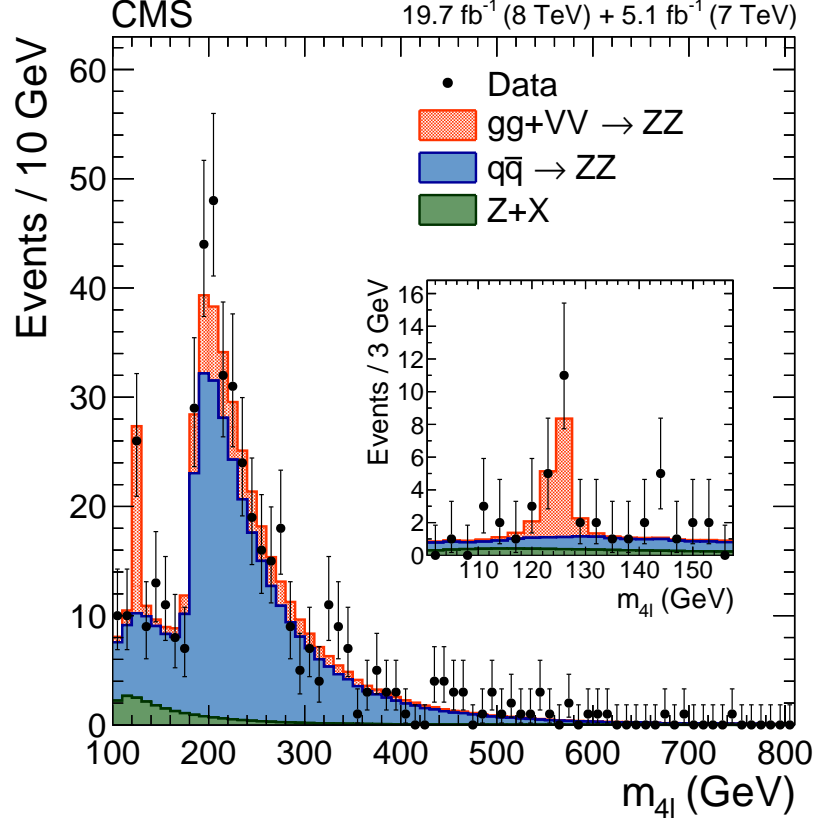


Figure 5.17: Observed 4ℓ events (black points) for on-shell and off-shell regions, $100 < m_{4\ell} < 800$ GeV, with expected distributions with SM-like Higgs boson. $gg + VV \rightarrow ZZ$ distributions (red) account for signal, background, and interference for ggF and VBF production methods. $q\bar{q} \rightarrow ZZ$ (blue) and $Z + X$ (green) are the dominant and sub-dominant backgrounds for the width measurement. The inlaid plot is a narrow region near the Higgs boson peak, $100 < m_{4\ell} < 160$ GeV, where only observed and expected events for $\mathcal{D}_{\text{bkg}}^{\text{kin}} > 0.5$ are plotted. No broad excesses at high mass indicative of an anomalously large width are observed.

CHAPTER 5. PROPERTIES

Final state	4e	2e2 μ	4 μ	All	Enriched
gg signal (SM)	$0.50^{+0.07}_{-0.06}$	$1.19^{+0.13}_{-0.14}$	$0.70^{+0.09}_{-0.09}$	$2.39^{+0.17}_{-0.19}$	$1.32^{+0.09}_{-0.10}$
gg background	$7.5^{+1.4}_{-1.1}$	$17.9^{+2.8}_{-3.0}$	$10.8^{+1.6}_{-1.6}$	$36.2^{+3.4}_{-3.6}$	2.17 ± 0.23
Total gg (SM)	$7.1^{+1.2}_{-1.2}$	$17.0^{+2.5}_{-2.6}$	$9.9^{+1.4}_{-1.6}$	$34.0^{+3.0}_{-3.1}$	$1.82^{+0.17}_{-0.18}$
VBF signal (SM)	0.048	0.115	0.065	0.228	0.119
VBF background	0.49	1.17	0.67	2.33	0.34
Total VBF (SM)	0.43	1.03	0.59	2.05	0.23
$q\bar{q}$	36.2 ± 4.0	87.9 ± 6.4	53.0 ± 3.6	177.1 ± 8.1	9.5 ± 0.5
Reducible	2.2 ± 0.5	1.7 ± 0.4	0.6 ± 0.2	4.5 ± 0.7	0.54 ± 0.09
All contributions (SM)	45.9 ± 4.3	107.6 ± 7.1	$64.1^{+3.9}_{-4.0}$	217.6 ± 9.5	12.0 ± 0.6
Observed	41	122	60	223	10

Table 5.3: Expected and observed number of events with $m_{4\ell} \geq 220$ GeV for each channel and the sum of 4e, 4 μ , and 2e2 μ channels. Listed expectations are for the Standard Model ($\mu = 1$). Total observed events agree with SM expectations within uncertainty. The “Enriched” column are the number of expected and observed events for the signal-enriched region where $m_{4\ell} \geq 330$ GeV and $\mathcal{D}_{gg} > 0.65$. No excess is observed for this region.

CHAPTER 5. PROPERTIES

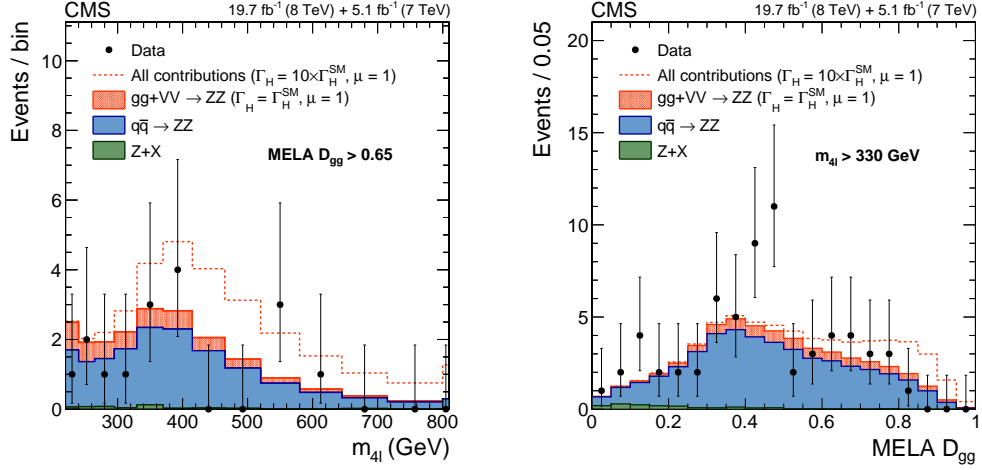


Figure 5.18: Observed 4ℓ events with SM expectations in signal-enriched region. Expectations for $gg + VV \rightarrow 4\ell$, including signal, background, and interference for a SM-like ($r = 1$) Higgs boson width, are in filled red. Expectations for $gg + VV \rightarrow 4\ell$ with $r = 10$ are plotted in dashed red. Irreducible $q\bar{q} \rightarrow 4\ell$ (blue) and reducible $Z + X$ (green) backgrounds are also plotted. On left, $m_{4\ell}$ distribution shows that there are few high mass events in signal-enriched region. On right, \mathcal{D}_{gg} distribution shows that what high mass events exist are typically at lower values of \mathcal{D}_{gg} .

of 4.15 MeV for $m_H = 125.6$ GeV. These limits are substantially stronger than the $\Gamma_H < 3.4$ GeV measurement made only using on-shell information.

5.5 Off-Shell Anomalous Coupling

The width analysis using the off-shell region in Sec. 5.4 relies on two small theoretical assumptions: i) the observed Higgs boson has standard model couplings and ii) the coupling ratios between on-shell and off-shell are well modeled. The first assumption appears to be valid given current measurements. As shown in the results of Sec. 5.3, the Higgs boson is observed to be in agreement with a scalar. The second assumption implies that the fermionic loop of gluon-gluon fusion is dominated by the top quark and there are no BSM particles that contribute to its production. In Sec. 5.2, no Higgs-like resonances were observed in the high mass region and no search [106] for fermions beyond the top-mass has found a higher mass particle.

For the couplings, although anomalous couplings do not have a substantial effect on the on-shell normalization, they do alter the overall cross section seen in the off-shell region. Using MCFM and MELA, simulations of anomalous couplings, seen in Fig. 5.20, will tend to give higher off-shell yields than the Standard Model, which would lead to an even tighter limit on the width. In particular, $f_{\Lambda Q}$, defined in Eqn. 3.6, is the most extreme off-shell enhancement and represents the

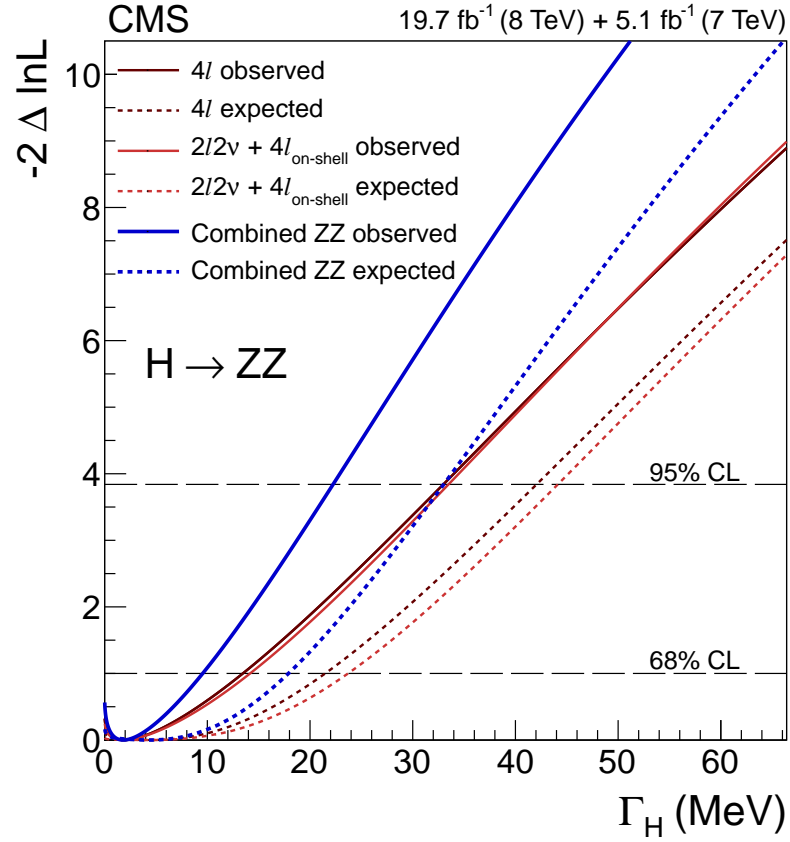


Figure 5.19: Expected (dashed) and observed (solid) likelihood scans for Higgs boson width for $m_H = 125.6$ GeV using the full 4ℓ mass range (dark red), the $2\ell 2\nu$ channel off-shell mass range with 4ℓ on-shell (light red), and combined (blue). In both channels, a dearth of events is observed leading to a tighter observed limit at 95% CL, $\Gamma_H < 22$ MeV, than the expected $\Gamma_H < 33$ MeV.

CHAPTER 5. PROPERTIES

scale of BSM physics that modifies the HVV vertex. Furthermore, this anomalous coupling can *only* be measured through this off-shell enhancement as all kinematic distributions become identical to the SM. By modifying the off-shell analysis of Sec. 5.4.2, we can simultaneously measure the final anomalous coupling of Eqn. 3.3 and loosen the assumptions in the width measurement.

Because $f_{\Lambda Q} \neq 0$ will have the same kinematic distributions as $f_{\Lambda Q} = 0$, the off-shell analysis can be adapted simply by modifying the $m_{4\ell}$ distributions of the $(m_{4\ell}, \mathcal{D}_{gg})$ templates to reflect the value of $f_{\Lambda Q}$. This reweighting can be done using the following equations¹⁷:

$$\begin{aligned}\mathcal{P}_{\text{sig}}^{\text{gg}} &= \left| \sqrt{1 - f_{\Lambda Q}} - \sqrt{f_{\Lambda Q}} e^{i\phi_{\Lambda Q}} \cdot \frac{m_{ZZ}^2}{m_H^2} \right|^2 \cdot \mathcal{P}_{\text{sig}}^{\text{gg}}(\text{SM}) \\ \mathcal{P}_{\text{int}}^{\text{gg}} &= \text{Re} \left(\sqrt{1 - f_{\Lambda Q}} - \sqrt{f_{\Lambda Q}} e^{i\phi_{\Lambda Q}} \cdot \frac{m_{ZZ}^2}{m_H^2} \right) \cdot \mathcal{P}_{\text{int}}^{\text{gg}}(\text{SM}) \\ \mathcal{P}_{\text{sig}}^{\text{VBF}} &= \left| \sqrt{1 - f_{\Lambda Q}} - \sqrt{f_{\Lambda Q}} e^{i\phi_{\Lambda Q}} \cdot \frac{m_{ZZ}^2}{m_H^2} \right|^4 \cdot \mathcal{P}_{\text{sig}}^{\text{VBF}}(\text{SM}) \\ \mathcal{P}_{\text{int}}^{\text{VBF}} &= \left| \sqrt{1 - f_{\Lambda Q}} - \sqrt{f_{\Lambda Q}} e^{i\phi_{\Lambda Q}} \cdot \frac{m_{ZZ}^2}{m_H^2} \right|^2 \cdot \mathcal{P}_{\text{int}}^{\text{VBF}}(\text{SM})\end{aligned}$$

Note that for VBF, because there are two HVV vertices – one in production and one in decay – the $f_{\Lambda Q}$ enhancement is two powers stronger for VBF signal than ggF signal. For large values of m_{ZZ} , the $\sqrt{f_{\Lambda Q}}$ term will dominate unless $f_{\Lambda Q}$ is very small. This implies that we should expect a very narrow limit on $f_{\Lambda Q}$ as no 4ℓ event is observed for $m_{4\ell} > 800$ GeV.

For the earlier width measurement, the limit was set using the total number

¹⁷Where the phase $\phi_{\Lambda Q} = 0$ or π , where the coupling would be real.

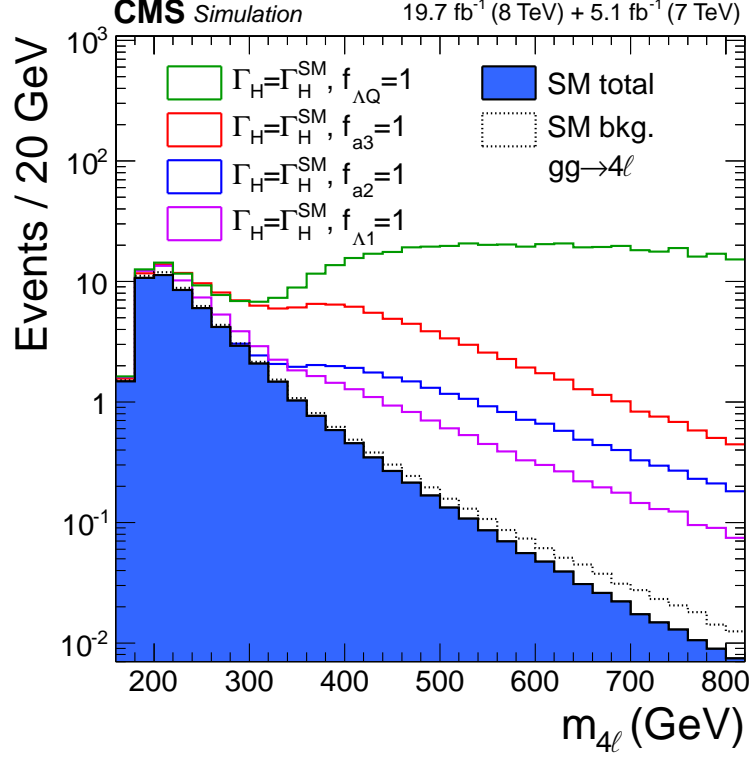


Figure 5.20: Compared to the SM off-shell yields in 4ℓ (total $gg \rightarrow 4\ell$ in filled blue, background only in dotted black), anomalous couplings will tend to give considerable enhancements. Modeled using MCFM and MELA anomalous couplings, $f_{\Lambda Q} = 1$ (green), $f_{a3} = 1$ (red), $f_{a2} = 1$ (blue), and $f_{\Lambda 1} = 1$ (magenta) were generated for demonstration of these effects. Arbitrary anomalous couplings can be generated and $f_{\Lambda Q} = 1$ is the most extreme enhancement compared to SM.

CHAPTER 5. PROPERTIES

of off-shell events with a separation of Higgs boson signal from background using decay kinematics. With the stronger off-shell enhancement being for VBF, we should again implement production separation in the off-shell region. In Sec. 4.4.3, a jet categorization determined which production discriminant (p_T or \mathcal{D}_{jet}) to use on events in the on-shell likelihood. For the off-shell region, instead of using the jet categorization, we implement a new categorization built on vbfMELA. Looking at the \mathcal{D}_{jet} distributions of VBF against either ggF or $q\bar{q}ZZ$ in Fig. 5.2, we categorize events by their value of \mathcal{D}_{jet} with one category for events with $\mathcal{D}_{\text{jet}} \geq 0.5$ and the other category with $\mathcal{D}_{\text{jet}} < 0.5$ or having less than two jets. The full list of observables and categories for the on-shell and off-shell regions is in Table 5.4.

Category	$m_{4\ell}$	Jets	Observables \vec{x}		
On-shell Dijet	$105.6 < m_{4\ell} < 140.6 \text{ GeV}$	$N_{\text{jet}} \geq 2$	$m_{4\ell}$	$\mathcal{D}_{\text{bkg}}^{\text{kin}}$	\mathcal{D}_{jet}
On-shell Non-Dijet	$105.6 < m_{4\ell} < 140.6 \text{ GeV}$	$N_{\text{jet}} < 2$	$m_{4\ell}$	$\mathcal{D}_{\text{bkg}}^{\text{kin}}$	p_T
Off-shell Dijet	$220 < m_{4\ell} < 1600 \text{ GeV}$	$\mathcal{D}_{\text{jet}} \geq 0.5$	$m_{4\ell}$	\mathcal{D}_{gg}	
Off-shell Non-Dijet	$220 < m_{4\ell} < 1600 \text{ GeV}$	$\mathcal{D}_{\text{jet}} < 0.5$ or $N_{\text{jet}} < 2$	$m_{4\ell}$	\mathcal{D}_{gg}	

Table 5.4: On-shell and off-shell jet categorizations and observables used for likelihood analysis. On-shell region is identical to method of Sec. 4.4 near $m_H = 125.6$ GeV except that vbfMELA is used for \mathcal{D}_{jet} as in Sec. 5.2. Off-shell region is identical to method used in Sec. 5.4.2, with added jet categorization based on \mathcal{D}_{jet} .

The $\mathcal{D}_{\text{jet}} \geq 0.5$ category will be remarkably pure in VBF, where less than 5%

CHAPTER 5. PROPERTIES

of ggF or background events pass this threshold compared to about 40% of VBF events, as seen in the ratios of Fig. 5.21. Given that these ratios are very small for all but VBF, the $(m_{4\ell}, \mathcal{D}_{gg})$ templates for each category are built using the full MC or control region then scaled by analytic $m_{4\ell}$ fits of the $\mathcal{D}_{\text{jet}} > 0.5$ ratio to give the appropriate normalization. VBF has sufficient statistics in each category to build separate templates from each subset of simulated events.

For VBF and $q\bar{q}$, the nominal \mathcal{D}_{jet} ratios come from the respective MC samples that were used in the earlier off-shell analysis. For ggF, as discussed in Sec. 5.2, the jet kinematics of MINLO is more accurate than POWHEG or other LO generators, so the nominal ratio used for categorization is found from MINLO. In implementing the $\mathcal{D}_{\text{jet}} > 0.5$ selection, we studied the effects of using alternative MC for the purpose of adding a yield systematic for the jet categorization. For VBF, Phantom and JHUGen at LO were compared to POWHEG at NLO. The relative uncertainty in the yield of the $\mathcal{D}_{\text{jet}} > 0.5$ category is about 5%. Similar studies were done in ggF (MCFM and GG2VV at LO, POWHEG and MINLO at NLO) and $q\bar{q}ZZ$ (POWHEG at NLO and MadGraph for an inclusive sample with up to 2 jets), where relative yield uncertainties were found to be 15% and 25%, respectively. $Z + X$ is data driven, so the nominal shape comes from the control region with a conservative 100% uncertainty on the dijet yield. These new yield uncertainties¹⁸ are 100% anti-

¹⁸The considered shape uncertainties of \mathcal{D}_{jet} in Sec. 4.4.3 can be reinterpreted as yield uncertainties for the $\mathcal{D}_{\text{jet}} > 0.5$ categorization. The largest available deviations come from different MC generators.

CHAPTER 5. PROPERTIES

correlated between the non-dijet and dijet categorizations to maintain the same total normalization.

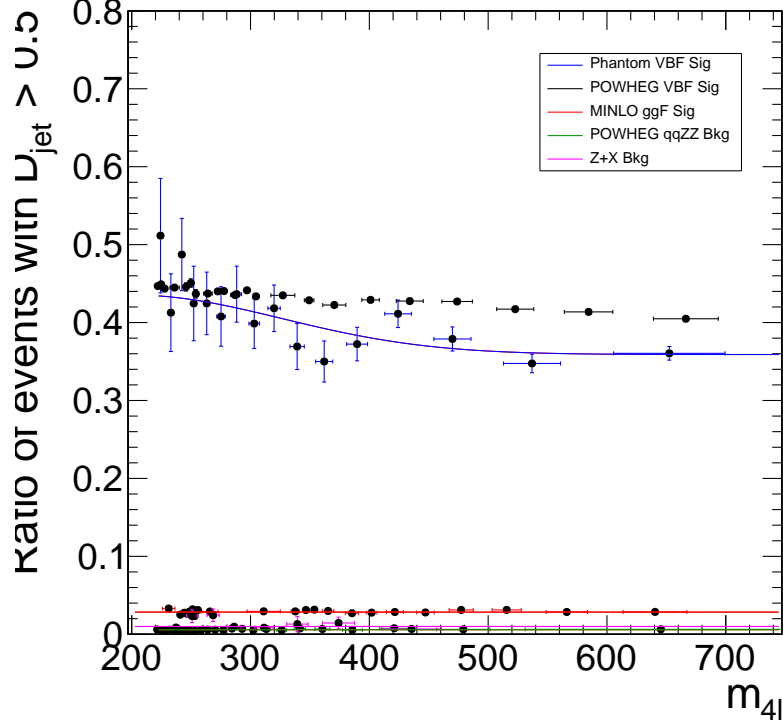


Figure 5.21: Ratios of events that pass $D_{\text{jet}} > 0.5$ categorization over total number of events. VBF (blue) has the highest ratios, around 40% over a wide $m_{4\ell}$ range. ggF (magenta), $Z + X$ (green), and $q\bar{q}ZZ$ (red) all have much lower ratios, sub 5%. Aside from VBF, these ratios are fit analytically to build templates for each category.

Other than the new jet categorization using vbfMELA to isolate the elevated impact on VBF and the modification of the templates for values of $f_{\Lambda Q}$, there are

CHAPTER 5. PROPERTIES

only small changes from the analysis of Sec. 5.4.2. For VBF, the `Phantom` samples were fully simulated through the detector by the time of this analysis, so they are used for creating the templates with a minor reweighting. VH is a small contribution (about 10-15% relative to VBF for $m_{4\ell} \gtrsim 200$ GeV) in the off-shell region and these `Phantom` samples include its contribution, but only when the associated W or Z decays hadronically. A small reweighting is applied to account for the additional leptonic decays.

With these changes in place, we still have the same $m_{4\ell}$ distributions as in Fig. 5.17, but we also plot the $m_{4\ell}$ distributions separately for each jet categorization. In the left plot of Fig. 5.22, we have applied a $\mathcal{D}_{gg} > 0.67$ selection to emphasize the signal-enriched region. As with Fig. 5.18, there are few signal-like events in the off-shell region, which led to the upper limit measurement on the width. When $f_{\Lambda Q}$ is small, destructive interference will bring down the contribution of an anomalously large width. However, as $f_{\Lambda Q}$ increases, the number of signal-like events expected at very high masses ($m_{4\ell} > 800$ GeV) increases, most obviously in the $\mathcal{D}_{\text{jet}} > 0.5$ category in the right plot of Fig. 5.22.

The impact of the destructive interference for small values of $f_{\Lambda Q}$ means that the width limit will loosen somewhat when $f_{\Lambda Q}$ is allowed to vary. This is exactly what is seen in Fig. 5.23, where the likelihood scans were run both using $f_{\Lambda Q} = 0$ – identical to Sec. 5.4.3 – and when we unconstrain $f_{\Lambda Q}$. The expected and observed limits for $f_{\Lambda Q} = 0$ are $\Gamma_H < 41$ MeV and $\Gamma_H < 26$ MeV, respectively. When $f_{\Lambda Q}$ is

CHAPTER 5. PROPERTIES

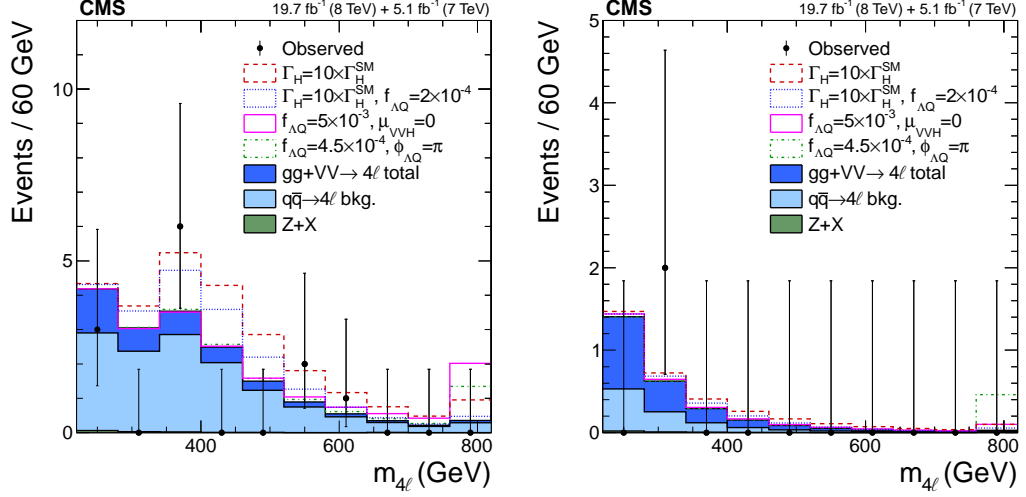


Figure 5.22: Observed 4ℓ events (black points) for off-shell regions, $220 < m_{4\ell} < 800$ GeV where the last bin of the histogram also includes yields for $800 < m_{4\ell} < 1600$ GeV, with expected distributions with SM-like Higgs boson. $gg + VV \rightarrow 4\ell$ distributions (dark blue) account for signal, background, and interference for ggF and VBF & VH production methods. $q\bar{q} \rightarrow ZZ$ (light blue) and $Z + X$ (green) are the dominant and sub-dominant backgrounds. Four BSM contributions are also shown: $\Gamma_H = 10 \times \Gamma_{SM}$ with $f_{\Lambda Q} = 0$ (dashed red) and $f_{\Lambda Q} = 2 \times 10^{-4}$ (dotted blue) show an enhancement just past the $2 \times m_Z$ peak whereas for the $f_{\Lambda Q}$ close to the expected exclusion limits, $\Gamma_H = \Gamma_{SM}$ with $f_{\Lambda Q} = 5 \times 10^{-3}$ (solid magenta) and $f_{\Lambda Q} \times \cos(\phi_{\Lambda Q}) = -4.5 \times 10^{-4}$, the enhancement is almost entirely in $m_{4\ell} > 800$ GeV. On left, $\mathcal{D}_{gg} > 0.67$ and $\mathcal{D}_{jet} < 0.5$ or $N_{jets} < 2$. On right, $\mathcal{D}_{jet} \geq 0.5$.

CHAPTER 5. PROPERTIES

unconstrained, the expected upper limit becomes $\Gamma_H < 73$ MeV with an observed upper limit of $\Gamma_H < 46$ MeV, where all limits are at 95% CL.

Alternatively, for a given value of the Higgs boson width, we can set limits on $f_{\Lambda Q}$. In Fig. 5.24, we set $\Gamma_H = \Gamma_{SM}$. The expected value of $f_{\Lambda Q} \cos(\phi_{\Lambda Q})$ is¹⁹ $0_{-4.5}^{+10.7} \times 10^{-4}$ with an observed best fit of $f_{\Lambda Q} \cos(\phi_{\Lambda Q}) = 0.1_{-3.7}^{+10.5} \times 10^{-4}$, so the Λ_Q anomalous coupling is in agreement with the Standard Model expectations. The observed allowed region at 95% CL is $[-24, 38] \times 10^{-4}$ compared to the expected region of $[-36, 44] \times 10^{-4}$. A limit of $f_{\Lambda Q}$ where Γ_H is allowed to float unconstrained cannot be set because the off-shell behavior disappears entirely as $\Gamma_H \rightarrow 0$. However, the 2D likelihood scan of $(\Gamma_H, f_{\Lambda Q})$ has been constructed, seen in Fig. 5.25.

This off-shell anomalous coupling measurement finishes the set of couplings for the HVV vertex, where all couplings are observed to be in agreement with the Standard Model. Since the other couplings would similarly provide off-shell enhancement (see Fig. 5.20), the technique opens up further extensions to the on-shell spin-parity measurements, both in how they affect the width measurement and to how they could further constrain the anomalous coupling limits set in the on-shell region.

¹⁹Recall that for this analysis, $\phi_{\Lambda Q} = 0$ or π .

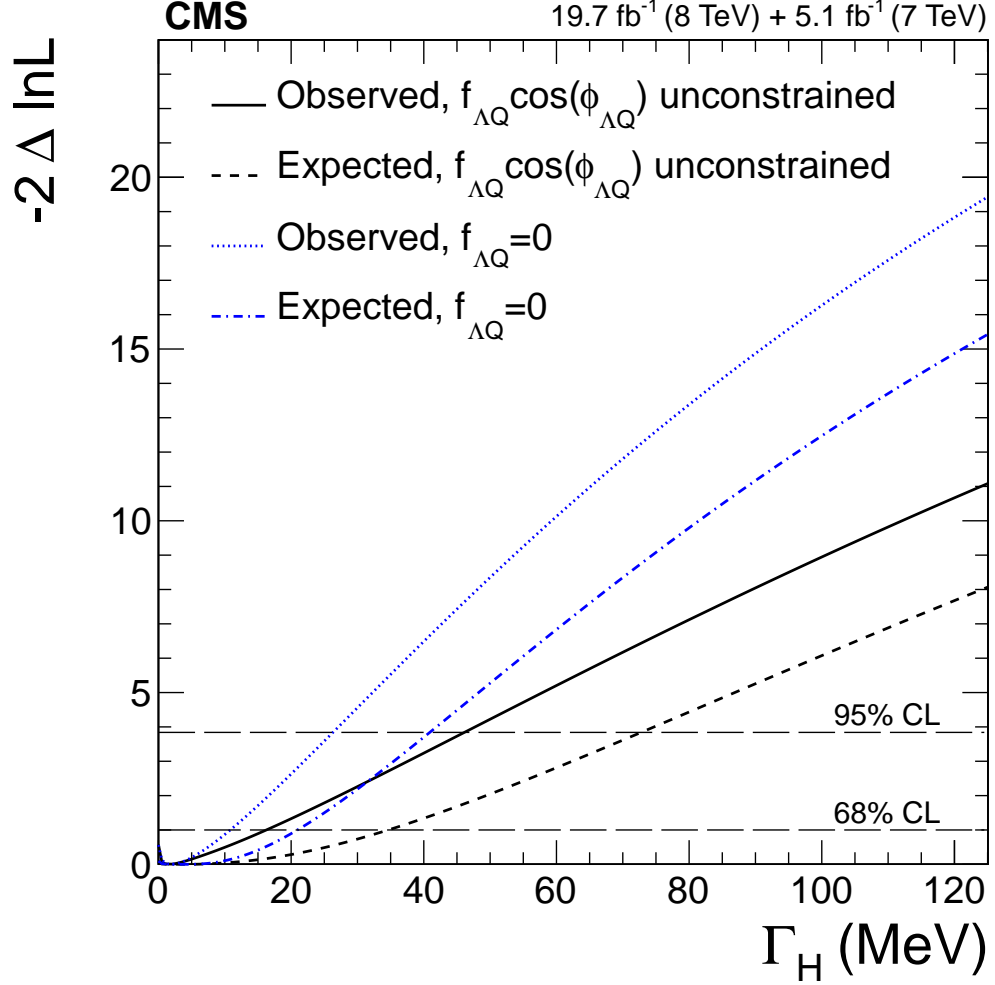


Figure 5.23: Likelihood scans for Higgs boson width for $m_H = 125.6$ GeV with $f_{\Lambda Q}$ anomalous coupling. When $f_{\Lambda Q} = 0$, the results are similar to Sec. 5.4.3 with expected (dot dashed blue) limit of $\Gamma_H < 41$ MeV compared to an observed (dotted blue) limit of $\Gamma_H < 26$ MeV. When $f_{\Lambda Q}$ is allowed to float unconstrained, the width limits loosen giving an observed (solid black) limit of $\Gamma_H < 46$ MeV compared to the expected (dashed black) limit of $\Gamma_H < 73$ MeV. All limits listed at 95% CL.

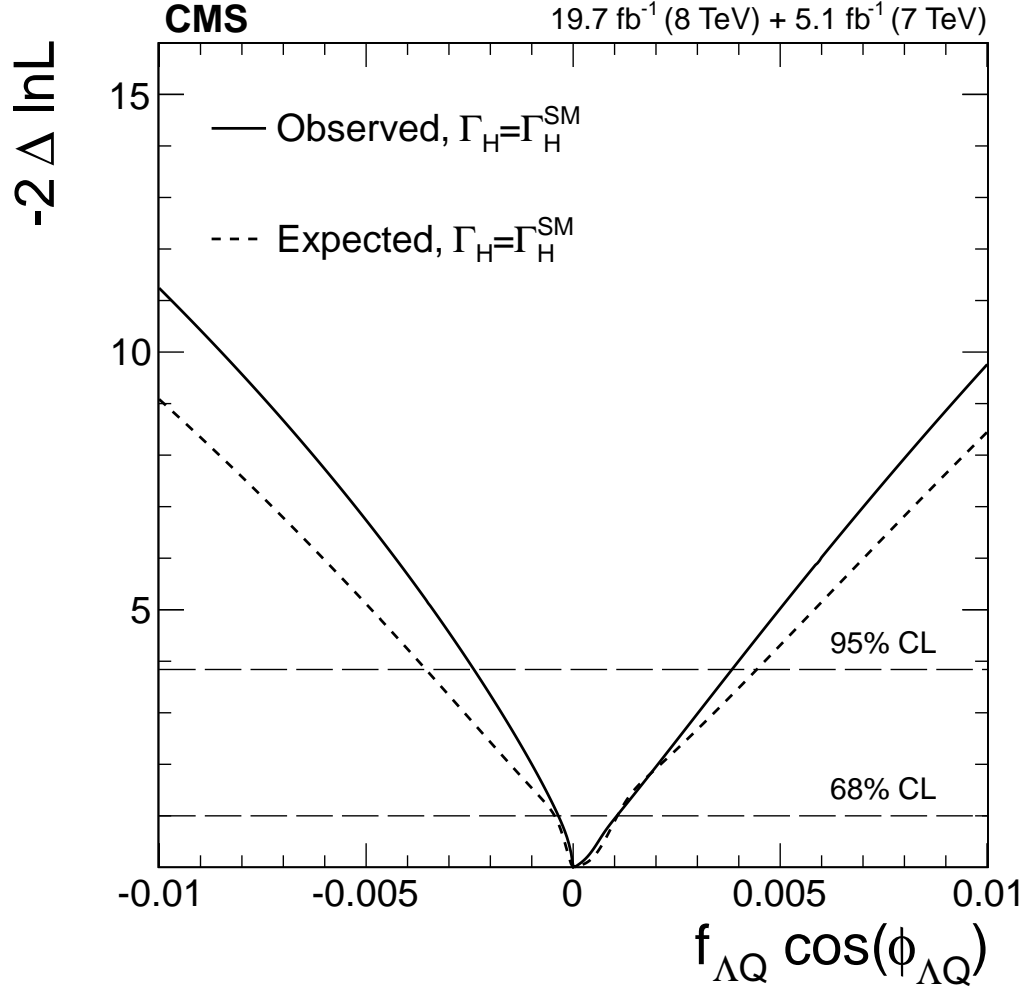


Figure 5.24: Expected (dashed) and observed (solid) likelihood scans for $f_{\Lambda Q} \cos(\phi_{\Lambda Q})$ where $\Gamma_H = \Gamma_H^{\text{SM}}$. Expected allowed region at 95% CL is $[-36, 44] \times 10^{-4}$ compared to observed allowed region of $[-24, 38] \times 10^{-4}$. Observed best fit value of $f_{\Lambda Q} \cos(\phi_{\Lambda Q}) = 0.1^{+10.5}_{-3.7} \times 10^{-4}$ agrees with SM expectations.

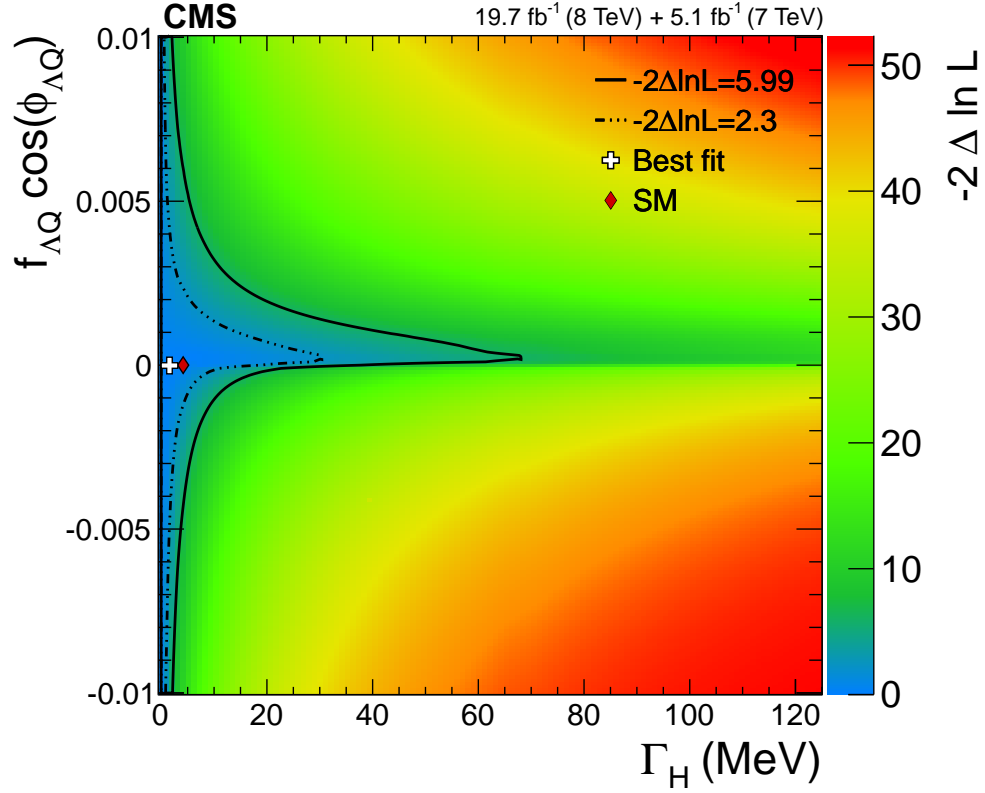


Figure 5.25: 2D $(\Gamma_H, f_{\Lambda Q})$ observed likelihood scan. SM expectation is plotted at the $(\Gamma_{SM}, 0)$ with a red rhombus compared to the observed best fit value at the white cross. Contour limits corresponding to 2D 68% (dot dash line) and 95% CL (solid line) are also plotted. For small values of Γ_H , the limit on $f_{\Lambda Q}$ weakens because $\Gamma_H \rightarrow 0$ gives no expected off-shell signal events to be modified by $f_{\Lambda Q}$.

5.6 Summary

After the discovery of a Higgs-like boson near 125 GeV, the Standard Model provides predictions for a variety of other properties the Higgs boson must exhibit: it should be a spin-0 CP-even scalar; its width should be around 4 MeV; it should have a small off-shell enhancement in the $H \rightarrow VV$ decay channels. In each case, these properties were measured and no anomalous couplings or widths or extra resonances were observed. However, this does not mean that the Higgs boson at 125.6 GeV is The Higgs Boson of the Standard Model, it only implies that nothing anomalous has been observed yet. What, if anything, can we say about future measurements? Can we probe any of these properties further to find a deviation that would disagree with SM expectations and imply new physics?

Chapter 6

Conclusions and Outlook

Two of the overarching goals behind the construction of the LHC and its detectors were to search for any evidence of the Standard Model Higgs boson and to look for any signs of new physics beyond the Standard Model. Behind the work of hundreds of collaborators and centuries of combined experience, the first goal was achieved. In Sec. 4, using the $H \rightarrow ZZ \rightarrow 4l$ decay channel over the first run of data for CMS, a Higgs boson near $m_H = 125.6$ GeV was observed to 7σ global significance. The matrix element methods outlined in Sec. 3 were crucial to its discovery. The second goal of the LHC, observations that indicate new physics, are a bit more nuanced. At the time of writing, the LHC has yet to observe additional resonances that would be indicative of any theoretical extension of the Standard Model. However, we do have a Higgs boson. If its properties disagree with the expectations of the Standard Model, then particle physicists may have a sign of

CHAPTER 6. CONCLUSIONS

what the next development will be.

As shown in Sec. 5, the $m_H = 125.6$ GeV Higgs boson appears to match many of the expectations of the Standard Model. In Sec. 5.2, no additional Higgs-like resonances were found in the high mass region. The spin-parity of the Higgs boson should be a spin-0 CP-even particle. Looking at the results of Sec. 5.3, any spin-1 or spin-2 model is excluded, many at $\geq 3\sigma$. From Sec. 5.3 and 5.5, the fractional measurements of the anomalous HVV couplings are all in agreement with what should be expected for the Standard Model Higgs boson given current statistical and theoretical limitations. Finally, the total width of the resonance, if anomalously large, would be a strong sign of new physics. But as calculated in Sec. 5.4.3 and 5.5 using the combined on-shell and off-shell regions, the width is in agreement with Standard Model expectations. Indeed, when looking at the combination result from all decay channels in CMS, the Higgs boson's signal strength agrees with the predictions, even when split by decay mode as in Fig. 6.1 or when split by production mode¹ as in Fig. 6.2.

However, just because results currently agree with the expectations of the Standard Model does not imply that this Higgs boson is The Higgs Boson. The second run of the LHC at 13 TeV is about to begin physics runs, do we have any expectations of what sensitivity we can reach in these property measurements?

For the total Higgs width, the limits are all driven by the modeling of the off-

¹There is an excess in $t\bar{t}H$ production, coming largely from $H \rightarrow \gamma\gamma$ and $H \rightarrow WW$.

CHAPTER 6. CONCLUSIONS

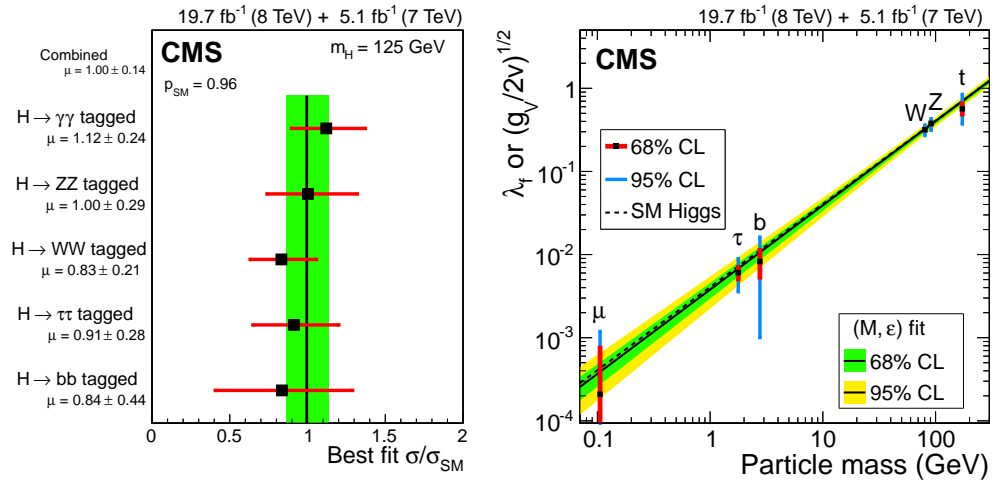


Figure 6.1: On left, signal strengths for the combination (vertical black line, with green $\pm 1\sigma$ uncertainty bands) and split via subcombinations of bosonic ($H \rightarrow \gamma\gamma$, $H \rightarrow ZZ$, $H \rightarrow WW$) and fermionic ($H \rightarrow \tau\tau$, $H \rightarrow b\bar{b}$) decay modes with horizontal red bars for $\pm 1\sigma$ uncertainty around best fit value. On right, deviations of the Higgs boson coupling to fermions and bosons are plotted. Particle masses are taken from [106]. Both plots are from [107].

CHAPTER 6. CONCLUSIONS

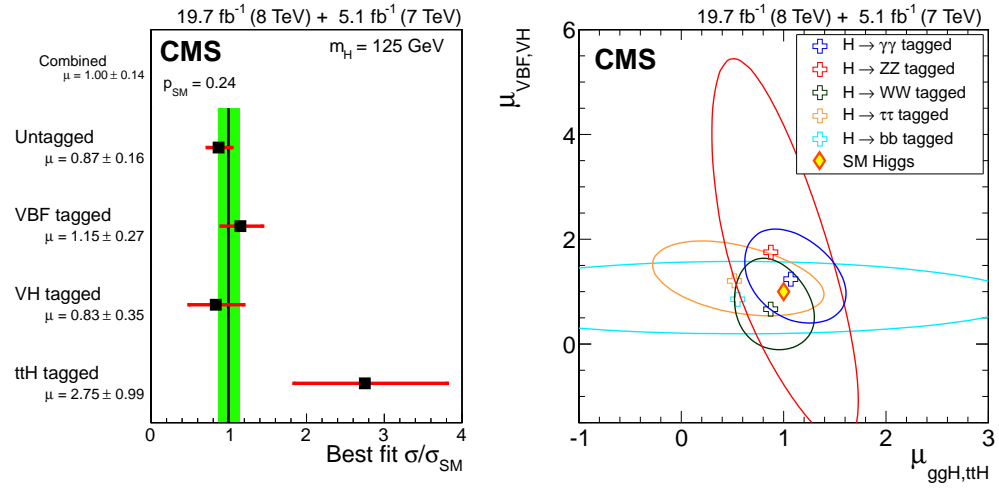


Figure 6.2: On left, signal strengths for the combination (vertical black line, with green $\pm 1\sigma$ uncertainty bands) and split via subcombinations of tags for different production mechanisms (VBF, VH, $t\bar{t}H$, and Untagged) with horizontal red bars for $\pm 1\sigma$ uncertainty around best fit value. On right, comparison of signal strength for bosonic ($\mu_{VBF, VH}$) vs fermionic ($\mu_{ggH, t\bar{t}H}$) couplings split by decay channel, with a cross and 1σ contour for each decay channel plotted alongside the SM expectations (red and yellow diamond). Both plots are from [107].

CHAPTER 6. CONCLUSIONS

shell region. Improving the theoretical uncertainty in the off-shell region – particularly in the scale factor for the $gg \rightarrow 4l$ channel – would necessarily improve the measurement. However, this only goes so far. If the Higgs width is smaller than SM predictions, this could appear in the signal strengths of different decay channels. For large values of the Higgs width, the lack of signal-like events in the off-shell region provides a limit. But because the destructive off-shell interference is proportional to $\sqrt{\Gamma_H}$ while signal is proportional to Γ_H , when $\Gamma_H \approx \Gamma_{SM}$, this intermediate width region cannot be probed well using the off-shell analysis. No expectations for the total width using 13 TeV simulation has been set, but the measurement is not expected to improved dramatically with more data.

However, the anomalous coupling measurements are statistically limited. In [34], we investigated the sensitivities for anomalous HVV couplings within the lifetime of the LHC (both with and without the anticipated high lumionsity upgrade²) and a range of considered energies for a future lepton colliders³. Lepton colliders will have drastically different production preferences than Sec. 3.1.2, with VBF and VH being the dominant mechanisms. Furthermore, the ratios of production cross sections for an anomalous Higgs boson compared to the SM Higgs boson for VBF and VH will be considerably higher than ggF, so these production mechanisms are important to quantify at the LHC, in addition to $H \rightarrow ZZ$ and $H \rightarrow \gamma\gamma$

²The *HL-LHC* is a high luminosity upgrade for the LHC intended to be built in the coming years. It would increase the lifetime integrated luminosity of the LHC by a factor of 10 [108–110].

³Aside from the HL-LHC, there are plans being evaluated for future lepton colliders [111,112] which would require a choice of beam energy.

CHAPTER 6. CONCLUSIONS

decays.

Using JHUGen to generate 14 TeV⁴ signal MC samples and produce the matrix elements, we followed the discriminant framework outlined in Sec. 5.3. POWHEG and MadGraph were used to generate the background events ($q\bar{q} \rightarrow ZZ^{(*)}/Z\gamma^{(*)}/\gamma\gamma^* + \text{jets}$ for LHC, $e^+e^- \rightarrow ZZ$ for lepton colliders), scaled to account for all backgrounds in the respective production or decay. Then, with physics objects defined similarly as Sec. 4.1 and after lepton momenta smearing as used in [31, 33], selection requirements were set similar to Sec. 4.3 for $H \rightarrow ZZ \rightarrow 4l$ or [113] for $H \rightarrow \gamma\gamma$. The total yields of each decay or production was set for the LHC at 300 fb⁻¹ and 3000 fb⁻¹ and different beam energies for lepton colliders.

The predicted sensitivities to the CP-odd cross section from these yields is found in Table 6.1 and Fig. 6.3. In summary, sensitivity to CP violation⁵ in the Higgs boson is expected to be on the order of 10⁻⁴ in the HL-LHC or future linear colliders, particularly from VBF and VH production mechanisms. The expected value of f_{CP} for $H \rightarrow ZZ$ decay is very small, around 10⁻⁵ even for large pseudoscalar contributions.

At the time these sensitivities were projected, the off-shell measurement was not yet designed; these measurements are all from on-shell measurements. If we combine the off-shell anomalous coupling measurement techniques described in

⁴Run II for the LHC is set to 13 TeV, but the design energy of the LHC is 14 TeV.

⁵In Table 6.1 and Fig. 6.3, the term f_{CP} is used. The translation between f_{CP} and f_{a3} from Sec. 3.2 is not linear, but they represent the same information.

CHAPTER 6. CONCLUSIONS

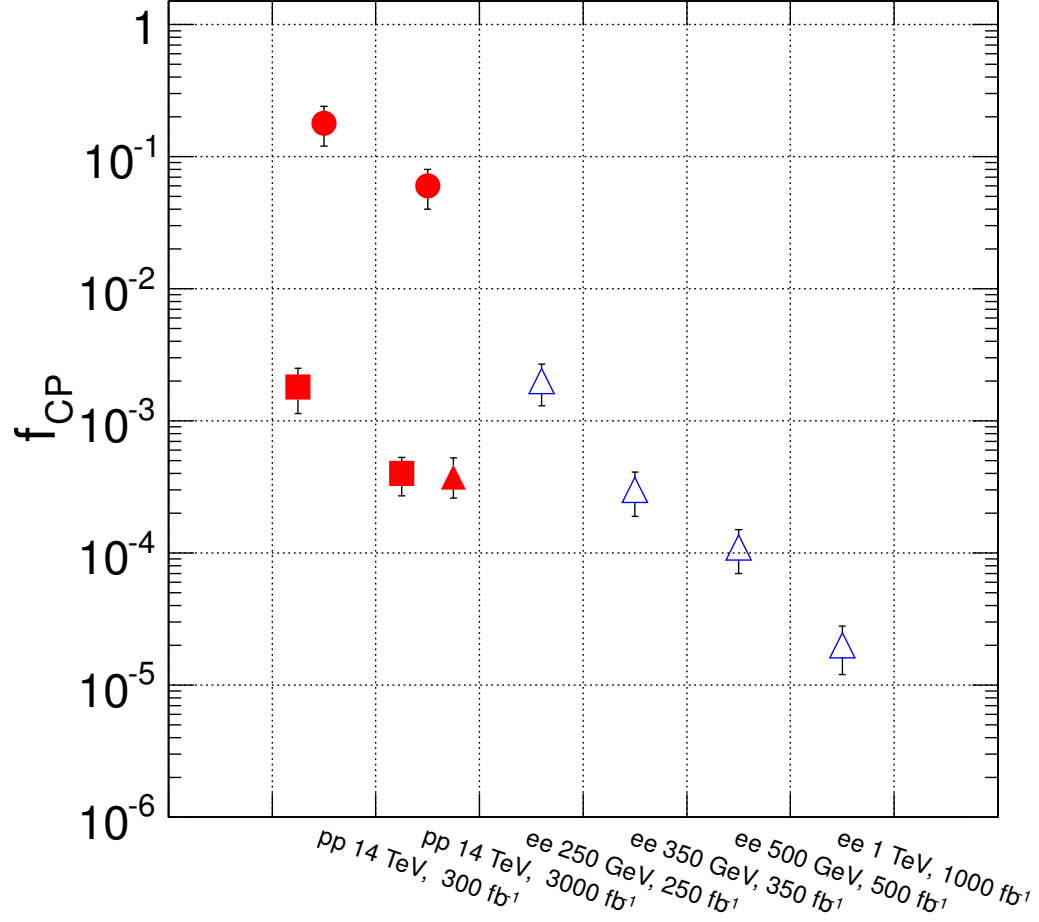


Figure 6.3: Summary of f_{CP} precisions on the HVV vertex at the LHC (solid red) and proposed future colliders (open blue). VH (triangles) and VBF (square) production methods as well as $H \rightarrow VV$ decays (circles) are shown. Energies and luminosities are listed in the x -axis.

CHAPTER 6. CONCLUSIONS

Sec. 5.5, the overall measurement of anomalous HVV couplings can become even tighter, especially for VBF production. It is plausible that the sensitivity of f_{CP} could become test some BSM theoretical predictions within the lifetime of the LHC. Until and unless the LHC observes new particles not predicted by the Standard Model, this technique and others like it can provide more concrete information concerning physics beyond the Standard Model.

By any standard, the searches and property measurements of the Higgs Boson should be considered a grand success, both for the Standard Model and the LHC. For their theoretical contribution, Higgs and Englert were jointly awarded the Nobel Prize in Physics in 2013. But the Higgs Boson was the last piece of the Standard Model which – even with its immense predictive power and precision – is known to be insufficient to explain all phenomena in particle physics. The next wave of searches, either through direct measurement of new particles or indirectly through precision Higgs boson properties, will aim to answer the current mysteries: What, exactly, is dark matter? What about dark energy? Why is there more matter than antimatter? In short, the question we must answer individually and cosmically: How did we get here and where are we going? That is the solitary goal of all particle physics, even physics in general. Through the LHC and the Higgs boson, we move closer to providing an answer.

Collider	Energy GeV	\mathcal{L} fb^{-1}	HZZ/HWW				H_{gg}		$HZ\gamma$	$H\gamma\gamma$	
			$H \rightarrow VV^*$ f_{CP} δf_{CP}	$V^* \rightarrow VH$ f_{CP} δf_{CP}	$V^*V^* \rightarrow H$ f_{CP} δf_{CP}		$gg \rightarrow H$ f_{CP} δf_{CP}		$H \rightarrow Z\gamma$	$\gamma\gamma \rightarrow H$	$H \rightarrow \gamma\gamma$
pp	14 000	300	0.18 0.06	6×10^{-4} 4×10^{-4}	18×10^{-4} 7×10^{-4}		– 0.50				
pp	14 000	3 000	0.06 0.02	3.7×10^{-4} 1.2×10^{-4}	4.1×10^{-4} 1.3×10^{-4}		0.50 0.16		✓		✓
e^+e^-	250	250	✓	21×10^{-4} 7×10^{-4}	✓						
e^+e^-	350	350	✓	3.4×10^{-4} 1.1×10^{-4}	✓						
e^+e^-	500	500	✓	11×10^{-5} 4×10^{-5}	✓						
e^+e^-	1 000	1 000	✓	20×10^{-6} 8×10^{-6}	✓						
$\gamma\gamma$	125		✓							✓	

 Table 6.1: Projected sensitivities for f_{CP} in HVV couplings at 3σ significance with corresponding uncertainties.

Current LHC lifetime projections were found using a beam energy of 14 TeV and integrated luminosity of 300 fb^{-1} or 3000 fb^{-1} including the anticipated high luminosity upgrade. e^+e^- and $\gamma\gamma$ refer to proposed future lepton or photon colliders. Numerical values are calculated for H_{gg} and HZZ/HWW decays. The ✓ indicates that a measurement could be done, but its projection was not calculated.

Bibliography

- [1] D. Galbraith and C. Burgard, "UX: Standard Model of the Standard Model," 2012, CERN Webfest 2012. [Online]. Available: "<http://davidgalbraith.org/portfolio/ux-standard-model-of-the-standard-model/>"
- [2] H. Georgi, *Lie Algebras In Particle Physics: from Isospin To Unified Theories*, 2nd ed. Westview Press, 1999.
- [3] E. S. Walter Greiner, Stefan Schramm, *Quantum Chromodynamics*, 3rd ed. Springer, 2007.
- [4] S. L. Glashow, "Partial-symmetries of Weak Interactions," *Nucl. Phys.*, vol. 22, p. 579, 1961.
- [5] P. W. Anderson, "Plasmons, Gauge Invariance, and Mass," *Phys. Rev.*, vol. 130, pp. 439–442, Apr 1963.

BIBLIOGRAPHY

- [6] P. W. Higgs, "Broken Symmetries and the Masses of Gauge Bosons," *Phys. Rev. Lett.*, vol. 13, p. 508, 1964.
- [7] F. Englert and R. Brout, "Broken Symmetry and the Mass of Gauge Vector Mesons," *Phys. Rev. Lett.*, vol. 13, p. 321, 1964.
- [8] P. W. Higgs, "Broken symmetries, massless particles and gauge fields," *Phys. Lett.*, vol. 12, p. 132, 1964.
- [9] G. Guralnik, C. Hagen, and T. Kibble, "Global Conservation Laws and Massless Particles," *Phys. Rev. Lett.*, vol. 13, p. 585, 1964.
- [10] S. Weinberg, "A Model of Leptons," *Phys. Rev. Lett.*, vol. 19, pp. 1264–1266, 1967.
- [11] A. Salam, "Elementary Particle Physics," *N. Svartholm ed., Almqvist and Wiksell, Stockholm*, 1968.
- [12] F. Hasert *et al.*, "Observation of Neutrino Like Interactions Without Muon Or Electron in the Gargamelle Neutrino Experiment," *Phys.Lett.*, vol. B46, pp. 138–140, 1973.
- [13] G. Arnison *et al.*, "Experimental Observation of Isolated Large Transverse Energy Electrons with Associated Missing Energy at $\sqrt{s} = 540$ GeV," *Phys.Lett.*, vol. B122, pp. 103–116, 1983.

BIBLIOGRAPHY

- [14] G. Arnison *et al.*, “Experimental Observation of Lepton Pairs of Invariant Mass Around $95 \text{ GeV}/c^2$ at the CERN SPS Collider,” *Phys.Lett.*, vol. B126, pp. 398–410, 1983.
- [15] P. Bagnaia *et al.*, “Evidence for $Z_0 \rightarrow e^+e^-$ at the CERN anti-p p Collider,” *Phys.Lett.*, vol. B129, pp. 130–140, 1983.
- [16] M. Sher, “Electroweak Higgs potential and vacuum stability,” *Physics Reports*, vol. 179, no. 5–6, pp. 273 – 418, 1989.
- [17] R. Barate *et al.*, “Search for the standard model Higgs boson at LEP,” *Phys.Lett.*, vol. B565, pp. 61–75, 2003.
- [18] “Combined CDF and D0 Upper Limits on Standard Model Higgs Boson Production with up to 8.6 fb^{-1} of Data,” 2011.
- [19] A. Sakharov, “Violation of CP Invariance, c Asymmetry, and Baryon Asymmetry of the Universe,” *Pisma Zh.Eksp.Teor.Fiz.*, vol. 5, pp. 32–35, 1967, reprinted in *Kolb, E.W. (ed.), Turner, M.S. (ed.): The early universe* 371-373, and in *Lindley, D. (ed.) et al.: Cosmology and particle physics* 106-109, and in *Sov. Phys. Usp.* 34 (1991) 392-393 [*Usp. Fiz. Nauk* 161 (1991) No. 5 61-64].
- [20] Y. Fukuda *et al.*, “Evidence for oscillation of atmospheric neutrinos,” *Phys.Rev.Lett.*, vol. 81, pp. 1562–1567, 1998.

BIBLIOGRAPHY

- [21] S. Chatrchyan *et al.*, “Measurement of the properties of a Higgs boson in the four-lepton final state,” *Phys. Rev. D*, vol. 89, p. 092007, May 2014.
- [22] CMS Collaboration, *CMS Physics: Technical Design Report Volume 1: Detector Performance and Software*, ser. Technical Design Report CMS. Geneva: CERN, 2006, there is an error on cover due to a technical problem for some items.
- [23] CMS Collaboration, “CMS Physics: Technical Design Report Volume 2: Physics Performance,” *J. Phys. G*, vol. 34, no. CERN-LHCC-2006-021. CMS-TDR-8-2, pp. 995–1579. 669 p, 2007, revised version submitted on 2006-09-22 17:44:47.
- [24] V. Blobel, “Software alignment for tracking detectors,” *Nucl. Instrum. Meth.*, vol. A566, pp. 5–13, 2006.
- [25] V. Karimaki, T. Lampen, and F. Schilling, “The HIP algorithm for track based alignment and its application to the CMS pixel detector,” 2006.
- [26] E. Widl, R. Fruhwirth, and W. Adam, “A Kalman filter for track-based alignment,” 2006.
- [27] CMS Collaboration, “Alignment of the CMS Silicon Tracker during Commissioning with Cosmic Rays,” *JINST*, vol. 5, p. T03009, 2010.
- [28] CMS Collaboration, “Particle-Flow Event Reconstruction in CMS and Per-

BIBLIOGRAPHY

- formance for Jets, Taus, and MET,” CERN, 2009. Geneva, Tech. Rep. CMS-PAS-PFT-09-001, Apr 2009.
- [29] N. Metropolis and S. Ulam, “The Monte Carlo Method,” *Journal of the American Statistical Association*, vol. 44, no. 247, pp. 335–341, 1949, pMID: 18139350.
- [30] LHC Higgs Cross Section Working Group, S. Heinemeyer, C. Mariotti, G. Passarino, and R. Tanaka (Eds.), “Handbook of LHC Higgs Cross Sections: 3. Higgs Properties,” *CERN-2013-004*, CERN, Geneva, 2013.
- [31] Y. Gao, A. V. Gritsan, Z. Guo, K. Melnikov, M. Schulze *et al.*, “Spin determination of single-produced resonances at hadron colliders,” *Phys.Rev.*, vol. D81, p. 075022, 2010.
- [32] A. Soni and R. M. Xu, “Probing CP violation via Higgs boson decays to four leptons,” *Phys. Rev. D*, vol. 48, pp. 5259–5263, Dec 1993.
- [33] S. Bolognesi, Y. Gao, A. V. Gritsan, K. Melnikov, M. Schulze *et al.*, “On the spin and parity of a single-produced resonance at the LHC,” *Phys.Rev.*, vol. D86, p. 095031, 2012.
- [34] I. Anderson, S. Bolognesi, F. Caola, Y. Gao, A. V. Gritsan *et al.*, “Constraining anomalous HVV interactions at proton and lepton colliders,” *Phys.Rev.*, vol. D89, no. 3, p. 035007, 2014.
- [35] Y. Chen, E. Di Marco, J. Lykken, M. Spiropulu, R. Vega-Morales *et al.*, “8D

BIBLIOGRAPHY

- likelihood effective Higgs couplings extraction framework in $h \rightarrow 4\ell$," *JHEP*, vol. 1501, p. 125, 2015.
- [36] S. Baffioni, C. Charlot, F. Ferri, D. Futyan, P. Meridiani, I. Puljak, C. Rovelli, R. Salerno, and Y. Sirois, "Electron reconstruction in CMS," *Eur. Phys. J. C*, vol. 49, p. 1099, 2007.
- [37] CMS Collaboration, "Electron reconstruction and identification at $\sqrt{s} = 7$ TeV," CMS Physics Analysis Summary CMS-PAS-EGM-10-004, 2010.
- [38] CMS Collaboration, "Electron commissioning results at $\sqrt{s} = 7$ TeV," CMS Detector Performance Summary CMS-DP-2011-003, 2011.
- [39] e/g POG, "Electron Selection Criteria in 2012," *CMS AN 2012/201*, 2012.
- [40] CMS Collaboration, "Performance of CMS muon reconstruction in pp collision events at $\sqrt{s} = 7$ TeV," *Journal of Instrumentation*, vol. 7, no. 10, p. P10002, 2012.
- [41] CMS Collaboration, "Commissioning of the particle-flow event reconstruction with leptons from J/ψ and W decays at 7 TeV," CMS Physics Analysis Summary CMS-PAS-PFT-10-003, 2010.
- [42] M. Cacciari and G. P. Salam, "Pileup subtraction using jet areas," *Phys. Lett. B*, vol. 659, p. 119, 2008.

BIBLIOGRAPHY

- [43] M. Cacciari, G. P. Salam, and G. Soyez, “The Catchment Area of Jets,” *JHEP*, vol. 04, p. 005, 2008.
- [44] G. Daskalakis *et al.*, “Measuring Electron Efficiencies at CMS with Early Data,” *CMS Analysis Note*, vol. 2007/019, 2007.
- [45] M. Cacciari and G. P. Salam and G. Soyez, “The anti- k_T jet clustering algorithm,” *JHEP*, vol. 04, p. 063, 2008.
- [46] M. Cacciari, G. P. Salam, and G. Soyez, “FastJet user manual (for version 3.0.2),” *Eur. Phys. J. C*, vol. 72, p. 1896, 2012.
- [47] S. Chatrchyan *et al.*, “Determination of Jet Energy Calibration and Transverse Momentum Resolution in CMS,” *JINST*, vol. 6, p. P11002, 2011.
- [48] CMS Collaboration, “Pileup Jet Identification,” CERN, Geneva, Tech. Rep. CMS-PAS-JME-13-005, 2013.
- [49] S. Frixione, P. Nason, and C. Oleari, “Matching NLO QCD computations with parton shower simulations: the POWHEG method,” *JHEP*, vol. 11, p. 070, 2007.
- [50] T. Sjöstrand, S. Mrenna, and P. Z. Skands, “PYTHIA 6.4 Physics and Manual,” *JHEP*, vol. 05, p. 026, 2006.
- [51] G. Passarino, C. Sturm, and S. Uccirati, “Higgs pseudo-observables, second Riemann sheet and all that,” *Nucl. Phys. B*, vol. 834, p. 77, 2010.

BIBLIOGRAPHY

- [52] S. Goria, G. Passarino, and D. Rosco, “The Higgs Boson Lineshape,” *Nucl. Phys. B*, vol. 864, p. 530, 2012.
- [53] N. Kauer and G. Passarino, “Inadequacy of zero-width approximation for a light Higgs boson signal,” *JHEP*, vol. 08, p. 116, 2012.
- [54] D. de Florian, G. Ferrera, M. Grazzini, and D. Tommasini, “Higgs boson production at the LHC: transverse momentum resummation effects in the $H \rightarrow 2\gamma$, $H \rightarrow WW \rightarrow 2\ell 2\nu$ and $H \rightarrow ZZ \rightarrow 4\ell$ decay modes,” *JHEP*, vol. 06, p. 132, 2012.
- [55] C. Anastasiou, R. Boughezal, and F. Petriello, “Mixed QCD-electroweak corrections to Higgs boson production in gluon fusion,” *JHEP*, vol. 04, p. 003, 2009.
- [56] D. de Florian and M. Grazzini, “Higgs production through gluon fusion: updated cross sections at the Tevatron and the LHC,” *Phys. Lett. B*, vol. 674, p. 291, 2009.
- [57] J. Baglio and A. Djouadi, “Higgs production at the LHC,” *JHEP*, vol. 03, p. 055, 2011.
- [58] LHC Higgs Cross Section Working Group, S. Dittmaier, C. Mariotti, G. Passarino, and R. Tanaka (Eds.), “Handbook of LHC Higgs Cross Sections: 1. Inclusive Observables,” *CERN-2011-002*, CERN, Geneva, 2011.

BIBLIOGRAPHY

- [59] A. Djouadi, M. Spira, and P. M. Zerwas, "Production of Higgs bosons in proton colliders: QCD corrections," *Phys. Lett. B*, vol. 264, p. 440, 1991.
- [60] S. Dawson, "Radiative corrections to Higgs boson production," *Nucl. Phys. B*, vol. 359, p. 283, 1991.
- [61] M. Spira, A. Djouadi, D. Graudenz, and R. M. Zerwas, "Higgs boson production at the LHC," *Nucl. Phys. B*, vol. 453, p. 17, 1995.
- [62] R. V. Harlander and W. B. Kilgore, "Next-to-next-to-leading order Higgs production at hadron colliders," *Phys. Rev. Lett.*, vol. 88, p. 201801, 2002.
- [63] C. Anastasiou and K. Melnikov, "Higgs boson production at hadron colliders in NNLO QCD," *Nucl. Phys. B*, vol. 646, p. 220, 2002.
- [64] V. Ravindran, J. Smith, and W. L. van Neerven, "NNLO corrections to the total cross section for Higgs boson production in hadron-hadron collisions," *Nucl. Phys. B*, vol. 665, p. 325, 2003.
- [65] S. Catani, D. de Florian, M. Grazzini, and P. Nason, "Soft gluon resummation for Higgs boson production at hadron colliders," *JHEP*, vol. 07, p. 028, 2003.
- [66] S. Actis, G. Passarino, C. Sturm, and S. Uccirati, "NLO electroweak corrections to Higgs boson production at hadron colliders," *Phys. Lett. B*, vol. 670, p. 12, 2008.

BIBLIOGRAPHY

- [67] M. Ciccolini, A. Denner, and S. Dittmaier, “Strong and electroweak corrections to the production of Higgs + 2-jets via weak interactions at the LHC,” *Phys. Rev. Lett.*, vol. 99, p. 161803, 2007.
- [68] M. Ciccolini, A. Denner, and S. Dittmaier, “Electroweak and QCD corrections to Higgs production via vector-boson fusion at the LHC,” *Phys. Rev. D*, vol. 77, p. 013002, 2008.
- [69] T. Figy, D. Zeppenfeld, and C. Oleari, “Next-to-leading order jet distributions for Higgs boson production via weak-boson fusion,” *Phys. Rev. D*, vol. 68, p. 073005, 2003.
- [70] K. Arnold *et al.*, “VBFNLO: A parton level Monte Carlo for processes with electroweak bosons,” *Comput. Phys. Commun.*, vol. 180, p. 1661, 2009.
- [71] P. Bolzoni, F. Maltoni, S.-O. Moch, and M. Zaro, “Higgs Boson Production via Vector-Boson Fusion at NNLO at Next-to-Next-to-Leading Order in QCD,” *Phys. Rev. Lett.*, vol. 105, p. 011801, 2010.
- [72] J. Alwall, P. Demin, S. de Visscher, R. Frederix, M. Herquet, F. Maltoni, T. Plehn, D. L. Rainwater, and T. Stelzer, “MadGraph/MadEvent v4: the new web generation,” *JHEP*, vol. 09, p. 028, 2007.
- [73] T. Binoth, N. Kauer, and P. Mertsch, “Gluon-induced QCD Corrections to $pp \rightarrow ZZ \rightarrow \ell\bar{\ell}\ell'\bar{\ell}'$,” p. 142, 2008.

BIBLIOGRAPHY

- [74] S. Agostinelli *et al.*, “GEANT4—a simulation toolkit,” *Nucl. Instrum. Meth. A*, vol. 506, p. 250, 2003.
- [75] J. Allison *et al.*, “Geant4 developments and applications,” *IEEE Trans. Nucl. Sci.*, vol. 53, p. 270, 2006.
- [76] H.-L. Lai, J. Huston, Z. Li, P. Nadolsky, J. Pumplin, D. Stump, and C.-P. Yuan, “Uncertainty induced by QCD coupling in the CTEQ global analysis of parton distributions,” *Phys. Rev. D*, vol. 82, p. 054021, 2010.
- [77] H.-L. Lai, M. Guzzi, J. Huston, Z. Li, P. M. Nadolsky, J. Pumplin, and C.-P. Yuan, “New parton distributions for collider physics,” *Phys. Rev. D*, vol. 82, p. 074024, 2010.
- [78] J. M. Campbell and R. K. Ellis, “MCFM for the Tevatron and the LHC,” *Nucl. Phys. Proc. Suppl.*, vol. 205, p. 10, 2010.
- [79] J. M. Campbell and R. K. Ellis, “An update on vector boson pair production at hadron colliders,” *Phys. Rev. D*, vol. 60, p. 113006, 1999.
- [80] J. M. Campbell, R. K. Ellis, and C. Williams, “Vector boson pair production at the LHC,” *JHEP*, vol. 07, p. 018, 2011.
- [81] M. Oreglia, “A study of the reactions $\psi' \rightarrow \gamma\gamma\psi$,” Ph.D. dissertation, Stanford University, 1980, SLAC Report SLAC-R-236.

BIBLIOGRAPHY

- [82] CMS Collaboration, “Measurement of the Rapidity and Transverse Momentum Distributions of Z Bosons in pp Collision at $\sqrt{s} = 7$ TeV,” *Phys. Rev. D*, vol. 85, p. 032002, 2012.
- [83] CMS Collaboration, “Measurement of the Λ_b cross section and the $\bar{\Lambda}_b$ to Λ_b ratio with $J/\psi\Lambda$ decays in pp collisions at $\sqrt{s} = 7$ TeV,” *Phys. Lett. B*, vol. 714, p. 136, 2012.
- [84] S. Chatrchyan *et al.*, “Evidence for the 125 GeV Higgs boson decaying to a pair of τ leptons,” *JHEP*, vol. 1405, p. 104, 2014.
- [85] ATLAS and CMS Collaborations, LHC Higgs Combination Group, “Procedure for the LHC Higgs boson search combination in Summer 2011,” ATLAS-*PHYS-PUB* 2011-11/CMS NOTE 2011/005, 2011.
- [86] J. Beringer *et al.*, “Review of Particle Physics,” *Phys. Rev. D*, vol. 86, p. 010001, 2012.
- [87] T. Junk, “Confidence level computation for combining searches with small statistics,” *Nucl. Instrum. Meth. A*, vol. 434, p. 435, 1999.
- [88] V. Khachatryan *et al.*, “Search for a Higgs boson in the mass range from 145 to 1000 GeV decaying to a pair of W or Z bosons,” 2015.
- [89] V. Khachatryan *et al.*, “Constraints on the spin-parity and anomalous HVV couplings of the Higgs boson in proton collisions at 7 and 8 TeV,” 2014.

BIBLIOGRAPHY

- [90] V. Khachatryan *et al.*, “Constraints on the Higgs boson width from off-shell production and decay to Z-boson pairs,” *Phys.Lett.*, vol. B736, p. 64, 2014.
- [91] G. Passarino, “Higgs Interference Effects in $gg \rightarrow ZZ$ and their Uncertainty,” *JHEP*, vol. 1208, p. 146, 2012.
- [92] S. Chatrchyan *et al.*, “Observation of a new boson at a mass of 125 GeV with the CMS experiment at the LHC,” *Phys. Lett. B*, vol. 716, p. 30, 2012.
- [93] P. Avery, D. Bourilkov, M. Chen, T. Cheng, A. Drozdetskiy, J. S. Gainer, A. Korytov, K. T. Matchev, P. Milenovic, G. Mitselmakher, M. Park, A. Rinkevicius, and M. Snowball, “Precision studies of the Higgs boson decay channel $H \rightarrow ZZ^* \rightarrow 4\ell$ with MEKD,” *Phys. Rev. D*, vol. 87, p. 055006, 2013.
- [94] N. D. Christensen and C. Duhr, “FeynRules - Feynman rules made easy,” *Comput. Phys. Comm.*, vol. 180, p. 1614, 2009.
- [95] Y. Chen, N. Tran, and R. Vega-Morales, “Scrutinizing the Higgs Signal and Background in the $2e2\mu$ Golden Channel,” *JHEP*, vol. 01, p. 182, 2013.
- [96] Y. Chen, R. Harnik, and R. Vega-Morales, “Probing the Higgs Couplings to Photons in $h \rightarrow 4\ell$ at the LHC,” *Phys.Rev.Lett.*, vol. 113, no. 19, p. 191801, 2014.
- [97] N. Kauer, “Inadequacy of zero-width approximation for a light Higgs boson signal,” *Mod. Phys. Lett. A*, vol. 28, p. 1330015, 2013.

BIBLIOGRAPHY

- [98] F. Caola and K. Melnikov, “Constraining the Higgs boson width with ZZ production at the LHC,” *Phys. Rev. D*, vol. 88, p. 054024, 2013.
- [99] M. Bonvini, F. Caola, S. Forte, K. Melnikov, and G. Ridolfi, “Signal-background interference effects in $gg \rightarrow H \rightarrow WW$ beyond leading order,” *Phys. Rev. D*, vol. 88, p. 034032, 2013.
- [100] M. Krämer, E. Laenen, and M. Spira, “Soft gluon radiation in Higgs boson production at the {LHC},” *Nuclear Physics B*, vol. 511, no. 3, pp. 523 – 549, 1998.
- [101] J. Baglio, L. D. Ninh, and M. M. Weber, “Massive gauge boson pair production at LHC: a next-to-leading order story,” *Phys. Rev. D*, vol. 88, p. 113005, 2013.
- [102] A. Bierweiler, T. Kasprzik, and J. H. Kühn, “Vector-boson pair production at the LHC to $\mathcal{O}(\alpha^3)$ accuracy,” *JHEP*, vol. 12, p. 071, 2013.
- [103] S. Gieseke, T. Kasprzik, and J. H. Kühn, “Vector-boson pair production and electroweak corrections in HERWIG++,” *Eur.Phys.J.*, vol. C74, no. 8, p. 2988, 2014.
- [104] T. Kasprzik, Private communication.
- [105] G. Passarino, “Higgs CAT,” *Eur.Phys.J.*, vol. C74, p. 2866, 2014.

BIBLIOGRAPHY

- [106] K. Olive *et al.*, “Review of Particle Physics,” *Chin.Phys.*, vol. C38, p. 090001, 2014.
- [107] V. Khachatryan *et al.*, “Precise determination of the mass of the Higgs boson and tests of compatibility of its couplings with the standard model predictions using proton collisions at 7 and 8 TeV,” 2014.
- [108] “Physics at a High-Luminosity LHC with ATLAS,” 2013.
- [109] “Projected Performance of an Upgraded CMS Detector at the LHC and HL-LHC: Contribution to the Snowmass Process,” 2013.
- [110] S. Dawson, A. Gritsan, H. Logan, J. Qian, C. Tully *et al.*, “Working Group Report: Higgs Boson,” 2013.
- [111] T. Behnke, J. E. Brau, B. Foster, J. Fuster, M. Harrison *et al.*, “The International Linear Collider Technical Design Report - Volume 1: Executive Summary,” 2013.
- [112] M. Koratzinos, A. Blondel, R. Aleksan, O. Brunner, A. Butterworth *et al.*, “TLEP: A High-Performance Circular e^+e^- Collider to Study the Higgs Boson,” p. TUPME040, 2013.
- [113] V. Khachatryan *et al.*, “Observation of the diphoton decay of the Higgs boson and measurement of its properties,” *Eur.Phys.J.*, vol. C74, no. 10, p. 3076, 2014.

CURRICULUM VITAE

Ian Anderson

Johns Hopkins University, Department of Physics and Astronomy

Email: ianderso@pha.jhu.edu

Phone: 717-580-4187

Education

B.S., Physics with Honors

Carnegie Mellon University, September 2005 - June 2009

M.A., Physics

Johns Hopkins University, 2011

Ph.D., Physics, Expected May 2015

Johns Hopkins University, September 2009 - present

Research Experience

- Graduate Research, Johns Hopkins University, CMS Collaboration, Fall 2011 - present
 - Discovered Higgs boson to very high statistical significance ($\sim 7\sigma$) with small number (~ 25) out of billions of potential events
 - Utilized grid computing and parallel processing over very large datasets (> 1 PB)
 - Developed novel multivariate analyses to measure properties of Higgs produc-

CURRICULUM VITAE

tion

- Produced and validated new Monte Carlo simulator used throughout LHC Experiment
 - Interpreted data through statistical analysis
 - Implemented technique to improve measurement of Higgs width by a factor of 200 over prior methods
- Monte Carlo Convener for HZZ, CMS Collaboration, 2013 - 2014
 - Led and coordinated Monte Carlo Simulation across 20+ research institutions from seven countries
 - Defined, produced, and validated Monte Carlo Simulations for six different scientific publications
- Research Assistant, INFN Bari, CMS Collaboration, Fall 2012
 - Interfaced between INFN Bari and other international research institutions
 - Developed analyses to produce consistency between multiple statistical frameworks
- Research Assistant, Johns Hopkins University, USA, Summers 2010 & 2011
 - Implemented software for noise reduction of astronomical observations
- Undergraduate Research Assistant, Indiana University, USA, Summer 2008
 - Analyzed discrepancies between many-body discrete models and continuous approximations in particle accelerator design

CURRICULUM VITAE

Invited Positions

- Instructor, CMS Data Analysis School, January 2013
 - Created and Organized rigorous week long Data Analysis Exercise for Graduate Students in CMS Collaboration
 - Taught data analysis techniques common to the $H \rightarrow ZZ$ subgroup of the CMS Experiment

Teaching Experience

- Head Teaching Assistant, General Mechanics II, Spring 2015
- Teaching Assistant, Advanced Physics Lab, Springs 2013 & 2014
 - Designed and validated experimental procedures for upper-level undergraduate physics majors
 - Taught statistical techniques including model building and error analysis
- Teaching Assistant, General Physics II, Springs 2010, 2012, 2013
- Teaching Assistant, Special Relativity and Waves, Fall 2011
- Teaching Assistant, General Physics I, Falls 2009 & 2012, Spring 2011
- Teaching Assistant, General Physics I Lab, Falls 2009 & 2012, Springs 2010 & 2011

Presentations and Talks

- Pheno 2014. Pittsburgh, PA, May 2014
 - “Constraints on the Higgs boson total width using off-shell production in the ZZ

CURRICULUM VITAE

decay"

- APS April Meeting. Savannah, GA, April 2014

"Measurement of the properties of a Higgs boson in the four-lepton final state"

- CMS WGM 183. Geneva, Switzerland, April 2014

"Constraints on the Higgs boson width from off-shell $H \rightarrow ZZ$ production"

Publications

- Selected Refereed Journal Publications

- I. Anderson et al., "Constraining anomalous HVV interactions at proton and lepton colliders", Phys. Rev. D 89, 035007
- CMS Collaboration, "Measurement of the properties of a Higgs boson in the four-lepton final state", Phys. Rev. D 89, 092007
- CMS Collaboration, "Constraints on the Higgs boson width from off-shell production and decay to Z-boson pairs", Phys. Lett. B 736 (2014) 64

- Submitted Journal Publications

- CMS Collaboration, "Constraints on the spin-parity and anomalous HVV couplings of the Higgs boson in proton collisions at 7 and 8 TeV", CMS PAS HIG-14-018 (2014)

- Papers in Preparation

- CMS Collaboration, "High mass WW and ZZ Higgs search with full statistics"
- CMS Collaboration, "Lifetime analysis using Higgs to 4l events"

CURRICULUM VITAE

Educational Outreach

- USA Science and Engineering Festival, Aprils 2012 & 2014
 - National biennial science festival with 300k+ attendees
 - Provided public outreach related to CMS and Experimental Particle Physics
- Johns Hopkins Physics Fair, Aprils 2010 - 2015
 - Annual outreach program for local families and children on physics information
- Baltimore Area High School Demonstrations, March 2013
 - Organized demonstrations for local area high school physics courses

July 14, 2015